ABSTRACT

Title of document: WIND-INDUCED VIBRATION ENERGY HARVESTING USING PIEZOELECTRIC TRANSDUCERS COUPLED WITH DYNAMIC MAGNIFICATION

Austin Baker, Kathryn Connolly, Lauren Dorsey, Ian Grissom, Alden Grobicki, Kevin Keller, Chandan Kittur, Daniel Konecki, Mark Lee, Timothy Lee, Boheng Ma, Edward Mulhern, Andrea Ng, Mihir Patel.

Directed by: Professor Amr Baz
Department of Mechanical Engineering

Flexible cylindrical structures subjected to wind loading experience vibrations from periodic shedding of vortices in their wake. Vibrations become excessive when the natural frequencies of the cylinder coincide with the vortex shedding frequency. In this study, cylinder vibrations are transmitted to a beam inside the structure via dynamic magnifier system. This system amplifies the strain experienced by piezoelectric patches bonded to the beam to maximize the conversion from vibrational energy into electrical energy. Real-world applicability is tested using a wind tunnel to create vortex shedding and comparing the results to finite element modeling that shows the structural vibrational modes. A crucial part of this study is conditioning and storing the harvested energy, focusing on theoretical modeling, design parameter optimization, and experimental validation. The developed system is helpful in designing wind-induced energy harvesters to meet the necessity for novel energy resources.

WIND-INDUCED VIBRATION ENERGY HARVESTING USING PIEZOELECTRIC TRANSDUCERS COUPLED WITH DYNAMIC MAGNIFICATION

by

Austin Baker, Kathryn Connolly, Lauren Dorsey, Ian Grissom, Alden Grobicki, Kevin Keller, Chandan Kittur, Daniel Konecki, Mark Lee, Timothy Lee, Boheng Ma, Edward Mulhern, Andrea Ng, Mihir Patel

Thesis submitted in partial fulfillment
of the requirements of the
Gemstone Program
2014

Advisory Committee:
Professor Amr Baz, Mentor
Professor Balakumar Balachandran
Professor Johan Larsson
Dr. Ronald G. Polcawich
Dr. Robert M. Proie
Professor Norman M. Wereley
Professor Miao Yu

© Copyright by
Austin Baker, Kathryn Connolly, Lauren Dorsey, Ian Grissom, Alden Grobicki, Kevin Keller, Chandan Kittur, Daniel Konecki, Mark Lee, Timothy Lee, Boheng Ma, Edward Mulhern, Andrea Ng, Mihir Patel.
2014

ACKNOWLEDGEMENTS

We would like to thank our mentor, Dr. Amr Baz, and his graduate students, Dr. Mostafa Nouh and Mohamed Raafat and the other members of his lab. We would also like to thank our librarian, Nedelina Tchangalova. We want to acknowledge the ACCIAC and the Maryland Sustainability Fund. In addition, we want to give a huge thanks to all of the Gemstone staff. We want to recognize all of our family and friends who have supported us along the way.

Table of Contents

List of Figures vii

List of Tables x

1 Introduction 1

2 Literature Review 7

2.1 Energy Harvesting 7

2.1.1 Piezoelectricity 8

2.1.2 Fatigue 9

2.1.3 Vortex Induced Vibrations 13

2.1.4 Unimorph 16

2.1.5 Dynamic Magnification 18

2.1.6 Related Research 20

2.2 Energy Conditioning 21

2.2.1 Rectifier Circuits 22

2.2.2 Impedance Matching 24

2.3 Energy Storage 26

2.3.1 Battery Systems 26
2.3.2 Supercapacitor Systems 28
2.3.3 Supercapacitor and Li-ion Battery Hybrid System 30
2.3.4 Control Circuitry 32

3 Harvesting 35
3.1 Harvesting Methodology 35
3.1.1 Prototype Fabrication 35
3.1.2 Finite Element Analysis 37
3.1.3 Vibrometer and Shaker Testing 38
3.1.4 Wind Tunnel Testing 38
3.1.5 Performance without Magnifier 40
3.1.6 Performance with Magnifier 41
3.2 Harvesting Results and Discussion 41
3.2.1 Finite Element Analysis 42
3.2.2 Shaker Testing 43
3.2.3 Vibrometer Testing 45
3.2.4 Wind Tunnel Testing 47
3.2.5 Harvesting Discussion 51
3.3 Summary 52

4 Conditioning 54
4.1 Conditioning Methodology 54
4.1.1 Construction of the Rectifier Circuit Models 54

4.1.2 Tuning of the Rectifier Circuits 56
4.1.3 Running pSpice Simulations 59
4.1.4 Evaluating the Simulation Results 60
4.1.5 Construction of the Physical Rectifier Circuits 61
4.1.6 Experimental Setup 61
4.1.7 Collecting Experimental Data 64
4.1.8 Derivations for Piezoelectric Analog Model 66
4.2 Conditioning Results and Discussion 69
4.2.1 Data Analysis 70
4.2.2 Conditioning Discussion 74
4.3 Summary 78

5 Storage 80
5.1 Storage Methodology 80
5.1.1 Battery Selection and Initial Testing 80
5.1.2 Charging System 81
5.1.3 Battery Efficiency 84
5.1.4 Energy Measurement 85
5.1.5 Calculation of Efficiency from Measurements 86
5.1.6 Supercapacitor Hybrid System 87
5.2 Storage Results and Discussion 88
5.2.1 Initial Setup Results 88
5.2.2 Final Setup Results 89

5.2.3 Storage Discussion 93
5.3 Summary 96

6 Integration 97
6.1 Integration Testing 97
6.2 Data Analysis 98
6.3 Discussion 99
6.4 Potential Applications 100

7 Conclusion 102

Glossary 104

Bibliography 108

Appendices 116

List of Figures

1.0.1 U.S. Carbon Emissions from 1990-2010 1

1.0.2 Breakdown of U.S. carbon emissions by industry 2

1.0.3 Breakdown of U.S. energy consumption 4

1.0.4 Map of U.S. wind speeds 5

2.1.1 Piezoelectric effect 8

2.1.2 Phase Diagram for PZT 10

2.1.3 Effect of cyclic loading on PZT strain value 11

2.1.4 Relationship between cyclic loading of PZT and crack growth length . . 12

2.1.5 Vortex formation behind a bluff body 13

2.1.6 Effect of Reynold's number on vortex formation 14

2.1.7 VIVACE converter 16

2.1.8 Circuit model of a piezoelectric unimorph 18

2.1.9 Dynamic magnification system 19

2.1.10 Piezoelectric harvester designed by Dr. Francis Moon 21

2.2.1 Conditioning Circuit diagrams 23

2.3.1 Specific power and energy of different batteries 28

2.3.2 Power density and energy density for different storage systems 30

3.1.1 Wiring diagram of the piezoelectric harvester 36

3.1.2 CAD render of the piezoelectric harvester prototype 37

3.1.3 Ling/LDS V408 V-408 Low Force Vibration Shaker 39

3.1.4 Correlation between wind velocity and fan frequency 40

3.2.1 Bending modes of the beam with baseline configuration 41

3.2.2 Bending modes of the beam with dynamic magnification 42

3.2.3 Sine sweep of the beam in the baseline system 44

3.2.4 Sine sweep of the cylinder in the baseline system 44

3.2.5 Displacement color map of baseline beam 45

3.2.6 Displacement color map of the beam with dynamic magnification 46

3.2.7 Fast-Fourier transform of the output voltage of the baseline harvester . . 48

3.2.8 Peak voltage for two elastomers at optimal flow velocity 49

3.2.9 Peak voltage for two elastomers after optimal flow velocity 50

4.1.1 pSpice schematic for the SEH circuit. 55

4.1.2 pSpice schematic for the SSHI-P circuit. 57

4.1.3 Bode plot for gain and phase shift of differentiator 58

4.1.4 Effect of RVAL value on voltage 60

4.1.5 Image of resistor box 62

4.1.6 SEH circuit setup 63

4.1.7 Image of piezoelectric shaker setup for conditioning testing 63

4.1.8 Schematic for measuring a signal with the DAQ 65

4.1.9 Input voltage from the piezoelectric stripe 66

4.1.10 Diagram of model used to simulate the piezoelectric analog 67

4.1.11 Piezoelectric analog model calibration 69

4.2.1 Piezoelectric analog model voltage vs load resistance 71

4.2.2 Piezoelectric analog model power vs load resistance 72

4.2.3 Simulated output voltage for SEH and SSHI-P 73

4.2.4 Simulated output power for SEH and SSHI-P 74

5.1.1 Boost converter configuration 83

5.2.1 Breakout circuit designed for the MAX17710 89

5.2.2 Voltage profile of unexpected breakdown 91

6.2.1 Voltage across piezoelectric element at 56 Hz 99

6.2.2 Rectifier output for integrated circuit 100

List of Tables

4.1 SEH pSpice component legend 55

4.2 SSHI-P pSpice component legend 56

4.3 SSHI-P fixed component values 57

4.4 SSHI-P fixed component values 64

4.5 Value of parameters in piezoelectric model 68

4.6 Simulated and experimental peak power output 72

5.1 Discharge voltage ranges over time 90

5.2 Discharge of the battery over 3 hours 92

1 Introduction

Undisciplined and minimally restrained use of the Earth's natural resources for energy production has led to significant environmental damage. In order to reduce this environmental damage, great strides must be made in the field of renewable energy sources. Energy is currently produced primarily by burning fossil fuels such as coal, natural gas, and petroleum[50]. Although these processes are reliable energy sources, the natural resources which drive them are finite[20]. The byproducts of these processes can result in harmful climate changes including acid precipitation, stratospheric ozone depletion,

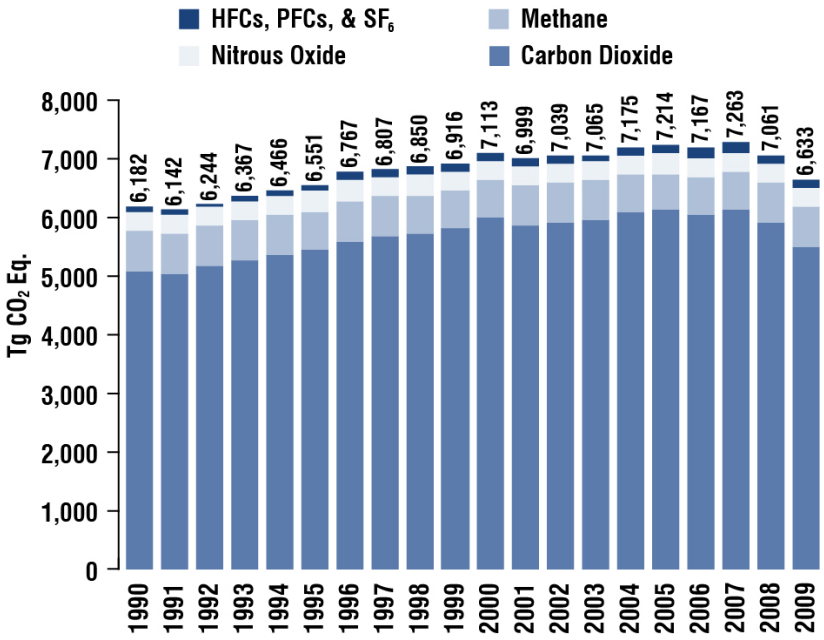

Figure 1.0.1: Carbon dioxide equivalent emitted by the US from 1990-2009.

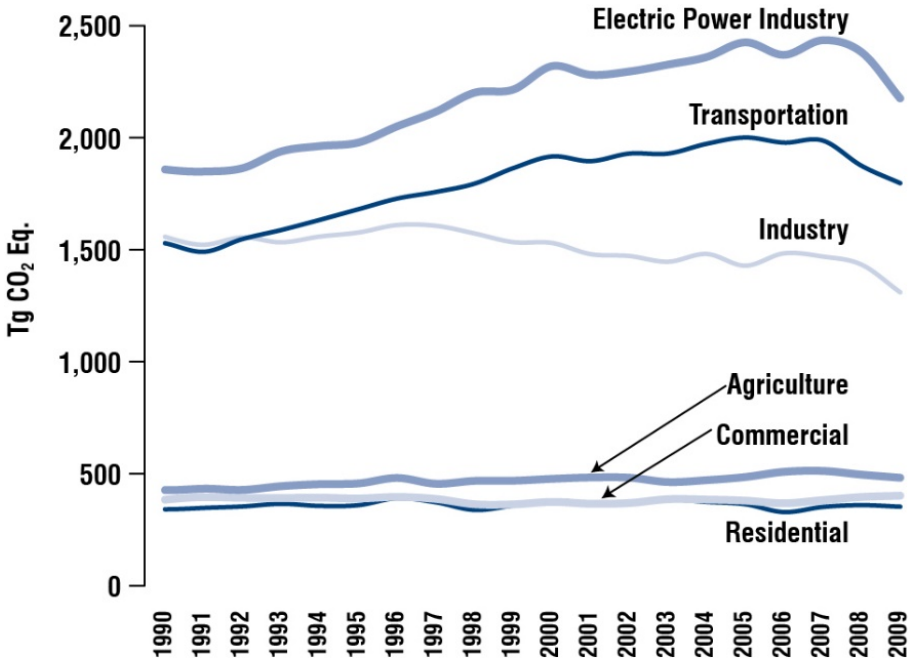

Figure 1.0.2: CO_2 emissions breakdown by industry in the U.S.

and the greenhouse effect[14]. According to the United States Environmental Protection Agency, greenhouse gases trap heat in the atmosphere, and an estimated fifty percent of this effect is attributed to the buildup of carbon dioxide[50]. Methane, chlorofluorocarbons, halons, nitrous oxide, ozone, and peroxyacteylnitrate produced in industrial processes make up the remaining fifty percent[14]. Because of the increasing amounts of greenhouse gases being emitted into the atmosphere due to human activities, the overall temperature of the earth is increasing over time. If current emission levels persist through the end of this century, the temperature of the earth could increase 2.0 to 11.5 degrees Fahrenheit above temperatures from the 1990s[50]. Climate variability has a detrimental effect on many natural and human processes, such as agriculture, precipitation patterns, and human health[1].

While methane, nitrous oxide, and hydrofluorocarbons are all greenhouse gases,

carbon dioxide, a byproduct of the burning of fossil fuels, makes up 83% of all the greenhouse gas emissions in the United States[50]. Figure 1.0.1 illustrates the amount of carbon dioxide released into the atmosphere from 1990 to 2009. Most of the carbon dioxide emissions resulted from burning fossil fuels, mainly coal. While carbon dioxide emissions have decreased since the early 2000s, a significant amount of the gas is still emitting into the atmosphere to this day[50].

The majority of these greenhouse gas emissions are a result of the electric power industry, which relies mostly on coal (Figure 1.0.2). Further exploration, development, and utilization of alternative energy sources are crucial to making society's energy dependence more sustainable and less harmful to the environment.

The U.S. Energy Information Administration (EIA) defines renewable energy as any source of energy that can regenerate and can be sustained indefinitely, and such sources include solar power, geothermal energy, and wind energy. Recent reports by the EIA state that from 2009 to 2011 renewable energy has only made an increase of 1% in the its share of the total primary energy production, from approximately 8% to 9% of the total energy consumed in the United States and 10.3% of the energy generated for electricity consumption[50, 49].

Wind power is an excellent candidate for renewable energy. Wind energy can be harvested at all times of the day, unlike solar power, which depends on the hours of daylight. Also, though wind is present at all times of year, other energy sources such as biofuels depend on seasonal variation and harvest yields. Among current renewable energy sources, wind power has had the least growth. According to the EIA, from 2009 to 2011, wind power experienced only a 2% increase for electricity produced from renew-

able sources (Figure 1.0.3)[49].

Most current wind energy harvesting devices are large turbines that utilize internal moving mechanical parts and require maintenance. In addition, these large turbines are centralized in the Midwestern United States due to the higher wind velocities that occur in that region (Figure 1.0.4). Wind turbines also cause problems for local wildlife, endangering all flying animals and affecting their ecosystems.

The U.S. Department of Energy reported in April 2011 that areas with annual average wind speeds around 6.5 m/s and greater at a height of 80 meters are generally considered to have suitable wind resource for wind development. According to Figure 1.0.4 Maryland, along with a majority of other states, does not receive adequate wind speeds

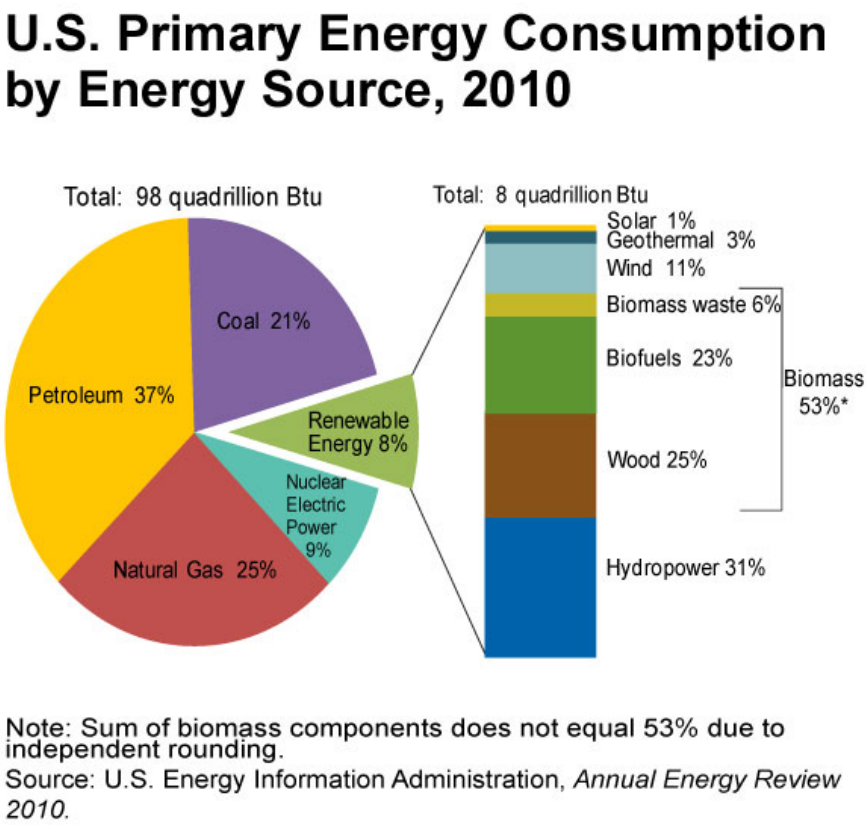

Figure 1.0.3: Breakdown of energy consumption in the U.S.

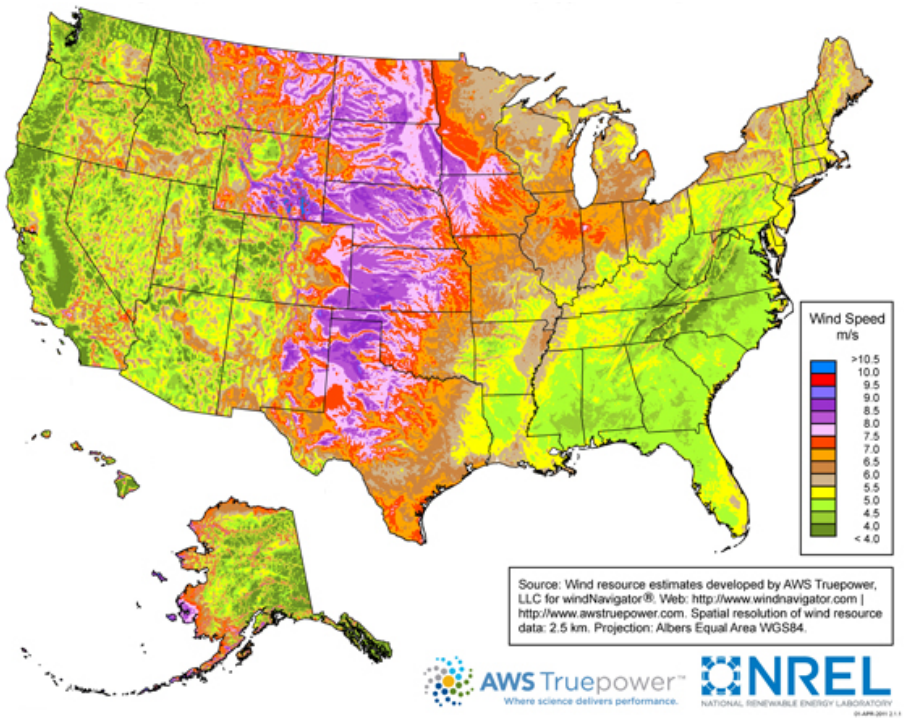

Figure 1.0.4: Average wind speeds across the U.S.

in order to viably utilize wind as an alternative energy source. To most effectively utilize regional differences in renewable resources, these resources will require implementation primarily on a local level in order to provide enough energy for the population[13]. While wind turbines require high wind velocities, there are practical alternatives for wind energy harvesting at lower wind velocities.

One possible implementation of an energy harvester uses piezoelectric materials to harvest energy from vibrations induced on a dynamically magnified bluff body by vortex induced shedding. This design lowers the required wind speed for energy harvesting dramatically, while the use of piezoelectrics as the energy converting element reduces the need for maintenance. Renewable energy sources throughout the nation comprise a minority of all energy produced in the U.S. In this study, a case is presented for using

piezoelectric-based wind energy harvesters because of their simplicity, reliability, and high conversion efficiency at low wind speeds.

2 Literature Review

The design of a new type of energy harvester is split into three categories, each of which addresses a separate component of the harvester: the energy harvesting device, the electrical conditioning circuitry, and the storage system. Extensive literature review in the fields respective to each of these categories has guided the design process of each subsystem.

2.1 Energy Harvesting

The design for the wind energy harvesting device is based on research for the best piezoelectric materials and on a structure that requires a minimal amount of maintenance and moving parts. The literature review includes research of specific piezoelectric materials, an examination of the properties compatible with the proposed application, the plausibility of an efficient, real world application based on wind data, the phenomenon of vortex induced vibrations (VIV), and the coupling of vibrations with dynamic magnification.

2.1.1 Piezoelectricity

Piezoelectric materials possess the unique ability to convert between electrical and mechanical energy. The piezoelectric effect occurs in certain materials when a mechanical stress is applied, causing the electrical charges in the molecules of the material to develop. As the material is deformed, the molecules realign in a manner that forms a surface charge density leading to voltage (Figure 2.1.1).

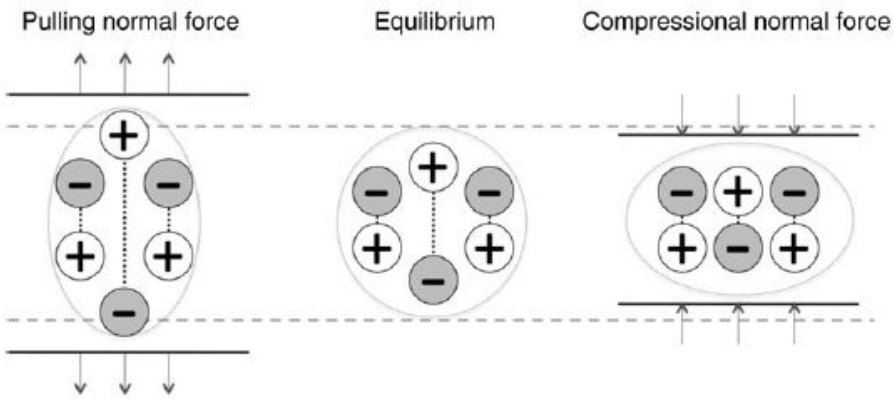

Figure 2.1.1: Piezoelectric effect

The converse piezoelectric effect is observed when an electrical charge is applied to a piezoelectric material[35]. The molecules are electrically inclined to create a dipole, thus causing a physical change in shape as the molecules realign. Piezoelectricity was first discovered in 1880 when the brothers Pierre and Paul-Jacques Curie observed that mechanical stress in certain materials such as tourmaline, cane sugar, topaz, and quartz resulted in the production of electric charge in the material. In 1881, Gabriel Lippmann predicted the converse effect using thermodynamic principles [4]. These properties can be found in crystalline materials such as quartz, bone, dentine, and sugar cane[35]. In modern day research and applications, piezoelectric materials are preferred for the immediacy

and simplicity of the transduction mechanism between the mechanical and electrical field [4]. The use of piezoelectric materials requires minimal incorporation of moving and quickly degrading parts.

Although there is a variety of piezoelectric materials, two types were considered for this design: ceramics and polymers. Ceramics, such as lead zirconate titonate (PZT), were first used as piezoelectric materials in 1947. PZT has now become the most commonly utilized ceramic piezoelectric material[42]. Although the piezoelectric properties of polymers were discovered in 1924, they were not used until the 1950s when researchers studied the strong piezoelectric properties of polyvinylidenefluoride (PVDF)[42]. Both materials have their advantages and disadvantages. Piezoceramics have a large strain response and therefore a high voltage output with piezoelectric constants of about 200 to 400 pC/N. The ceramics, however, are brittle and suffer from both high loss factors and highly hysteretic behavior [33, 38]. PVDF is much more flexible and can be modified easily to different dimensions of size and thickness, though it suffers from a lower piezoelectric constant of about 10 pC/N[33]. Despite the structural advantages of polymers, ceramics deliver greater voltage in response to mechanical strain, which is a primary goal of this design. Both materials were considered in this study to determine the best combination of the two for a specific range of wind velocities and frequencies.

2.1.2 Fatigue

Many piezoelectric materials were researched for the optimal electromechanical properties of an energy harvester. For use in sensors and actuators, piezoelectric materi-

als must have low dielectric and mechanical losses since the energy dissipation from these factors can change the physical properties of the material. They must also have high electromechanical coupling coefficients, which indicates a high conversion efficiency from mechanical strain to electrical charge[9].

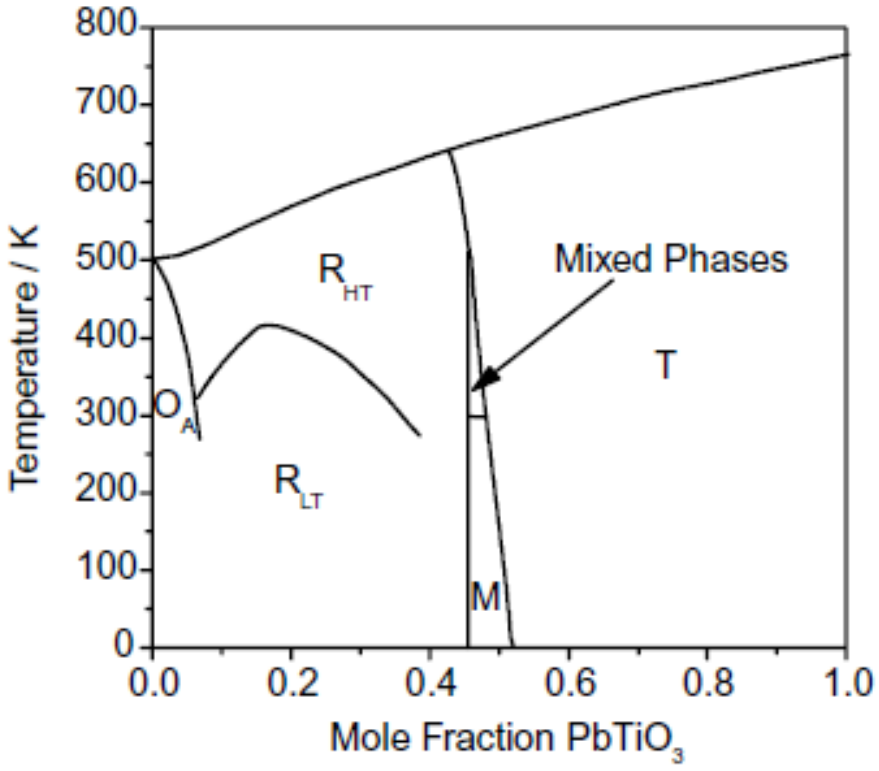

Figure 2.1.2: Crystal phases of PZT[9]

For most applications of PZT ($Pb[Zr_xTi_{1-x}]O_3\ 0 \leq x \leq 1$), the ideal performance occurs at the boundary between the tetragonal and rhombohedral perovskite phases, as seen in Figure 2.1.2. This is where the piezoelectric coefficients reach their maximum due to a peak in the spontaneous polarization, which is directly proportional to the intrinsic piezoelectric coefficient. In addition, the almost degenerate states of the tetragonal and rhombohedral structure allow the domains within the grains to be reoriented and aligned

through exposure to an electric field or by direct electrical poling. This reorientation maximizes the extrinsic piezoelectric contributions [9].

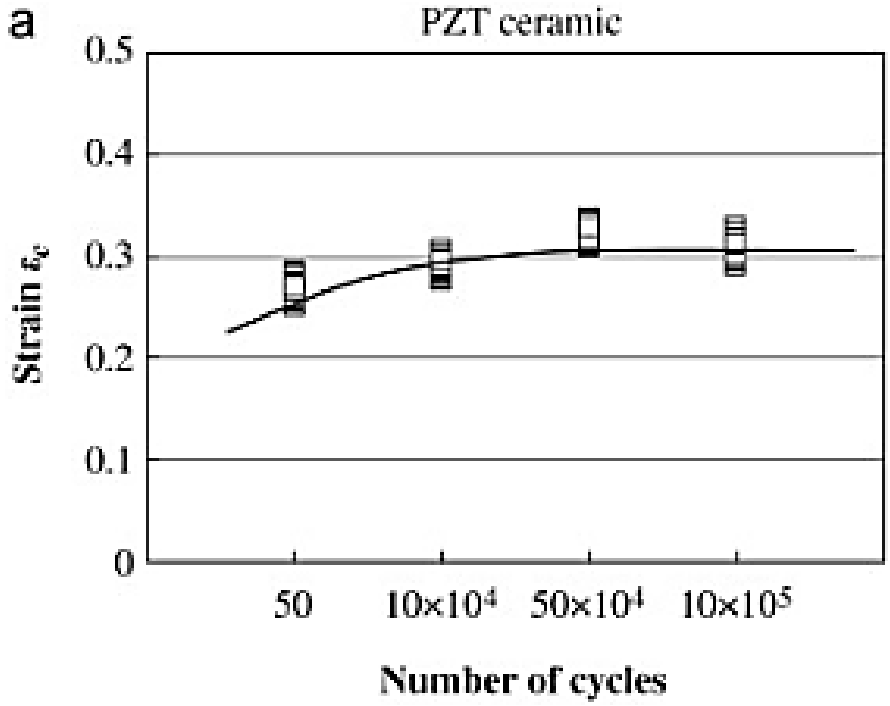

Figure 2.1.3: Strain value for PZT after cyclic loading

By substituting hardener or acceptor ions with lower valence states into the PZT system, the properties can be modified and diverge to hard or soft PZT. Hard PZT exhibits low losses and a high quality factor, but it only has modest values for the dielectric constant and piezoelectric coefficient. Alternatively, soft PZT exhibits a high dielectric constant and piezoelectric coefficient, but also exhibits high losses. Differences between the macroscopic properties of hard and soft PZT are caused by domain wall motion in piezoceramics [17].

The strain value increases with increasing cyclic loading, and settles after 50×10^4 cycles for the PZT ceramics, as seen in the Figure 2.1.3. The endurance limit for PZT

is at a stress amplitude of 180 MPa[39]. Figure 2.1.4 shows how crack growth length is affected by frequency of the load. The fatigue crack growth length increased nonlinearly during the cyclic loading, reaching its maximum at 5 kHz.

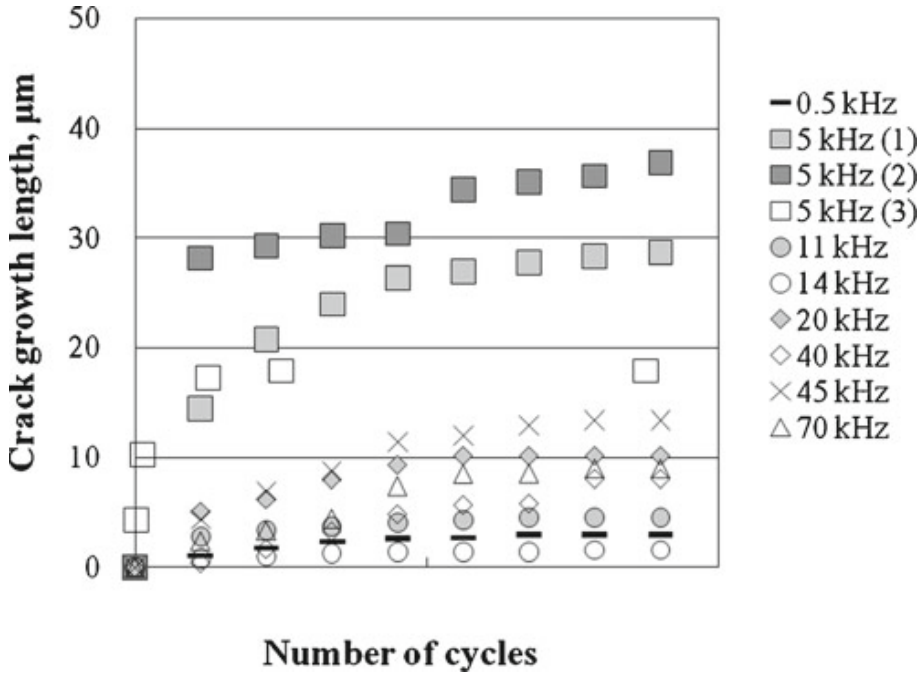

Figure 2.1.4: Cracks form in PZT during cyclic loading.

Electrically fatigued PZT with cyclic bipolar loading shows a large number of microcracks in the microstructure in regions near the surface, with the bulk showing no observable cracking. The loss in the polarization due to fatigue cracking can be regained by removing the affected surface layer to expose the internal bulk, meaning that these regions are largely responsible for the degradation of piezoelectric properties in PZT. After removing the load to 0 V the strain value becomes zero for PZT ceramics[34].

2.1.3 Vortex Induced Vibrations

Vortex induced vibrations(VIVs) occur when a bluff body rests in a flow within a range of Reynolds numbers from an approximate minimum value of 40 to an approximate maximum of 3×10^5 (Figure 2.1.5).

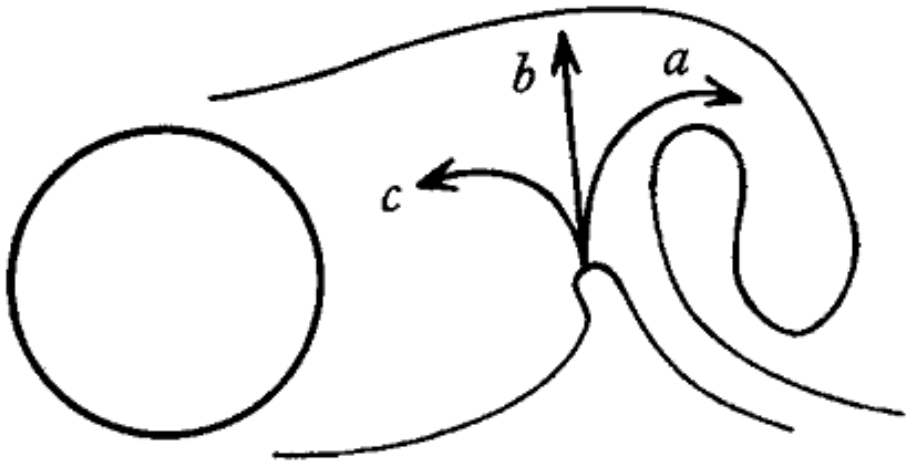

Figure 2.1.5: Vortex formation behind a bluff body[18]

Within these Reynolds numbers the flow splits apart so that the layers closest to the body start curving around behind it [11]. These layers, known as free shear layers, turn in opposite directions around the body [11]. As shown in Figures 2.1.6 and 2.1.5, these layers alternate in feeding a vortex until the vortex's rotation pulls the opposite shear layer across the object, thereby shedding the vortex and commencing the creation of the next vortex[18]. The end result is that vortices are created on alternating sides of the bluff body with a repeating frequency. The frequency at which the vortices are created is known as the shedding frequency and is dependent on the bluff body and the Strouhal number of the fluid [11].

The formation and shedding of a vortex causes the bluff body to experience unequal

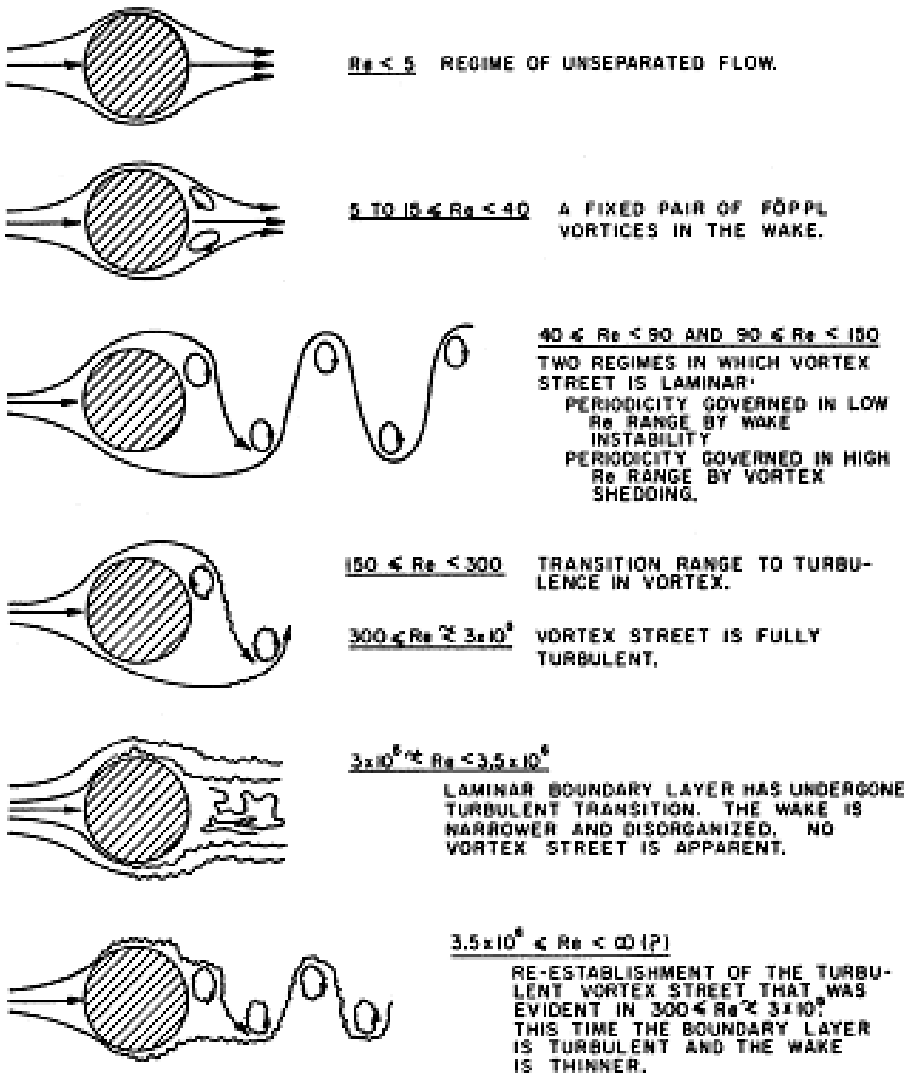

Figure 2.1.6: Air flow around a bluff body with varied Reynolds numbers[32]

pressures from different sides, leading the body to move back and forth perpendicular to the flow. This oscillating motion is greatest when the shedding frequency is equal to the natural oscillating frequency of the object[11]. These vibrations can be harvested by various means, including the use of piezoelectric materials and conventional mechanical generators[10, 46].

Vortex shedding from an oscillating bluff body is significantly different from that

of a fixed bluff body. In fact, the principles by which the incoming flow interacts with the bluff body alter when motion is either externally induced or vortex-induced[7]. One of the problems with vortex shedding on an oscillating bluff body is the difficulty in modeling the distributed force exerted by the fluid along the length of the body[8]. The oscillatory motion of the body makes analysis of the resultant force complex, so Bearman et al. utilized finite element modeling (FEM) of the bluff body in order to ensure the accuracy of the analysis. The bluff body and fluid involved in this study were a flexible cylinder and water and the primary quantities examined included the fluid forces and the lift and drag coefficients. The results of the study show that, based on a predetermined FEM, a force distribution analysis along the surface of a bluff body is plausible. Despite its success, the study emphasized that it utilized indirect measurement methods, and more direct measurement methods remain unavailable. Although the FEM provided solid groundwork in terms of a place to start for initial modeling, the exact details of the force distribution still require more clarity [8].

One example of a modern vortex-induced power harvester is the VIVACE converter developed at the University of Michigan [10]. The converter consists of a series of cylinders placed within a current of water, shown in Figure 2.1.7, which oscillate vertically like pistons in a motor, creating either usable electricity or hydraulic energy. The main fault with this project is that constant acceleration and deceleration of the cylinders caused by their oscillating motion, combined with friction between the parts, eventually damage the unit. Using piezoelectric materials to convert vortex induced vibrations into electricity eliminates the need for moving parts.

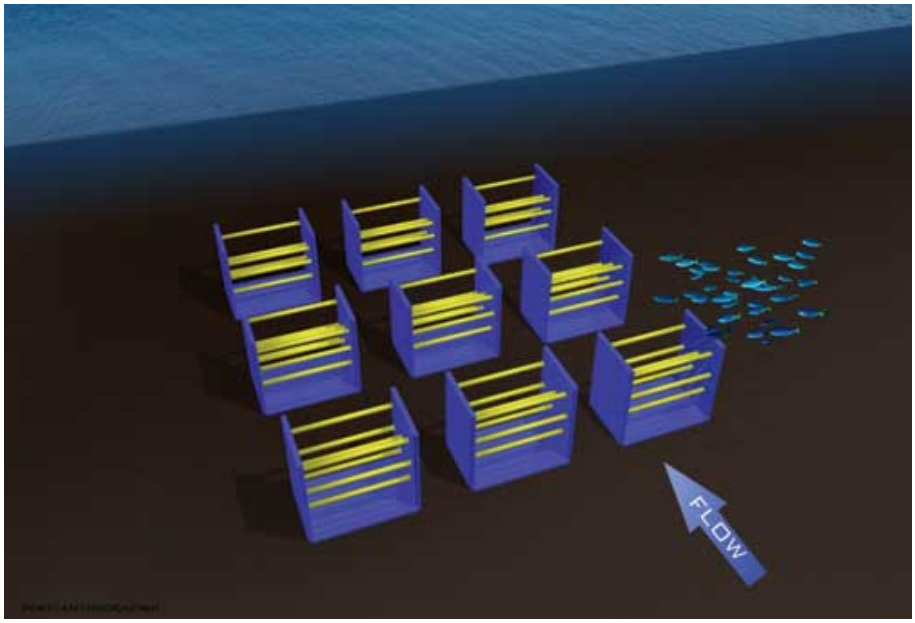

Figure 2.1.7: Model of the VIVACE converter[10]

2.1.4 Unimorph

The ceramic unimorph cantilever beam was identified as the most relevant design for the purpose of this project. The beam is fixed on one end and free on the other end, and the ceramic piezoelectric material is attached on top of the beam close to the fixed end. This ensures the highest strain because it is the location of the largest bending moment. A proof mass is also applied in order to increase the strain during the vibration[48]. Power is given by

$$P = \frac{m\xi A^2}{\omega}\left(\frac{\omega}{\omega_N}\right)\left[\left(2\xi\frac{\omega}{\omega_N}\right)^2 + \left(1-\left(\frac{\omega}{\omega_N}\right)^2\right)^2\right]^{-1} \tag{2.1.1}$$

where P is power, m is the mass, ξ is the damping coefficient, ω is the operating frequency, ω_N is the natural frequency, and A is amplitude of the acceleration. The optimal

resonance power, when the operating frequency equals the natural frequency, is given by

$$P = \frac{m\xi A^2}{4\omega_N \xi^2} \tag{2.1.2}$$

The natural frequency is determined by calculating the transverse stiffness and effective mass using

$$k_0 = W\left[\frac{G_b h_b^3}{12} + 2G\left(\frac{h_p^3}{12} + \frac{h_p(h_p+h_b)^2}{4}\right)\right]\left(\frac{\pi}{L}\right)^4\left(\frac{L}{2}\right) \tag{2.1.3}$$

$$m_{eff} = m_{proof} + \frac{WL}{2}(\rho_b h_b + 2\rho_p h_p) \tag{2.1.4}$$

$$\omega_N = \sqrt{\frac{k_0}{m_{eff}}} \tag{2.1.5}$$

where W and L are the width and length respectively. G is the young's modulus, h is the thickness and ρ is the density. The subscript b denotes the beam and the p denotes the ceramic piezoelectric material. The length, width, thickness, and proof mass need to be optimized to match the operating frequency in order to get the largest power.

The piezoelectric unimorph can be modeled as a circuit as shown in Figure 2.1.8 where the energy conversion is modeled as a charge source. The piezoelectric ceramic acts like a capacitor(C_p), and the parallel resistance(R_d) models the dielectric leakage. This is then used to charge a storage device. The electric power is given by the following equation.

$$P_{elec} = C_p V_{peak}^2 f_d \tag{2.1.6}$$

The peak voltage is the voltage at maximum compression of the ceramic where f_d is the operating frequency. The efficiency of the conversion from electrical to mechanical energy is given by the following equation.

$$\nu = \frac{C_p V_{peak}^2}{Fd} \tag{2.1.7}$$

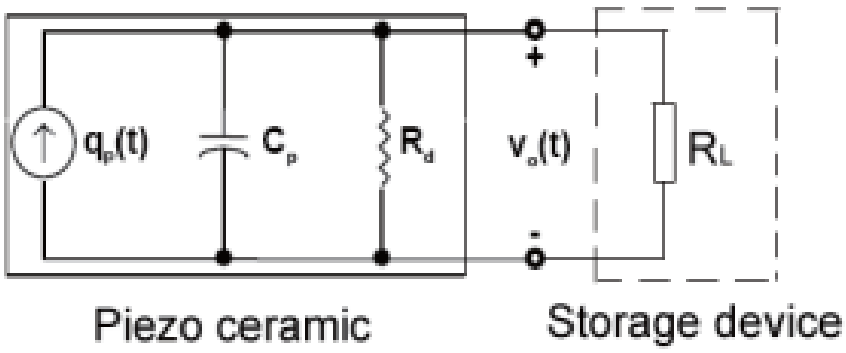

Figure 2.1.8: Circuit model of a piezoelectric unimorph[48]

F is force and d is displacement. The efficiency can be experimentally determined. Using this efficiency and the resonance power, the peak voltage can be predicted.

2.1.5 Dynamic Magnification

The basics of simple harmonic motion lead into the concept of dynamic magnification. The main differential equation governing a simple harmonic oscillator is given by

$$m\ddot{x}(t) + c\dot{x}(t) + kx(t) = f(t) \tag{2.1.8}$$

where m is the mass of the oscillator, c is the viscous damping coefficient for the system, k is the oscillator stiffness and $f(t)$ is the applied force with respect to time[19].

These properties lead to the following relations:

$$\omega_0 = \sqrt{\frac{k}{m}} \tag{2.1.9}$$

$$\xi = \frac{c}{2m\omega_N} \tag{2.1.10}$$

where ω_N is the natural frequency and ξ is the damping ratio.After substitution of Eq. 2.1.9

and Eq. 2.1.10 into Eq. 2.1.8 the following is obtained

$$\ddot{x}(t) + 2\xi\omega_N\dot{x}(t) + \omega_N^2 x(t) = \frac{f(t)}{m} \tag{2.1.11}$$

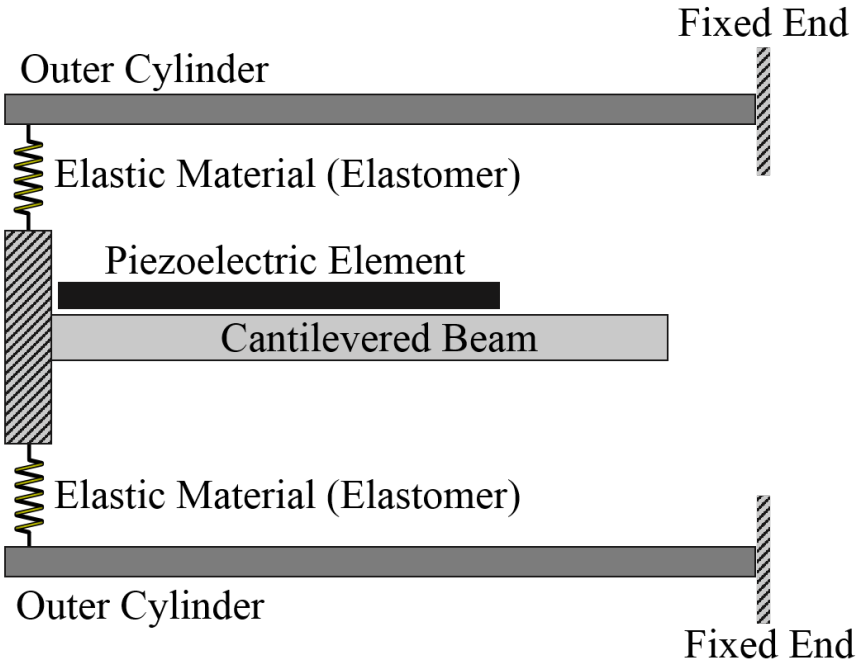

Figure 2.1.9: Dynamic magnification system configuration

The main structure in the system is referred to as the tube and the beam-mass system used to magnify the oscillations is referred to as the auxiliary beam or simply the beam. This beam configuration is demonstrated in Figure 2.1.9. The concept of dynamic magnification is similar to the idea of a tuned mass damper. The difference, however, lies in choosing auxiliary beam properties that will generate maximum amplitude in the oscillations of the auxiliary beam rather than dampen the amplitude of the primary beam oscillations.

In previous experiments, there has been success in magnifying both the system's first mode, as done by Aldraihem and Baz, and in the magnification of multi-mode oscil-

lations, as in the experiments conducted by Zhou et al[2, 51]. In the latter experiments, the addition of an optimized tuned mass damper increased the harvested energy to 25.5 times that of a single beam energy harvester[19]. This maximum magnification was achieved by adjusting the length of the auxiliary beam and the mass attached to auxiliary beam until both the primary and auxiliary structure had the same natural frequency.

In the single mode experiments conducted by Aldraihem and Baz, it was shown that the maximum energy harvested can be magnified by a factor of 20 using a tuned dynamic magnifier. This maximum was reached by adjusting the auxiliary beam properties until it resonated with the primary beam.

With preliminary figures for the dimensions of the primary structure and the auxiliary beam, it is possible to complete a comprehensive finite element analysis where the structure is theoretically tuned by adjusting the proof mass and the length of the auxiliary beam[51].

2.1.6 Related Research

While the design of the prototype and dynamic magnification system described in this report is novel, piezoelectric energy harvesting research is both an established and rapidly growing field. At Cornell University, Dr. Francis Moon leads a team of undergraduate engineering students in designing a piezoelectric energy harvester comprised of an array of foam masses on cantilevers that vibrate in wind. In Figure 2.1.10 below, the energy harvester is positioned on the roof of a building to maximize wind exposure and energy harvested. The team from Cornell sees a future for similar arrays since the

design is both more space efficient and less expensive than traditional wind energy harvesters like turbines. In addition to using piezoelectric materials to harvest the vibrational energy, the team is examining the feasibility of an electromagnetic apparatus for energy conversion. This option could also be a viable opportunity for future research for the harvester constructed by Team PRESSURE[27].

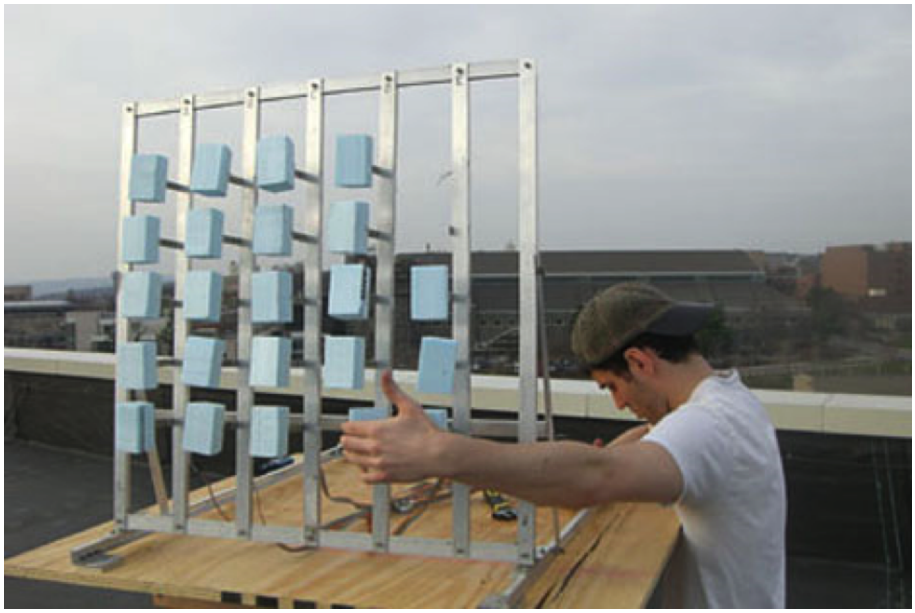

Figure 2.1.10: An undergraduate researcher adjusts the piezoelectric array

2.2 Energy Conditioning

The power harvesting capabilities of piezoelectric harvesters have improved through optimization of the conditioning circuits. The current produced directly from a piezoelectric energy harvester is not easily stored, as electrical energy is best stored by a direct current (DC). Therefore, the alternating electrical output from the harvester must be conditioned by a rectifier circuit to produce stable DC output. The rectifier circuit serves as

an efficient and effective intermediary between the harvesting and storage components of the harvester.

2.2.1 Rectifier Circuits

Early designs for rectifier circuits utilized diodes and capacitors to convert alternating current to direct current. These conditioning circuits employed standard passive diode rectification to condition signals. However, conditioning circuits that utilize active rectification, which adds switching elements to the rectifier, were found to increase the efficiency of power transfer by up to 400%. In these circuit designs, the switches are typically synchronized with the vibrations of the harvester by monitoring the voltage on the piezoelectric element of the harvester.

In most cases, the switches are turned on for high voltages to allow for energy storage and turned off for low voltages to prevent loss[3]. These two types of rectifier circuit designs are known as the standard energy harvester (SEH) and the synchronous switch harvesting on inductor (SSHI). As seen in 2.2.1a, the SEH consists of a standard full-bridge rectifier circuit coupled with a resistor and a capacitor in series.

The main goal of SSHI circuits is to synchronize the changes in voltage with the changes in current in a piezoelectric material. In normal piezoelectric materials the capacitance will result in a -90° phase shift between the voltage and the current, so an SSHI circuit uses an inductor and a switch to remove the phase shift[41]. The SSHI is formed by placing a branch with an inductor and a switch in parallel or in series to the traditional SEH circuit, as shown in 2.2.1b. The switch is thrown during the peak of the incoming

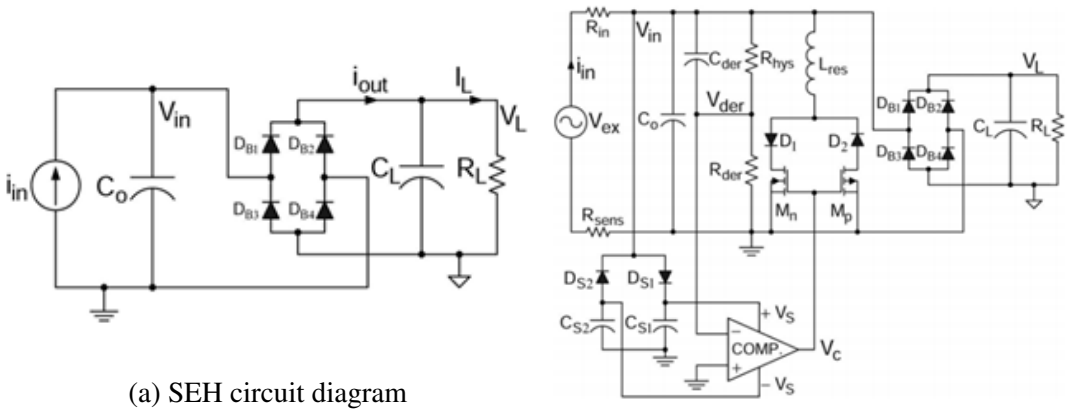

(a) SEH circuit diagram

(b) SSHI circuit diagram

Figure 2.2.1: Conditioning circuit diagrams[28]

voltage signal, allowing the inductor to resonate with the piezoelectric material's capacitance, resulting in the inversion of the piezoelectric material's voltage. This results in a higher power output because the capacitor starts in a charged state which is related to the inversion factor of the circuit[41].

One method of detecting the peak at which the switch should be thrown is through the use of a differentiator. When the differentiated signal is zero, the voltage has reached a peak. A simple differentiator can be devised using a resistor and capacitor, but suffers from low gain, so a more effective design is one using an op-amp as a differentiator and a Schmitt Trigger as a comparator. When powered by external sources, the design experiences a 230% improvement when compared to the standard diode bridge. When self-powered, the design experiences a 118% power improvement from the standard diode bridge[28].

SEH, SSHI-series, and SSHI-parallel circuits have a number of advantages and disadvantages. For weakly coupled systems, both the SSHI-series and parallel circuits pro-

duce optimal power outputs which are much greater than the SEH method. For medium range coupled systems, the peak power is comparable for all three circuits, though SSHI is less sensitive to frequency changes[44]. For strongly coupled systems, all three methods have similar peak optimal power outputs. The series-SSHI circuit experiences a significant loss in performance in weakly coupled systems when diode loss is accounted for[31]. The SSHI circuit also has voltage losses due to switching circuitry, voltage gap, and switching phase delay[41].

2.2.2 Impedance Matching

Maximum efficiency is obtained by using complete impedance versus incomplete impedance matching. The difference between incomplete and complete impedance is whether or not the reactive impedance is accounted for. Impedance can be divided into two types: real and reactive. The reactive capacitance causes the voltage and current coming from the mechanical system to be out of phase. The power of the system is maximized when the phase between the current and the voltage is zero. This can only be achieved through complete impedance matching. In order to obtain complete impedance matching, the input impedance of the electrical transmission system must be the complex conjugate of the output impedance of the mechanical system. Incomplete impedance matching is when only the real part of the impedance is matched and the reactive part is neglected. Using complete matching instead of incomplete matching can result in a 20% increase in power [12]. Constrained matching is maximizing the harvesting power subject to the constraints on the reactance of the electrical part, the resistance of the dissipative

component of the electrical part and the resistance of the harvesting component of the electrical part. Constrained matching is more effective than free matching in a non-ideal setting[30]

The real impedance from the mechanical system comes from the mechanical stress as well as the resistive element of the piezoelectric material, while the reactive impedance comes from the capacitive element of the piezoelectric material. This capacitive element inherently shunts some of the current flow, causing a significant drop in output power.

One possible solution for correcting this impedance mismatch is to include an inductor in parallel with the piezoelectric generator. However, there are numerous problems that arise when considering this solution. Both the impedance of the inductor and the impedance of the capacitor are frequency dependent, so any shift in frequency other than the resonant frequency causes an impedance mismatch. Additionally, only uncharacteristically large inductances, typically over 1 H, completely cancel the capacitive element. Generating such a large inductance would be impractical as the inductor's size would be large relative to the system[28].

Another possibility is joining a capacitive element in parallel with an even larger external capacitor, which drastically reduces the amount of inductance necessary to cancel the capacitive impedance. However, this setup has an extreme frequency dependence due to the large capacitance. By adding the external capacitance, the system will generate large reactive currents, forcing large losses in power[28].

2.3 Energy Storage

The final component of the energy harvester is the storage system. The storage system must be capable of storing the energy rectified by the conditioning circuit. Potential storage systems include batteries and supercapacitors controlled by smart chargers that can prevent overdischarges and provide regulated outputs.

2.3.1 Battery Systems

Common rechargeable battery systems used for energy storage include lead acid (Pb-acid), nickel metal hydride (NiMH), nickel cadmium (NiCd), sodium sulfur (NaS), sodium metal hydride (NaMH), and lithium ion (Li-ion). Characteristics relevant to the performance of a battery system include its energy capacity, power capacity, energy density, life span, operating temperature, and rate of self-discharge.

Energy capacity refers to the total energy that a battery can hold. Power capacity is the maximum rate energy can be transferred into or out of the battery over time. Energy density and power density are the energy and power capacities per unit volume, respectively. High energy and power capacity are desirable in a battery. The life span of the battery is the number of charge and discharge cycles the battery can be cycled through before it must be replaced. The operating temperature is the optimum operating temperature of the battery. High temperatures decrease lifespan, while low temperatures decrease battery capacity for most batteries. Rate of self-discharge is the amount of energy dissipated from the battery over time when it is not connected to a load[16].

Each battery system has different storage properties. Lithium-ion, NiCd, and NaS

batteries have the highest power density among batteries. NiCd and Pb-acid batteries are excellent pulsed power suppliers, but are large and heavy. In addition, NiCd and Pb-acid batteries have high energy densities but are difficult to recharge. Since NiCd and Pb-acid batteries are difficult to recharge, they do not perform well in applications where the batteries require recharging many thousands of times in a lifespan. NaS batteries are smaller and lighter than NiCd batteries[15]. They also have high energy density, high cycling flexibility, low maintenance requirements, and high coulombic efficiency. However, NaS batteries are sensitive to overcharging and overdischarging and operate at very high temperatures, ranging from $270°$C - $350°$ C [16]. Their constant heat input requirement is inconvenient and unrealistic for a self-sustaining system[15].

Li-ion batteries hold the greatest potential in terms of battery storage systems. Li-ion batteries outperform NiMH, NiCd, and Pb-acid batteries in providing energy and holding high specific power by at least a factor of 2.5, as shown in Figure 2.3.1 [16, 47]. They are particularly valuable because of their small size, light weight, high energy density, as well as their high output voltages and high storage efficiency [16, 15]. Li-ion batteries have a low self-discharge while not in use, one of the highest energy-to-weight ratios, and suffer less from memory effect. In addition, they have a long life cycle and rate capability [16]. The disadvantages of Li-ion batteries include high cost and a self-damaging effect when deeply discharged. When this occurs, the battery lifetime can drop to hazardously low levels[15]. Li-ion batteries prefer partial discharge to deep discharge, which does not lower the energy capacity since they exhibit little memory effect. Despite the disadvantages of Li-ion batteries, they remain the superior battery device for the design.

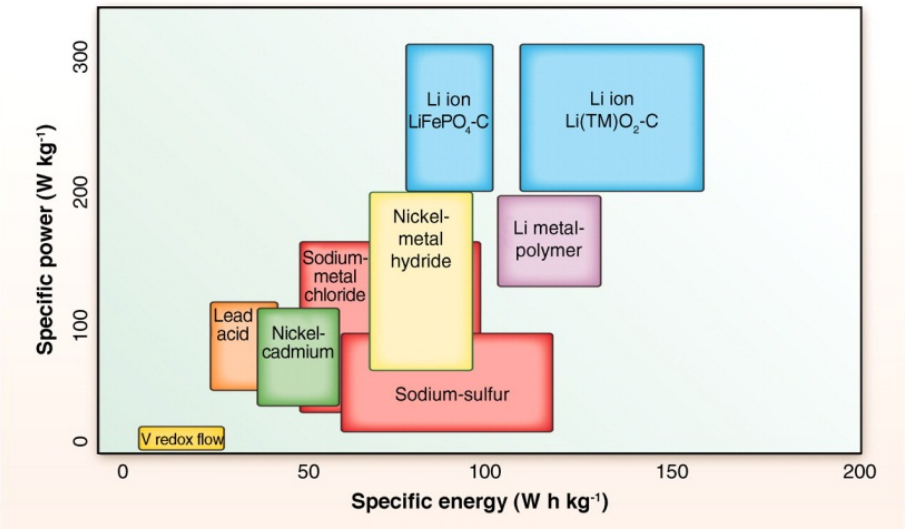

Figure 2.3.1: Specific power and energy of different batteries[16]

2.3.2 Supercapacitor Systems

Supercapacitors, also known as ultracapacitors and electrochemical capacitors, have been used successfully in a number of applications. Supercapacitors are used for regenerative braking in transportation vehicles, for consumer products such as cell phones and cameras, and for solar and wind energy harvesters[26].

The structure of a supercapacitor allows for capacitances 100 to 1000 times greater than those of traditional capacitors[5, 22]. Their large capacitance makes supercapacitors a viable energy storage option for various applications. A supercapacitor can be electrically modeled as two capacitors with an internal resistance in series; however, this resistance is nominal compared to the internal resistance of a battery cell. Because of their lower resistance, supercapacitors can have over ten times the power densities of normal batteries[5].

While supercapacitors can operate in a relatively wide range of temperatures and

voltages, -40°C to 85°C and 0.8 to 2.0 volts per cell, they are operated well within these ranges to prevent the lifetime from being significantly shortened[5, 25]. For every 100 mV or 10°C that a supercapacitor is operated at above its rated voltage and temperature, the lifetime of the supercapacitor is halved[22]. In addition, if the supercapacitor is operated outside its voltage range, chemical reactions may begin to occur, causing the supercapacitor to act more like a battery. The oxidation and reduction reactions result in the formation of impurities within the cell which decreases the lifetime and capacitance of the supercapacitor[5].

Unlike batteries, which store energy through chemical reactions within the cell, supercapacitors physically store and transfer charge across the electrode plates. This means that supercapacitors can last through hundreds of thousands of cycles, while batteries have a significantly shorter lifetime[5]. The Ragone chart in Figure 2.3.2 below depicts the relationship between energy density and power density for batteries and supercapacitors. From this chart, it is evident that double layer supercapacitors store less energy than batteries, but they can discharge at a much faster rate[29]. In addition, supercapacitors have a power density in the range of 18 kW/kg, significantly higher than that of a Li-ion battery. A supercapacitor's ability to charge and discharge in tens of seconds is beneficial for many applications, especially those in which there is a variable source and load, such as harvesting energy from varying renewable energy sources like the sun and wind. Batteries, on the other hand, take hours to fully charge or discharge. However, supercapacitors lack an energy density as high as that of batteries; therefore, for large energy storage needs batteries are more suitable[25].

Supercapacitors are a viable energy storage option over batteries due to their high

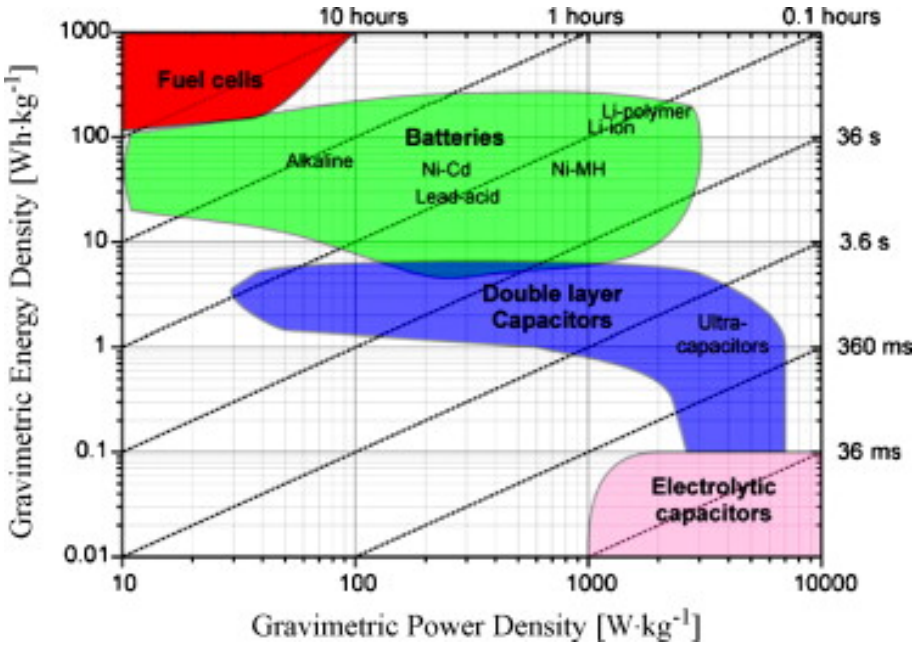

Figure 2.3.2: Power and energy density for different storage systems[29]

power density, wide operating temperature range, and long lifetime; however, there are some disadvantages of supercapacitors that must also be considered. Supercapacitors are ideal for applications requiring a rapid discharge, but not for those requiring slow and steady power discharge. Many potential applications of a piezoelectric device require a storage system to discharge energy at a steady rate. A supercapacitor is unable to store a large amount of energy due to its low energy capacity, making it unsuitable as the sole energy storage system[26].

2.3.3 Supercapacitor and Li-ion Battery Hybrid System

A hybrid system with both a Li-ion battery and a supercapacitor has the desirable characteristics of both. Qualities such as the long lifetime and large range of operating temperatures of supercapacitors are complemented by the high energy density of Li-ion

batteries. A Li-ion battery generally limits the longevity of a storage system. However, using a supercapacitor to manage the charging of the Li-ion battery increases the lifetime of the storage system[40]. Li-ion batteries typically undergo a charge cycle that begins with a constant current charging period followed by a constant voltage charging period until a full state of charge (SOC) is reached. The constant current charging period charges 70%-80% of the battery in 20%-30% of the total charge time, while the constant voltage charging period charges the remaining 20%-30% in the remaining charge time. In order to increase the longevity of a Li-ion battery, charging should occur at a constant, low current; the number of charge/discharge cycles should be as low as possible; and the battery should not undergo irregular charging in the constant voltage stage, as this decreases battery lifetime[40].

A supercapacitor reduces the number of cycles experienced by the battery by smoothing out the fluctuations in power from the source, thus extending the longevity of the system. Coupling supercapacitors to the Li-ion battery in the storage system reduces the rate capacity effect in the battery and increases the peak current that is provided to the load. Repeated high current discharges also reduce battery lifetime and thereby the longevity of the storage system. The supercapacitor can store energy from the battery during low load periods and release the extra energy necessary during high load periods. This allows the entire system to provide a higher overall peak discharge current while not exceeding the peak discharge current allowed for the Li-ion battery[24]. Using such a system increases the energy density of the system by up to 8% and extends the serviceable lifetime of the storage system[43].

Energy density, mass, and cost are important considerations for sizing a supercapac-

itor in a hybrid system. A larger supercapacitor helps decrease the battery's peak charge and discharge rates, leading to a longer system lifespan; however, because supercapacitors have a low energy density, the energy density of the system is also reduced[43]. A hybrid system can achieve higher power than a battery or supercapacitor alone because higher peak currents are produced when the two are coupled. A supercapacitor also increases the energy storage capacity of the overall system by over 20% in pulsed or fluctuating loads as compared with systems with only a Li-ion battery. This occurs because during pulsed loads, the supercapacitor supports the voltage provided by the battery during the time that the load draws current[24]. The overall capacity of the hybrid system as compared with a battery without a supercapacitor remains relatively unchanged because the supercapacitor can store little energy compared to the Li-ion battery.

The addition of a supercapacitor to a Li-ion battery not only increases the peak current delivered, but also regulates the charge and discharge of the battery in order to extend the battery lifetime, which decreases the total life cycle costs of the piezoelectric harvesting system. When sizing the supercapacitor for a hybrid system, design factors include peak load current, typical input power, and battery specifications.

2.3.4 Control Circuitry

A control circuit is important for regulating the power entering the energy storage system. When energy enters the system, an initial capacitor or supercapacitor charges up to a threshold voltage, after which charge is allowed to flow to the Li-ion battery. The voltage of the battery is controlled to prevent overcharging the battery. When there

is insufficient input power to charge the battery, the voltage of the supercapacitor drops significantly, so the cycle terminates. In the hybrid system, the charge on the battery is preserved until the supercapacitor discharges below a threshold voltage and the battery enters a discharge cycle to supply energy to the load[40]. A similar algorithm can be used in energy management circuits to ensure the longevity of a Li-ion battery. Ongaro et al. utilized this algorithm in an energy management and storage system for a photovoltaic array, which also experiences varying input power depending on weather conditions. This study found that the number of charge/discharge cycles decrease by a factor of four when utilizing a supercapacitor and Li-ion hybrid system.

Another component of control circuitry is the boost or DC-DC step up converter, which can greatly increase the effectiveness of a storage system. DC-DC converters are commonly used to regulate the output from highly variable sources such as wind sources and solar cells. Switch mode converters include boost converters, which step a voltage up, buck converters, which step a voltage down, and buck-boost converters, which regulate a voltage either higher or lower. Each uses a capacitor, an inductor, and a switch with other components. The inductor or capacitor is used to store energy, which is released when the switch changes position, thus enabling a higher output voltage to be realized from a lower input voltage. The coupling inductor is crucial to the performance of the design, and depending on the circuit, the power efficiency of the converter ranges between 67% and 86%[37].

There are a variety of DC-DC converters commercially available that could be used to integrate low voltage systems such as a supercapacitor with otherwise incompatible voltages such as a battery. For example, Linear Technologies' LTC3533 buck-boost con-

verter operates at input and output voltages of 1.8 V to 5.5 V with efficiencies of up to 96%. The LTC3785 is a similar device that has been shown to produce 3.3 V at 3 A from a 2.7 V to 10 V input source with efficiencies as high as 96%[23]. The efficiency and power consumption of the DC-DC converter are important factors to consider in the design of the storage system.

3 Harvesting

The purpose of the harvesting system is to design an energy harvester that utilizes piezoelectric materials to convert mechanical energy from vortex induced vibrations to electrical energy. A comprehensive model of a system with dynamic magnification is generated to accurately simulate prototype behavior under varying conditions. Additionally, the experimental performance of a dynamic magnifier is compared to that of a baseline energy harvester.

3.1 Harvesting Methodology

In this section, fabrication of the prototype, testing facilities and experimental methods are discussed. CAD models, simulation parameters and instrument specifications are presented. Finally, baseline and dynamic magnification configurations are explained.

3.1.1 Prototype Fabrication

In order to determine the transferability of theoretical results to real world applications, a small scale prototype harvester was constructed. To construct the prototype leads were soldered to the top and bottom contacts of four 2.25" PZT-5H bimorphs. The ceramic PZT-5H was purchased from APC International. These piezoelectric samples

were then secured to the top and bottom of a 10.75” acrylic magnifier beam using epoxy. To harvest energy from all four piezoelectric elements, the elements were connected in a manner such that their voltage potentials were summed. The inner surfaces were wired to a ’positive’ lead, and the outer surfaces were wired to a ’negative’ lead. The bending of the cantilever beam due to external vibrations caused the inner surfaces to be in compression and the outer surface to be in tension. The corresponding setup can be seen in Figure 3.1.1.

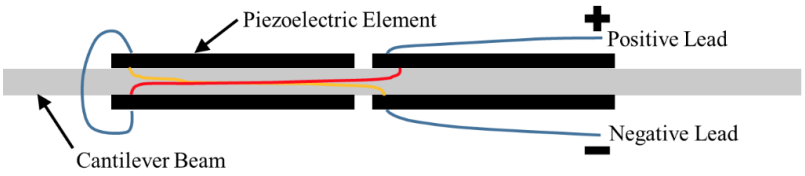

Figure 3.1.1: Wiring schematic of the piezoelectric harvester

The beam was then epoxied to a base plug as defined by the cantilever design. In order to create dynamic magnification, a rubber ring design was selected to serve as a sleeve for the base plug. Three different types of elastomer tubing purchased from McMaster-Carr were cut to lengths of 3/8” (creating rings). To assemble the harvester, the beam-plug-elastomer system was then inserted inside the free end of a cantilevered plastic cylinder. The plastic cylinders for the harvester structure were purchased from Uline Shipping Supply Specialists. At the fixed end of the cantilevered plastic cylinder, the base contained a small sleeve for stabilization, and duct tape was used to further secure the connection. The base for the cylinder and the base plugs were fabricated using a rapid prototyping machine in the Mechanical Engineering Prototyping Lab (ProtoME). The prototype base and plugs were custom designed using SolidWorks. The wire leads

from the ceramic piezoelectric were taped to the inner walls of the cylinder to reduce any negative effects due to damping. A computer-aided design (CAD) model and a photo of the prototype are shown in Figure 3.1.2.

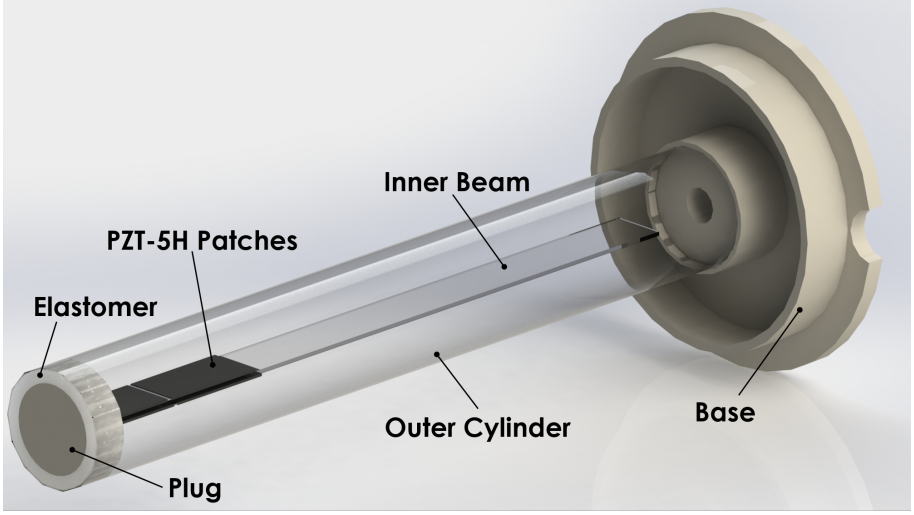

Figure 3.1.2: Labeled CAD render of the harvester prototype

3.1.2 Finite Element Analysis

Following prototype fabrication, a CAD model was created in the engineering simulation software ANSYS to complete finite element analysis (FEA) of the structure. The necessary material properties for each element were measured or determined from prior research, and these physical dimensions and material properties were imported into ANSYS. The CAD model was virtually excited across a range of frequencies to determine the theoretical natural modes of the beam, cylinder, and coupled beam-cylinder assembly. These results were then compared with later experiments to determine the validity of the experimental results.

3.1.3 Vibrometer and Shaker Testing

The highest voltage output is obtained when the structural frequency of the harvester is matched to the vortex shedding frequency. To test the natural modes of the beam and cylinder, the energy harvester was fixed to a shaker device, as shown in Figure 3.1.3, so that the beam was orthogonal to the shaking directional axis. This allowed the determination of the frequency of the first, second and third bending modes for both the beam and the cylinder, which the harvester experiences when undergoing vortex shedding. A dynamic signal analyzer, SR785 – 100 kHz 2-ch. FFT analyzer, was used to drive the shaker at multiple frequencies. In addition, the signal analyzer was used initially to perform sine sweeps and obtain the frequencies of the natural bending modes of both the beam and cylinder. These frequencies were then tested using a PSV-200, OFV-055, Scanning Vibrometer. White reflective tape was applied along the desired test section, which spanned the entire length of the beam or cylinder, so that the vibrometer could measure the displacement corresponding to each of the measured frequencies. The results from the laser vibrometer data were used to verify whether these frequencies correspond to the correct bending modes.

3.1.4 Wind Tunnel Testing

The laboratory used for the wind tunnel testing of the prototype was the Edwin W. Inglis '43 Thermal Fluids Instructional Laboratory at the University of Maryland. Flow in the wind tunnel was created by a large fan that could be set to different fan frequencies to modulate the test-section wind speed, as seen in Figure 3.1.4. Wind velocities inside the

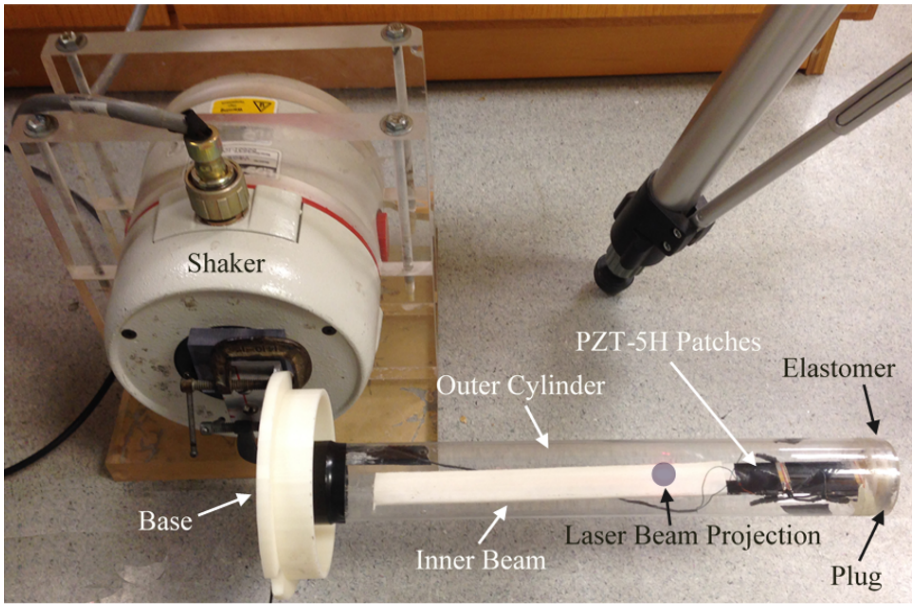

Figure 3.1.3: Ling/LDS V408 V-408 Low Force Vibration Tester/Shaker and labled experimental setup.

wind tunnel were measured using a flow meter. In Matlab, a linear regression of the data points for all the wind velocities and fan frequencies correlated the wind velocity (m/s) to fan frequency (Hz) as shown in Equation 3.1.1.

$$v(f) = 0.8456f - 2.9346 \tag{3.1.1}$$

The first data set included the resonance frequency of the fully assembled cylinder-beam harvester in the wind tunnel. These results were compared to the shaker results and the value obtained in the FEA. Voltage output from the piezoelectric elements was taken over a range of wind velocities from 7.7 m/s to 26.5 m/s.

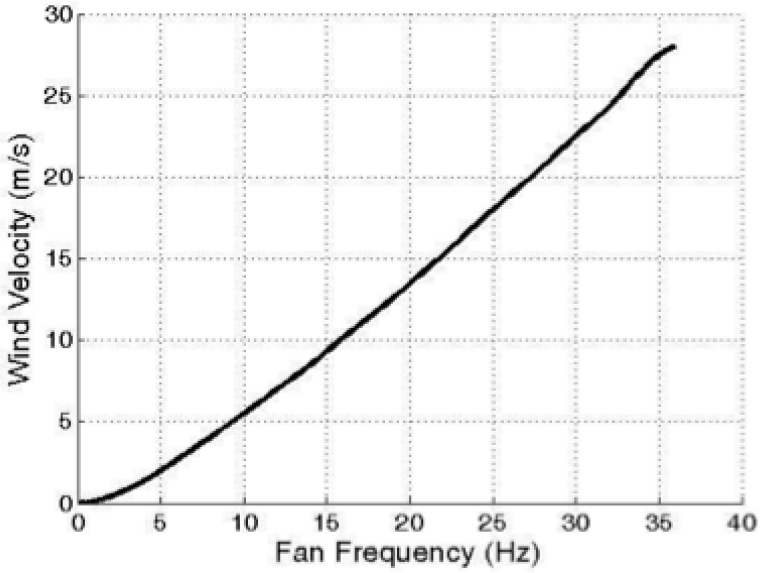

Figure 3.1.4: Wind velocity (m/s) vs. fan frequency (Hz)

3.1.5 Performance without Magnifier

To obtain a baseline with which the theoretical results and the experimental dynamic magnifier could be compared, a larger base plug was fabricated to fit in the free end of the cantilevered cylinder without an elastomer. For testing, this prototype was placed in the wind tunnel. Measuring voltage output on the signal analyzer across a range of wind velocities resulted in a correlation between wind speed and piezoelectric voltage output. In addition, for each wind speed, the signal analyzer showed an FFT plot for the voltage, which revealed the different modes of the structure (structural frequencies) in addition to the vortex shedding frequencies. Voltage output was maximized by determining where the vortex shedding frequency matched the structural frequency. The voltage in the system was measured across the internal impedance of the scope.

3.1.6 Performance with Magnifier

Dynamic magnification testing followed an identical procedure to that of the non-magnified testing, except that the harvesting structure included the plug-beam subassembly fitted inside an elastomer ring. The voltage outputs of both systems were later compared to one another.

3.2 Harvesting Results and Discussion

In this section, the results from the finite element analysis are presented and discussed. The experimental results from the shaker and vibrometer testing are compared with the theoretical simulations. Finally, the wind tunnel results are presented, and a discussion of the performance of the harvester evaluates the feasibility and success of the design.

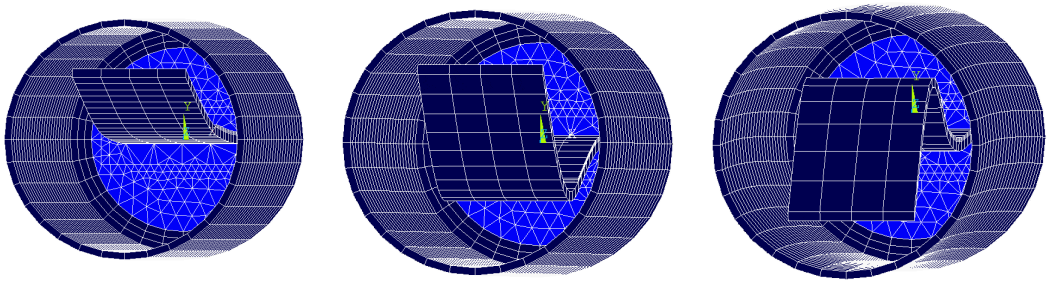

(a) (b) (c)

Figure 3.2.1: This picture shows the first(a), second(b), and third(c) bending modes of the beam with baseline configuration from ANSYS

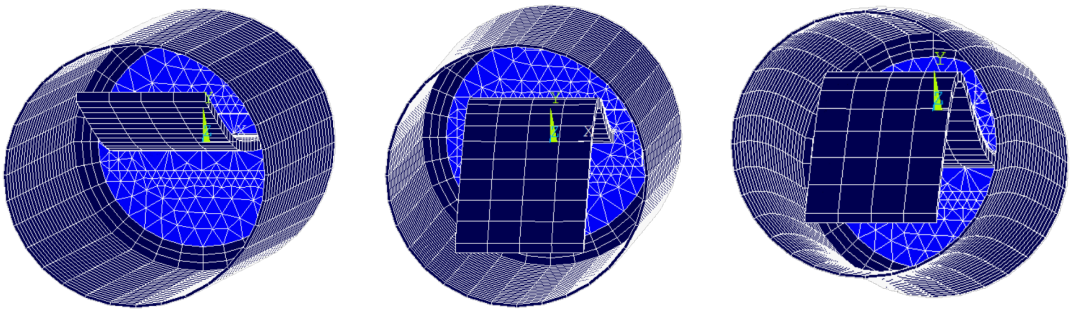

(a) (b) (c)

Figure 3.2.2: This picture shows the first(a), second(b), and third(c) bending modes of the beam with dynamic magnification from ANSYS

3.2.1 Finite Element Analysis

In order to validate the vibrometer and wind tunnel results, a computer model of the harvester was constructed to determine the theoretical performance of the prototype. Both baseline and dynamic magnification configurations were simulated to ensure that results from both experiments could be supported theoretically. The code used in the ANSYS simulation is included in the Appendix and the results are described below. The model was excited at a continuous range of frequencies from 1 Hz to 200 Hz. The first four modes of the cylinder and beam were determined and the most important modes shapes are shown below. The first, second and third modes of the beam are the most important as they exert the maximum strain on the piezoelectric material. The first three modes of the beam in the baseline configuration are shown in Figure 3.2.1a, 3.2.1b, and 3.2.1c. Their frequencies are 9 Hz (a), 34 Hz (b), and 76 Hz (c). The first three modes of the beam with dynamic magnification are shown in Figure 3.2.2a, 3.2.2b, and 3.2.2c. Their frequencies

are 9 Hz (a), 34 Hz (b), and 80 Hz (c). The remainder of the peaks found in the ANSYS testing are included in the Appendix.

3.2.2 Shaker Testing

After theoretical tests were completed to determine the bending modes of the prototype, the constructed harvester was secured to a shaker for testing as described in the methodology section of this paper. An initial sine sweep generated by the spectrum analyzer, and used to drive the shaker, allowed the determination of the frequencies where the piezoelectric material experienced maximum voltage output. These excitation frequencies were then evaluated using a scanning laser vibrometer to determine which modes the peaks represented. The sine sweeps for the beam and cylinder in both the baseline and dynamic magnification configurations are shown in Figure 3.2.3 and Figure 3.2.4. Since the cylinder did not have any piezoelectric material to measure the strain, an accelerometer was utilized in the sine sweep to determine mode locations for the cylinder. In addition, each of these figures contains a table that presents the theoretical bending modes determined by the FEA. The sine sweep for the beam showed peaks at 9, 18, 31, 57, 69, 79, 85 and 148 Hz. While the sine sweep peaks at 9, 31 and 85 showed promising correlation to the results obtained in the finite element analysis, a definitive connection could not be proved until the laser vibrometer measured the shape of the beam displacement at each of these frequencies. The sine sweep for the cylinder showed peaks at 18, 31, 59, 70, 79 and 90 Hz. Although the modes did not align exactly due to unknown properties related to the coupling of the beam-cylinder system, the third mode of the beam and the first mode of

the cylinder were close to each other. This finding was important for the eventual tuning of the system in wind tunnel testing.

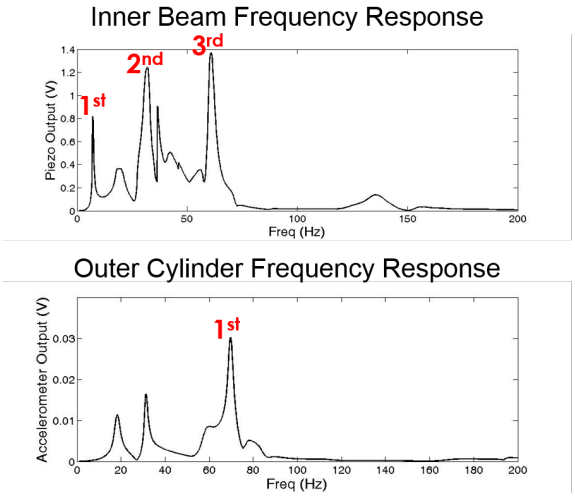

FEM Results

Frequency (*Hz*)	Description
9.141	First Bending of Beam
34.265	Second Bending of Beam
55.505	First Bending of Shell
58.839	Second Bending of Shell
91.476	Third Bending of Beam
91.547	Rocking of Beam/Shell
170.94	First Torsion of Beam
190.90	Fourth Bending of Beam

Figure 3.2.3: Sine sweep of the beam in the baseline system

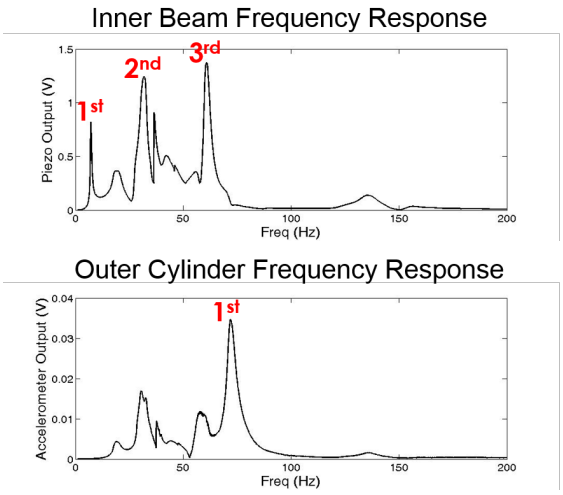

FEM Results

Frequency (*Hz*)	Description
9.136	First Bending of Beam
34.842	Second Bending of Beam
76.606	First Bending of Shell
76.788	Second Bending of Shell
93.889	Third Bending of Beam
95.224	Rocking of Beam/Shell
171.180	First Torsion of Beam
189.550	Fourth Bending of Beam

Figure 3.2.4: Sine sweep of the cylinder in the baseline system

3.2.3 Vibrometer Testing

To demonstrate that the peaks determined in the shaker testing were the same peaks shown in the finite element analysis, a scanning laser vibrometer was used to measure precise beam displacement during excitation. The shaker was used to excite the beam at each peak determined in the previous testing. Although the prototype was excited at each peak determined by the sine sweep, only the major bending modes of the beam are shown below. The remaining vibrometer data is included in the Appendix. The first set of vibrometer data was taken with the baseline configuration. In figures below, the color map shows the displacement of the beam at 7, 32 and, 60 Hz.

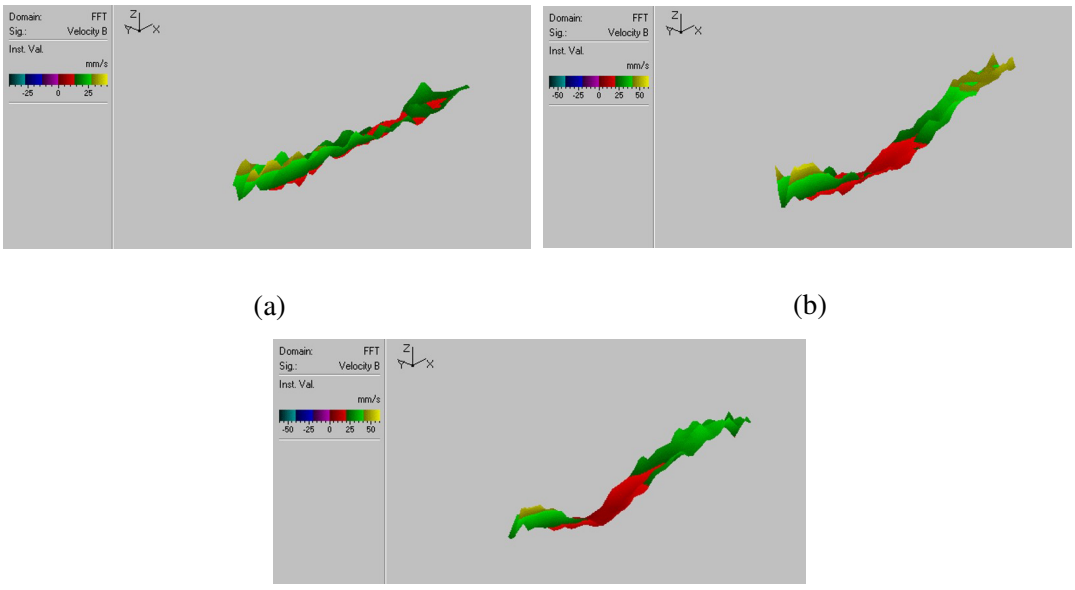

(a) (b)

(c)

Figure 3.2.5: Displacement color maps of the first(a), second(b), and third(c) bending modes of the beam with baseline configuration

In Figure 3.2.6a the two dimensional color map verified the location of the first

bending mode of the beam at 9 Hz for the dynamic magnification configuration. In Figure 3.2.6b, the prototype was given an input excitation of 31 Hz and the vibrometer results clearly show the presence of the second bending mode of the beam.The rest of the frequencies present in the sine sweep showed ambiguous mode shapes, which are torsional modes or superpositions of modes. The most accurate measurements are taken when the displacements occur along the axis parallel to the laser. Torsion is more difficult to measure and results in images that are more difficult to classify. Figure 3.2.6c shows the closest response to a third mode found in the list of frequencies. The bending of the beam closely resembles a superposition of the second and third modes at 69 Hz which makes it difficult to determine the location of the third bending mode with the vibrometer.

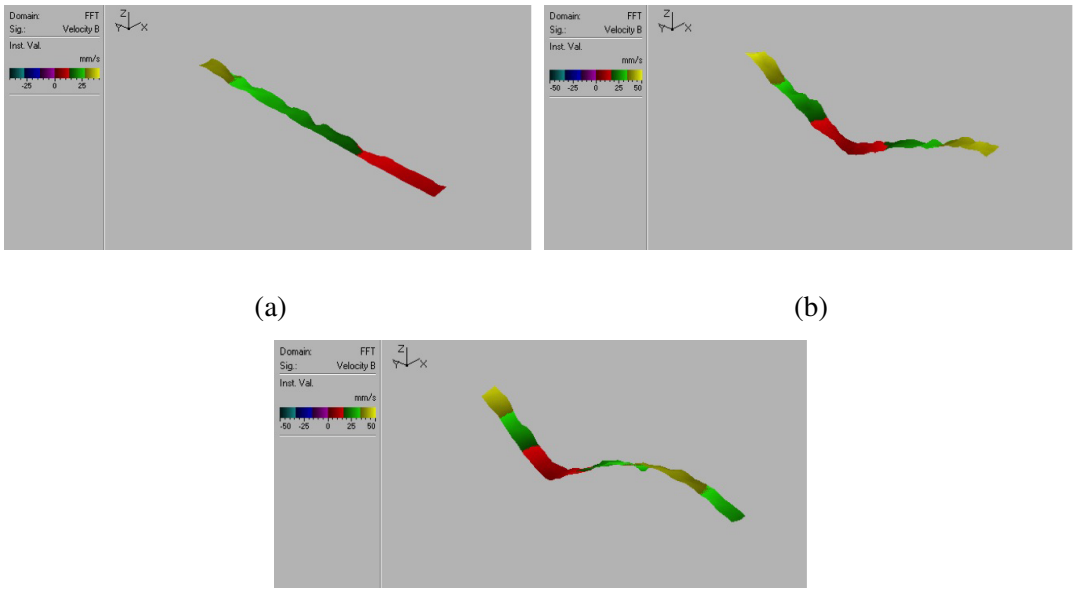

(a) (b)

(c)

Figure 3.2.6: Displacement color maps of the first(a), second(b), and third(c) bending modes of the beam with dynamic magnification

3.2.4 Wind Tunnel Testing

The final stage of testing involved placing the harvester in the wind tunnel in order to determine the performance of the harvester in a real world application. Three different harvester configurations were tested: baseline, elastomer A, and elastomer B, where elastomer A and elastomer B had different stiffnesses. For wind tunnel testing, it was hypothesized that dynamic magnification would cause the harvester to generate more voltage than the baseline harvester system. Baseline wind tunnel testing results showed a peak voltage output of 438 mV at a flow velocity of 12.9 m/s as shown in Figure 3.2.7. In the baseline configuration, the Strouhal (vortex shedding) frequency was approximately 100 Hz at a flow velocity of 20.6 m/s and the structural frequency was approximately 55 Hz, but at the optimal flow speed of about 13 m/s, the Strouhal frequency aligned with this structural frequency and the system experienced the highest level of vibrations, and thereby the highest voltage output. The first bending mode of the cylinder, which is excited at the Strouhal frequency, matches the third bending mode of the inner beam.

Using elastomer A, the peak voltage output from the harvester was 903 mV, while using elastomer B, the peak voltage was 939 mV as shown in Figure 3.2.8a and Figure 3.2.8b. Both of these peaks were measured at a flow velocity of 19.1 m/s. As shown in Figure 3.2.9, the voltage dropped at flow speeds greater than 19.1 m/s. Voltage outputs at a greater range of flow velocities were also measured, and the plots of these results can be found in the Appendix.

As projected, dynamic magnification resulted in more than double the voltage output of the non-magnified harvester system as in the case of elastomer B, which experi-

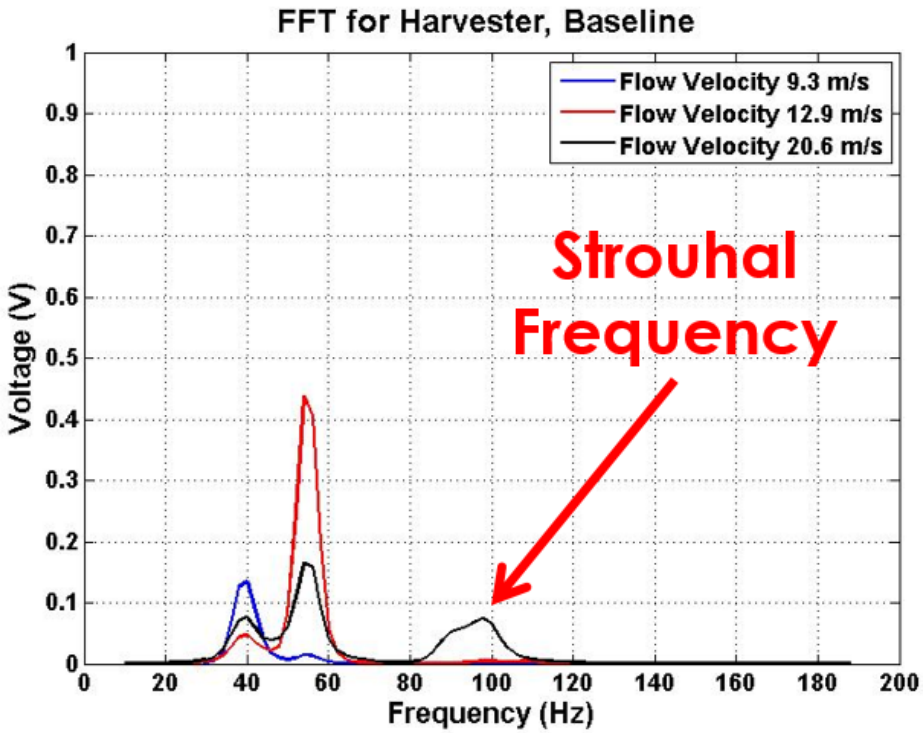

Figure 3.2.7: Peak voltage output for the baseline harvester system without dynamic magnification

enced a 509 mV increase. In the plots from all three setups, the harvester reached its peak voltage output only at the optimal flow velocity and then subsequently decreased. This was due to the phenomenon of the coinciding structural and Strouhal frequencies at the optimal flow velocity that resulted in a voltage peak. This increased voltage output was desired for the conditioning subgroup to harness and transform into storable electricity.

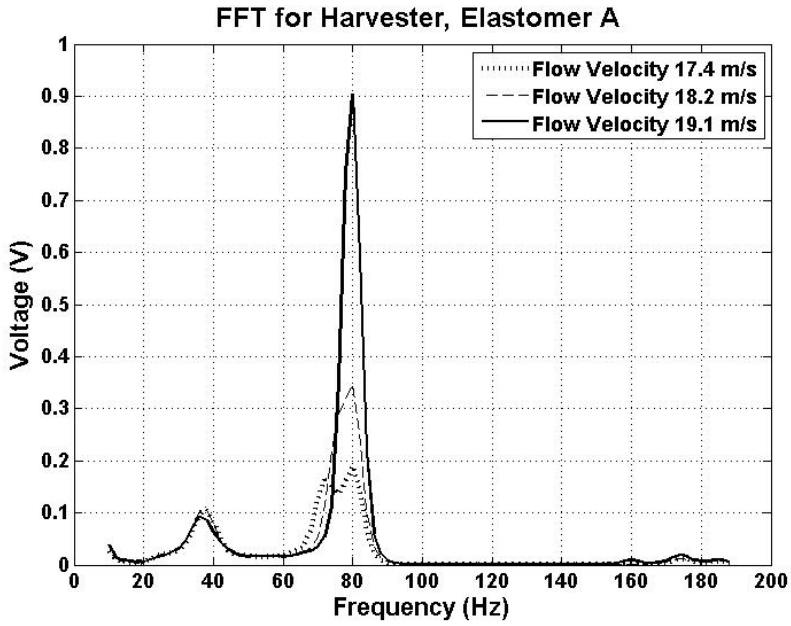

(a)

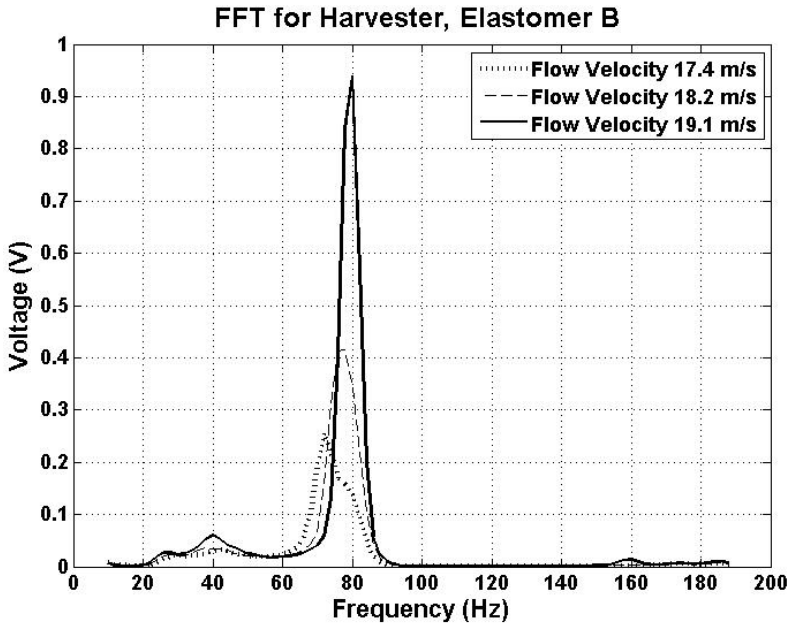

(b)

Figure 3.2.8: Peak voltage output for the harvester systems with elastomers A(a) and B(b)

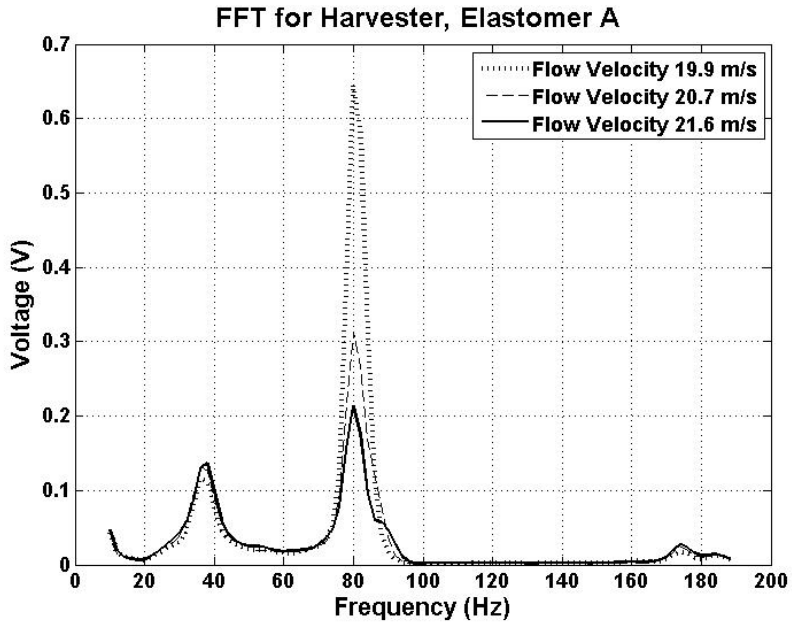

(a)

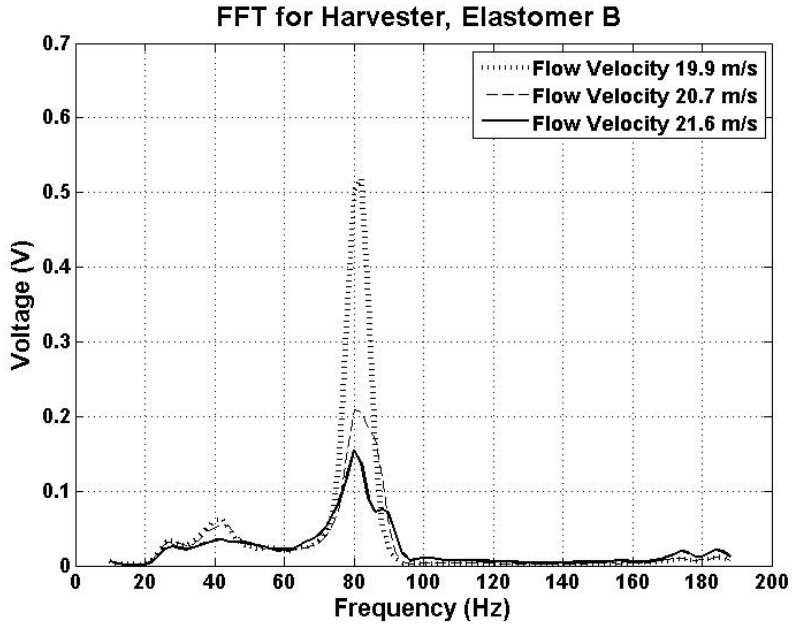

(b)

Figure 3.2.9: Peak voltage output for the harvester systems with elastomers A(a) and B(b) after optimal flow velocity

3.2.5 Harvesting Discussion

Although the results show promise for future piezoelectric integration into energy harvesters, more research must be completed to determine the feasibility of this design. The experimental prototype utilized in the data collection was not as robust as expected, leading to errors and inconsistencies in data collection. For example, securing the prototype in the wind tunnel required a very precise procedure. Changes in the position of the prototype, as little as a millimeter, drastically changed the results. Although the results were precise, a more robust prototype would lead to a higher voltage output. Throughout testing the prototype was converted from the baseline configuration to the dynamic magnification configuration multiple times for different sets of data. As the plug and beam were separated, fatigue on the piezoelectric material and the beam may have led to non-optimal testing conditions in the later data sets.

The scale of the energy harvester was limited by the dimensions of the wind tunnel test environment. Specific parameters such as the length of the outer cylinder, the length of the beam, and the size of the base were governed by the inner dimensions of the test environment. Larger scale designs could be tested in a wind tunnel with a larger test environment. These variations would utilize larger piezoelectric samples to harness vibrations and produce more voltage.

In retrospect, approaching the project from a vibrational perspective and forgoing wind tunnel testing to concentrate on shaker testing would have allowed for highly controlled experimental conditions. However, the phenomenon of vortex shedding would be completely absent in the proposed experimental setup.

One significant accomplishment described in the results is the similarity between shaker data and the ANSYS model for the dynamic magnification configuration. With an accurate model to describe prototype behavior over a wide range of frequencies, the harvester can be tuned and modified to maximize output without having to construct multiple prototypes for testing. Another valuable conclusion is that a dynamically magnified system generates considerably higher voltages than a non-magnified system. The frequency responses for both systems showed similar trends within their optimal flow velocity ranges, but the voltage output was over two times higher with dynamic magnification. This significant improvement in output demonstrates the feasibility of dynamic magnification in wind-induced energy harvesters.

3.3 Summary

The harvesting chapter describes the construction of the energy harvester and data obtained from FEA, vibrometer/shaker testing, and wind tunnel testing. One of the primary goals was to determine the viability of dynamic magnification by assessing the harvester's performance in the presence of a flow. As such, the harvester was designed to be interchangeable between a dynamically magnified configuration and a baseline configuration. These two designs were tested extensively with FEA in order to determine the theoretical natural modes of vibration for the structure. Next, the harvester was analyzed physically for its modes of vibration using the vibrometer/shaker setup, which allowed for verification of the FEA modeling. The matching between the FEA and the verification testing indicated a high-fidelity model for the harvester structure. Based on the results

from wind tunnel testing, it was determined that the first bending mode of the cylinder, which is excited at the Strouhal (vortex shedding) frequency, matches the third bending mode of the inner beam at the optimal flow velocity. Also, the results showed that dynamic magnification generated over double the voltage output than the baseline configuration. One significant limitation of the design was the scale, in that a larger wind tunnel test section would have allowed for a better design with more piezoelectric materials.

4 Conditioning

The purpose of the conditioning system is to efficiently convert the AC voltage from the piezoelectric harvester to a DC voltage which can be stored in the storage subsystem. This chapter details the methodology and results for the characterization of optimal impedance conditions for the SEH and SSHI-P rectifier circuits. A comparision is made between peak power outputs and corresponding impedance values for the SEH and SSHI-P circuits. In addition, performance of the two rectifier circuits is analyzed with varying capacitive loads.

4.1 Conditioning Methodology

In this section, the methodology for the design of the circuit simulation models, the construction of the experimental setup, and the data collection procedure are described.

4.1.1 Construction of the Rectifier Circuit Models

In order to verify the results obtained from the experimental setup, it was necessary to create simulated models of the rectification circuits that would be tested. Of the two circuits constructed, the SEH required the least number of components. Figure 4.1.1 contains the schematic as used in the simulation.

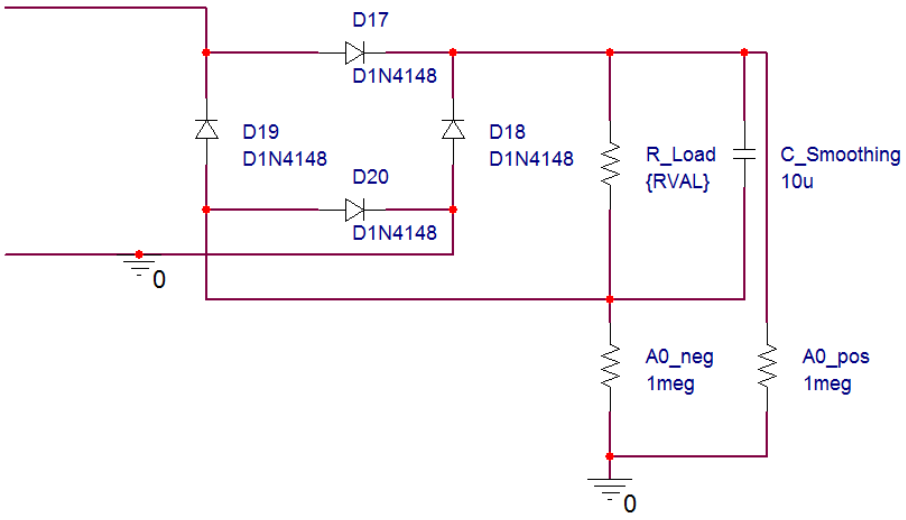

Figure 4.1.1: pSpice schematic for the SEH circuit

All model numbers and corresponding values can be found in Table 4.1. While the value of the capacitor 'C_Smoothing' appears to be fixed in the schematic above, it was varied between runs. Initially, a capacitor value of 10 μF was used for two reasons: it provided sufficient control over voltage ripples and allowed for a suitable charge time. The capacitance was later varied to ensure that the results remained consistent across a range of capacitor values. The resistive load, 'R_Load' in the schematic, was the independent variable during the simulated trial runs. The output voltage, and by extension the power, were the dependent variables.

Model Name	Component	Value
D1N4148	Leaded Glass Diode	N/A
R/ANALOG	Resistor	1 kΩ – 100 MΩ
C/ANALOG	Capacitor	10, 47, 100, 220 μF

Table 4.1: Model numbers, descriptions and values for the components of the SEH circuit

The SSHI-P circuit required far more components and tuning. The SSHI-P resembles the SEH; however, it uses a peak-based switch. The switch needs to toggle for every peak of the input signal. The design of such a switch is non-trivial and is frequency dependent. The design in the schematic in Figure 4.1.2 was inspired by previous research[41]. A list of the model numbers and corresponding values can be found in Table 4.2.

Model Name	Component	Value
D1N4148	Leaded Glass Diode	N/A
R/ANALOG	Resistor	1 kΩ – 40 MΩ
C/ANALOG	Capacitor	100 pF – 10 μF
L/ANALOG	Inductor	100 mH
LT6003	Linear Technology Op-Amp	N/A
LMC7215/NS	Texas Instruments Comparator	N/A
IRF7307	Dual N-P Channel MOSFET	N/A
VDC/SOURCE	Voltage Source	$\pm$3 V

Table 4.2: Model numbers, descriptions and values for the components of the SSHI-P circuit

4.1.2 Tuning of the Rectifier Circuits

The fixed component values for the SSHI-P circuit were selected based on the desired performance of the switch at the frequency of operation. The frequency of operation was determined by the harvesting system and was given as approximately 78 Hz. A list of the component values is given in Table 4.3.

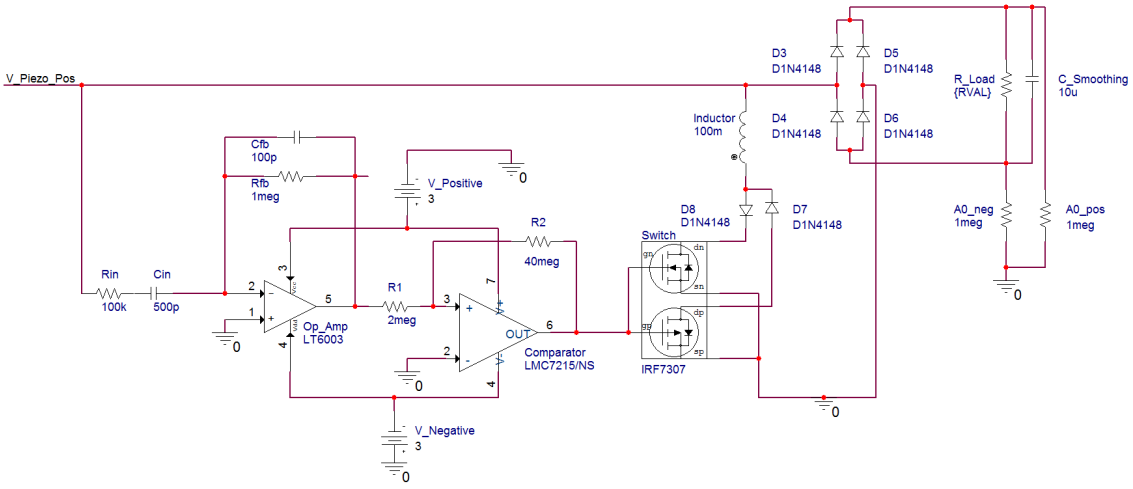

Figure 4.1.2: pSpice schematic for the SSHI-P circuit

Component	Value
R_{in}	100 kΩ
C_{in}	500 pF
R_{fb}	1 MΩ
C_{fb}	100 pF
R_1	2 mΩ
R_2	40 mΩ
V_+,V_-	±3 V

Table 4.3: Fixed component values for the SSHI-P circuit

The component labeled as 'Op_Amp' in Figure 4.1.2 takes the input signal and outputs the signal's derivative. For this circuit to function, the component values must be selected so that the phase-shift of the circuit is $90°$ and the gain is sufficient for boosting the output to a level that would trigger the square-pulse generator. The transfer function

and gain governing the differentiator is given by these equations[41]:

$$\frac{V_0}{V_{in}} = \frac{-1}{(R_{in} + \frac{1}{sC_{in}})(\frac{1}{R_{fb}} + sC_{in})} \tag{4.1.1}$$

Figure 4.1.3 shows the bode plot for both gain and phase shift of the differentiator. For the target frequency of 78 Hz, the phase-shift is 87.54° and the gain is -28.19 dBm.

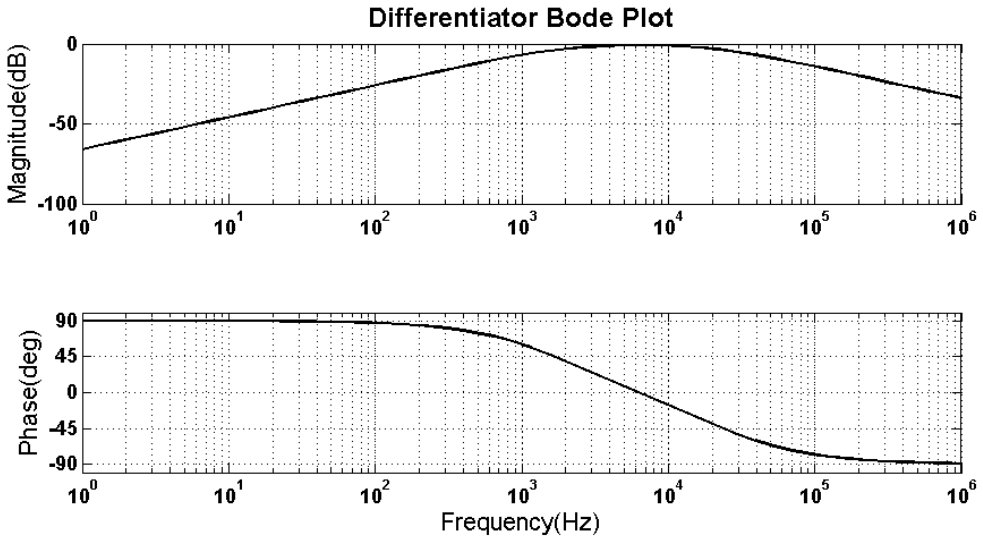

Figure 4.1.3: Bode plot for gain and phase shift of differentiator

The component labeled 'Comparator' in Figure 4.1.2 acts as a square-pulse generator. It converts all positive values from the output of the differentiator to a rail value of 3 V and all negative values to -3 V. This creates a square-wave pulse which will drive the NMOS and PMOS package, switching the inductor on and off. The component values for the square-pulse generator determine the threshold voltages, V_I and V_h that toggle the output. This relationship is given by these equations[41]:

$$V_I = V_- \frac{R_1}{R_1 + R_2} \tag{4.1.2}$$

$$V_h = V_+ \frac{R_1}{R_1 + R_2} \tag{4.1.3}$$

Based on the values in Table 4.2, the threshold voltage to trigger the comparator is $\pm$286 mV. The final fixed value component is the inductor. The value of the inductor governs the inversion time and factor for the voltage on the piezoelectric element. A 100 mH inductor was selected based on previous research[41]. This value of inductance allows for a sufficient inversion time based on the low frequency of operation.

4.1.3 Running pSpice Simulations

Evaluation of the circuits was based on relative peak power outputs and the corresponding real-valued load resistance. In order to determine the output power, the resistive load was varied while measuring voltage across the load. After achieving steady-state, the voltage across the load was then averaged over a duration of 2 seconds. In the case of the active SSHI-P circuit, the calculation of power consumption by the circuit itself was also necessary. This measurement was taken by recording the current drawn from the power supplies present in the system for the duration of the averaging. Power consumed by the SEH circuit is zero since there are no active elements.

In pSpice, component values can be parametrically swept by declaring them as global variables. The value of 'R_Load' in Figure 4.1.1and Figure 4.1.2 is a global variable named 'RVAL'. For each circuit, the value of RVAL was swept over a pre-set range, from 1 kΩ to 60 kΩ while the voltage across the resistive load was measured. A sample output from this process can be seen in the Figure 4.1.4.

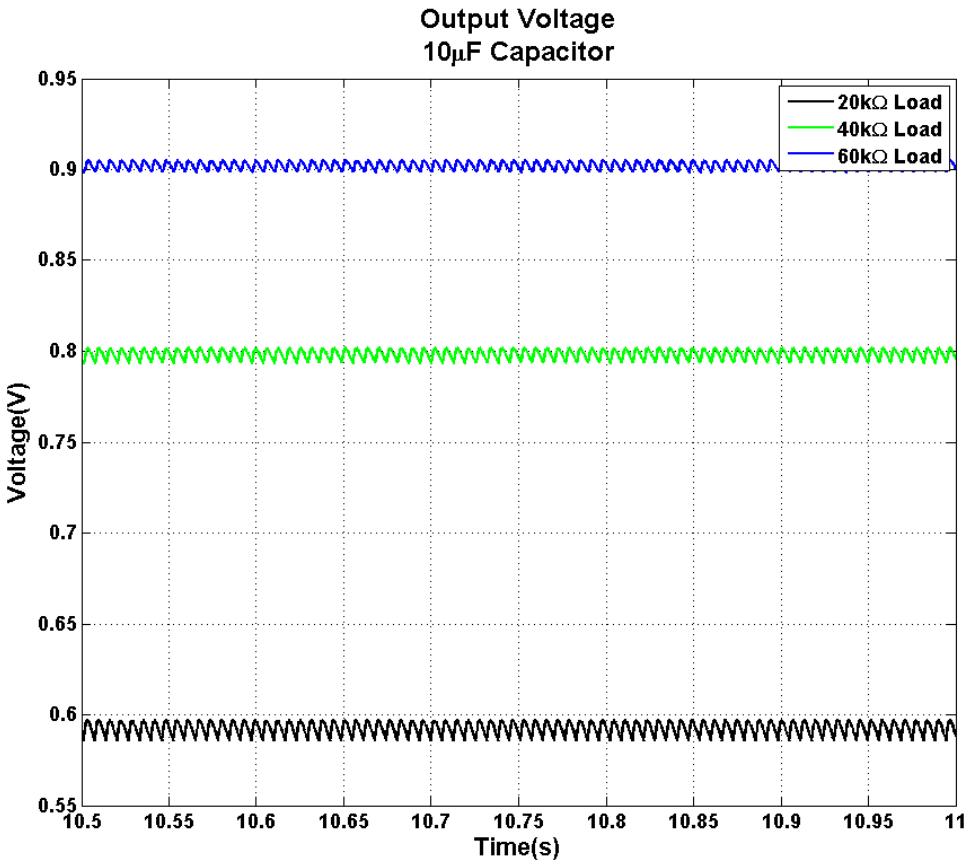

Figure 4.1.4: Voltage across the resistive load over time for a sweep of different RVAL values

4.1.4 Evaluating the Simulation Results

The data from the pSpice environment was next exported to Matlab. The voltages across the time period were then time-averaged. The average power was finally calculated based on the relationship:

$$P_{avg} = \frac{V_{avg}^2}{R} \tag{4.1.4}$$

While there is a capacitor in parallel with the resistor, the current that passes through the capacitor can be approximated to zero after the system reaches steady-state. For the

SSHI-P circuit the power consumption was taken as:

$$P_{consumed} = |V_{source}|I_{avg} \tag{4.1.5}$$

Finally, the total net power output was given as:

$$P_{net} = (P_{avg}) - (P_{consumed}) \tag{4.1.6}$$

This process yielded the net power output from each circuit as a function of the resistive load. The optimal load value is defined as the resistive load value for which the net power is maximized for the given circuit.

4.1.5 Construction of the Physical Rectifier Circuits

The components used in constructing the circuit were the same as the simulated components in the pSpice models. Simulation models and experimental components were matched to improve the likelihood of the experimental data agreeing with the simulated data. The only variation to the design involved the load resistance. A resistor box produced by Elenco, shown in Figure 4.1.5, was used in order to quickly sweep the load resistance. This box can generate a resistance from 0 Ω to 11 MΩ in 1 Ω increments.

When laying out the components, a breadboard was used to connect the resistor box and replace damaged or different valued components. A diagram of the constructed SEH circuit is shown in Figure 4.1.6.

4.1.6 Experimental Setup

When preparing to collect data, it became apparent that there would not be enough time to perform a full experimental test of both the SEH and SSHI-P circuits. Experi-

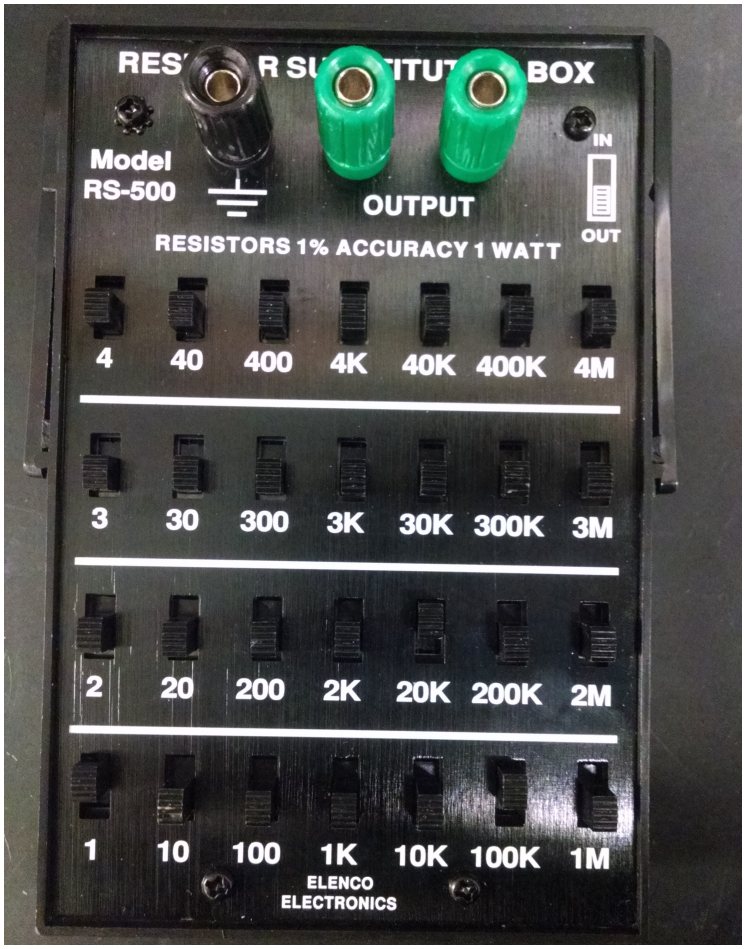

Figure 4.1.5: Variable resistor box

mental testing of the SEH circuit was prioritized, but simulated results from the SSHI-P circuit were still included for comparison.

The rectifier circuits required testing using the output of a piezoelectric material, but is difficult to model the mechanical and electrical properties of a piezoelectric element using hardware components. An ideal case would be to perform testing with the output of the harvesting device, when the device is placed in a wind tunnel. However, in order to avoid a strict reliance on the harvesting data and to obtain consistent results, the circuits were tested using a piezoelectric stripe actuator attached to a beam being driven by a

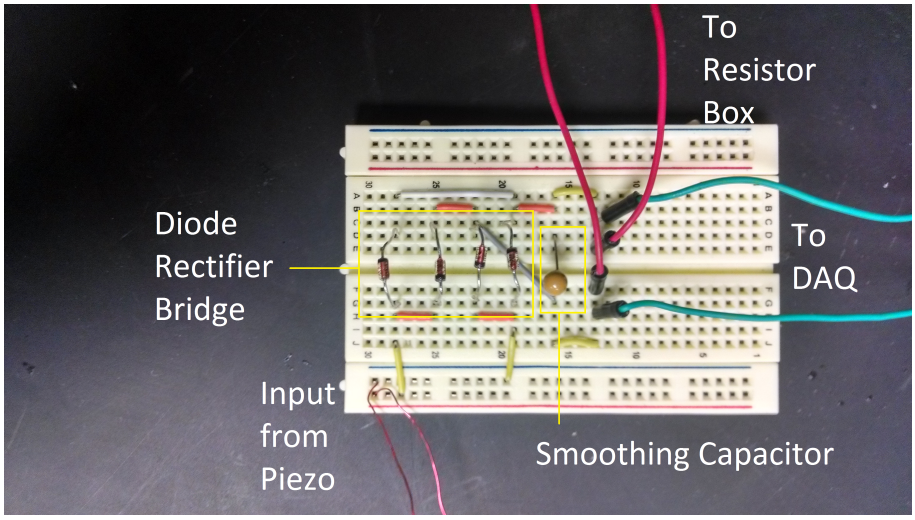

Figure 4.1.6: SEH circuit setup

shaker. By controlling the voltage gain and frequency of the shaker, AC voltage signals were generated from the piezoelectric element at targeted frequencies and amplitudes. Figure 4.1.7 contains an image of the piezoelectric beam shaker setup.

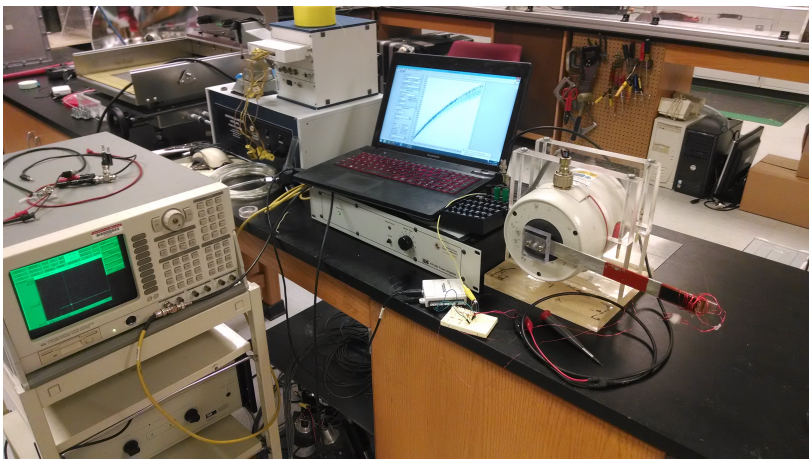

Figure 4.1.7: Piezoelectric shaker setup used to test the SEH circuit

The output from the piezoelectric stripe actuator acted as the input to the SEH circuit. The piezoelectric element used for the experiments is a stripe actuator, model no. 40-2010, produced by APC International. Table 4.4 gives the basic properties of the

piezoelectric stripe.

Length	60 mm
Width	20 mm
Thickness	0.7 mm
Total Deflection	$>$ 2.6 mm
Blocking Force	$>$ 0.5 N
Resonance	60 Hz
Capacitance	190 nF

Table 4.4: Fixed component values for the SSHI-P circuit

The output of the circuit was measured across the load using the National Instruments data acquisition USB-6009 device (DAQ). A differential measurement across the load was measured, transmitted to a laptop, and detected by LabVIEW software. This software allowed the measurement and time-averaging of voltages over a period of time before recording them to a text file for data analysis. The input leads to the DAQ device were configured as recommended in the manual using the differential for floating signal sources method. A schematic for this method is shown in Figure 4.1.8. High impedance resistors (1 MΩ) were used in this experiment.

4.1.7 Collecting Experimental Data

A test consisted of two stages: calibrating the shaker and measuring voltage while sweeping the load resistance. The shaker was calibrated in order to establish continuity of data across tests. Calibration began by monitoring the open circuit voltage of the piezo-

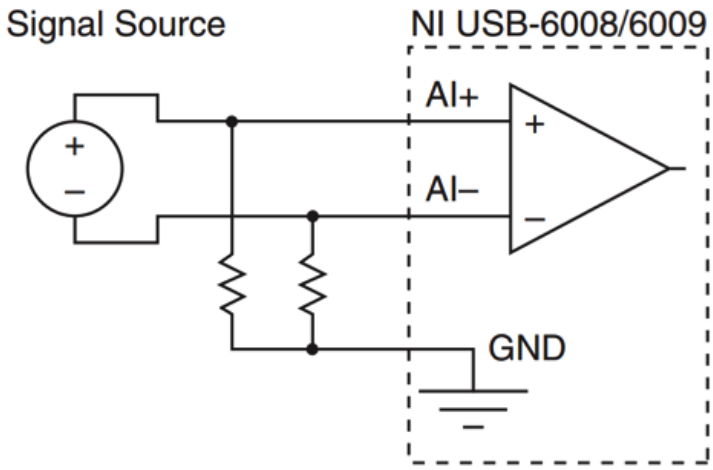

Figure 4.1.8: Circuit diagram of the method used to measure a signal with the DAQ device[36]

electric stripe. The input voltage to the shaker was of equal frequency and proportional magnitude to the motion of the shaker and therefore of equal frequency and proportional magnitude to the voltage of the piezoelectric stripe. The input voltage to the shaker was first set to the target frequency of 78 Hz. Next, the voltage gain was increased until the piezoelectric stripe produced 4 V_{pk-pk} signal. The shaker input voltage then remained fixed for the rest of the test. Doing this calibration before each test run ensured that the input to the conditioning circuit remained a fixed variable. Figure 4.1.9 shows the voltage of the piezoelectric stripe nearing the end of the calibration phase.

The output of the piezoelectric stripe was then wired as an input to the SEH circuit and the DAQ device was configured across the load in parallel with the resistor box. The DAQ device then measured a DC voltage which was a function of the load resistance. A data point was collected by setting the resistor box to the desired resistance, allowing a few seconds for the circuit to reach steady state, and then running the data collection pro-

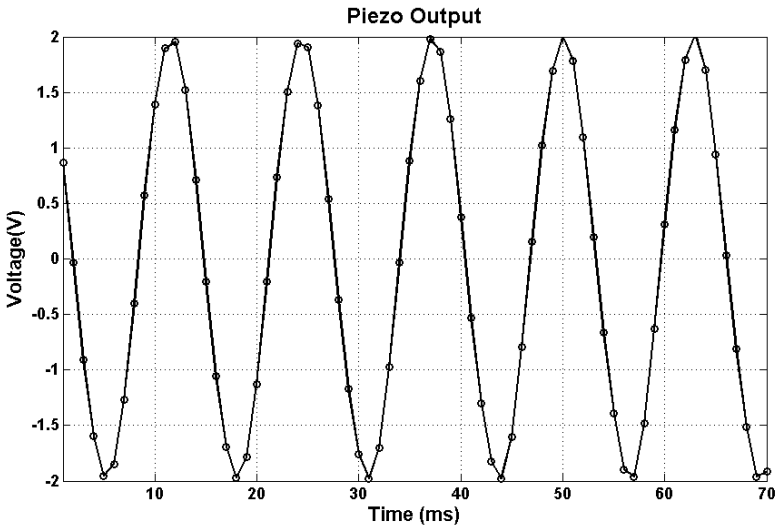

Figure 4.1.9: Input voltage from the piezoelectric stripe

gram in LabVIEW for 10 seconds. During this time, the program sampled the DC voltage and then time averaged it to produce an average voltage. This voltage was then output to a text file for later use. From here, the experiment continued by adjusting the resistor box to produce a new load resistance and then repeating this process. This continued until all desired data points were collected in the range between 1 kΩ and 100 kΩ. Typically data points were in increments of 5 kΩ, or 2 kΩ for points near the peak.

4.1.8 Derivations for Piezoelectric Analog Model

In order to accurately simulate the piezoelectric output, several impedance values were calculated based on data provided by the manufacturer. The 40-2010 stripe actuator manufactured by APC International was used, and the model shown in Figure 4.1.10 was used to simulate the piezoelectric analog. ΔP_p is the excitation force generated by the shaker and V_p is the voltage that the piezoelectric stripe generates.

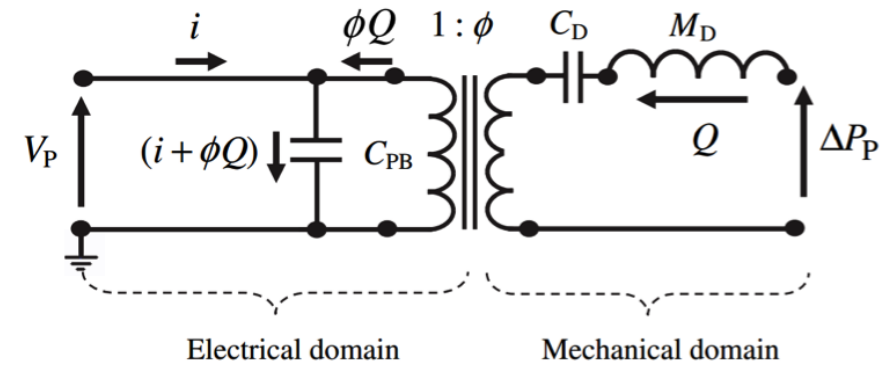

(a)

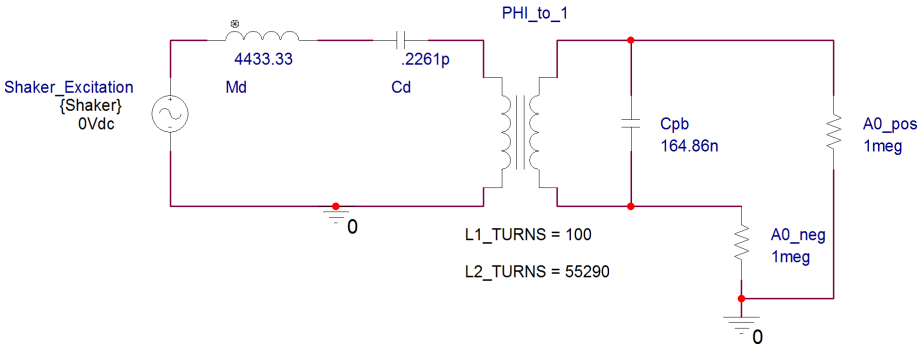

(b)

Figure 4.1.10: Schematic showing model used to simulate the piezoelectric analog(a) and its realization in pSpice(b)

The electrical domain governs the electrical properties of the piezoelectric material, while the mechanical domain corresponds to physical properties. The transformer with turns ratio ϕ corresponds to the electro-mechanical transduction coefficient. The following relationships model the system:

$$M_D = \frac{m_p}{A_R^2} = \frac{\rho l w t}{A_R^2} \tag{4.1.7}$$

$$Y_{31} = \frac{k_{31}^2 K^T \epsilon_0}{d_{31}^2} \tag{4.1.8}$$

$$C_D = \frac{Y_{31} A_R}{1} \tag{4.1.9}$$

$$\phi = \frac{-d_A}{C_D} \tag{4.1.10}$$

$$k = \frac{d_A^2}{C_p C_D} \tag{4.1.11}$$

$$C_{PB} = (1 - k^2) C_p \tag{4.1.12}$$

These relationships can be derived from the basic constitutive equations for a piezoelectric material. It was necessary to account for the mechanical domain of the harvester as well as the electrical domain. If the mechanical domain of the harvester was not modeled and coupled to the electrical domain then power drawn from the harvester would not have an effect on the excitation of the harvester. For a real piezoelectric harvester, power drawn from the harvester dampens the motion of the harvester. The coupling of the mechanical and electrical domains, modeled by the transformer in the circuit analog, determines the strength of the interaction between the domains.

A_R	1.2 mm^2	C_D	2.261×10^{-13} m^{4}s^2/kg
C_p	190 μF	C_{pB}	164.86 nF
d_{31}	-125×10^{-12} m/V	d_A	-125×10^{-12} C/N
K^{-1}	1275	k	.3638
l	60 mm	M_D	4433.33 kgm^{-4}
m_p	6.384 g	t	.7 mm
w	20 mm	Y_{31}	8.84×10^{10} N/m^2
ϵ_0	8.85×10^{-12} F/m	ρ	7.6 g/cm^3
ϕ	552.9 Pa/V		

Table 4.5: Value of parameters in piezoelectric analog model

The simulation needed to be calibrated in a similar manner to previous experiments

in order to have comparable data. This calibration was done by placing an AC voltage source at the input of the piezoelectric analog circuit to simulate ΔP_p, as can be seen in Figure 4.1.11. The source was then swept at a constant frequency in order to determine what input voltage corresponded to the appropriate 2 V open circuit voltage on the output. In addition, the DAQ was modeled with a differential measurement across two 1 MΩ resistors.

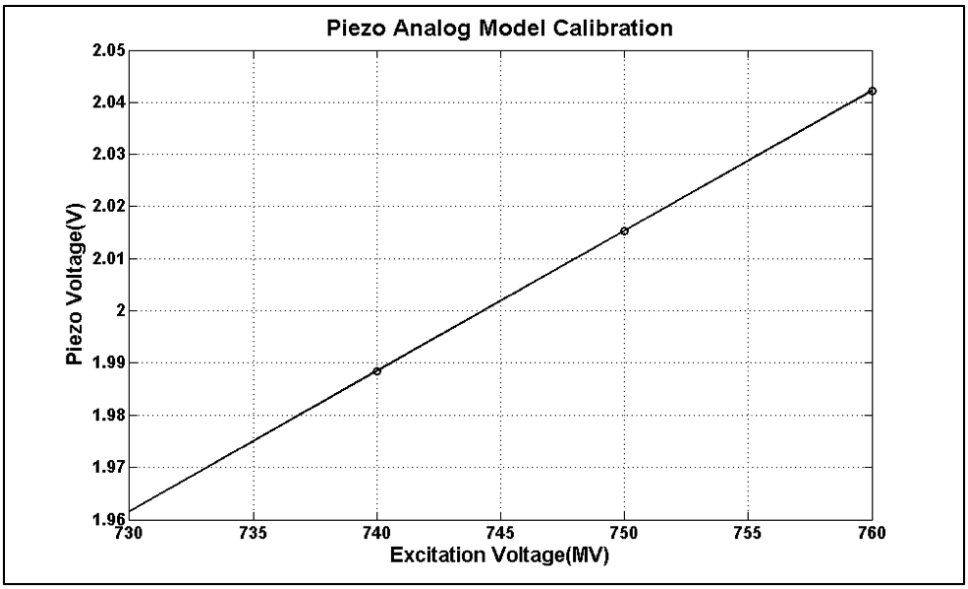

Figure 4.1.11: Excitation voltage and output amplitude of the piezoelectric analog model

4.2 Conditioning Results and Discussion

This section presents and analyzes the data obtained through the methods outlined in the previous section.

4.2.1 Data Analysis

The experimentally determined data was compared to data sets generated using the piezoelectric analog model[6]. Using this model, a reliable simulation of the piezo-bimorph output was generated by using electro-mechanical coupling factors based on the properties of the piezoelectric stripe actuator.

Validation of the data consisted of several factors. A non-linear relationship must be observed between the output voltage and load resistance. In addition, there must exist an absolute maximum power output as a function of load resistance. The maximum power output for both the experimental data and simulation data must fall within the same range of load resistances. Finally, the power output from the simulated data and the experimental data must be comparable.

Figure 4.2.1 shows the voltage across the load as a function of the load resistance. Data was collected across several smoothing capacitor values in order to ensure that the data was consistent. Both the simulated data and the experimental data exhibited a non-linear relationship, across all capacitor values. As the load resistance increased, the voltage began to level off. This relationship is key to ensuring that an absolute maximum power output exists. If the voltage is linear, the power output would exhibit a quadratic non-decreasing relationship instead.

Once the average voltage as a function of the load resistance was obtained, average power was calculated using Equation 4.2.1:

$$P = VI = \frac{V^2}{R} \tag{4.2.1}$$

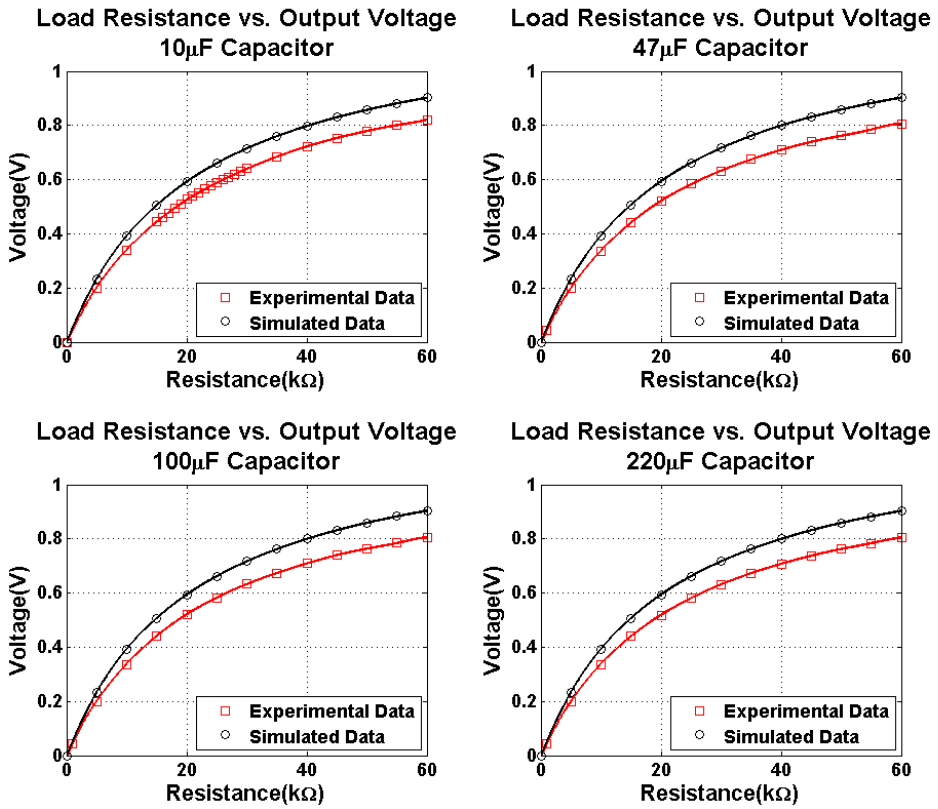

Figure 4.2.1: Output voltages of the piezoelectric analog model as a function of source resistance for various smoothing capacitor values

Figure 4.2.2 shows the relationship between output power and load resistance. For both simulated and experimental sets, an absolute maximum exists for all cases. In addition, the peak power is obtained within a narrow band of resistance values.

Table 4.6 contains the peak power value and corresponding resistance value for all sets. The peaks from each set fall within approximately 2 kΩ of one another.

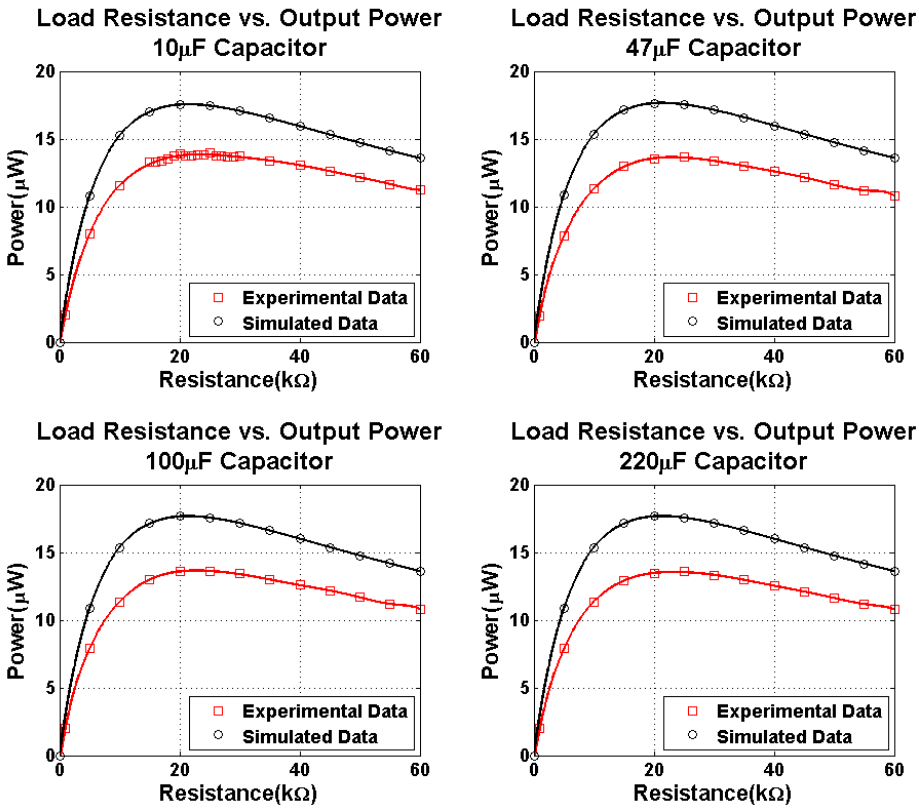

Figure 4.2.2: Output power of the piezoelectric analog model as a function of source resistance for various smoothing capacitor values

Capacitor Value	Data Set	Peak Power	Load Resistance
10 μF	Experimental	13.85 μW	23242 Ω
	Simulated	17.56 μW	21354 Ω
47 μF	Experimental	13.64 μW	22855 Ω
	Simulated	17.66 μW	21267 Ω
100 μF	Experimental	13.65 μW	22778 Ω
	Simulated	17.67 μW	21270 Ω
220 μF	Experimental	13.55 μW	23259 Ω
	Simulated	17.68 μW	21254 Ω

Table 4.6: Simulated and experimental peak power output and optimal resistance for multiple capacitors

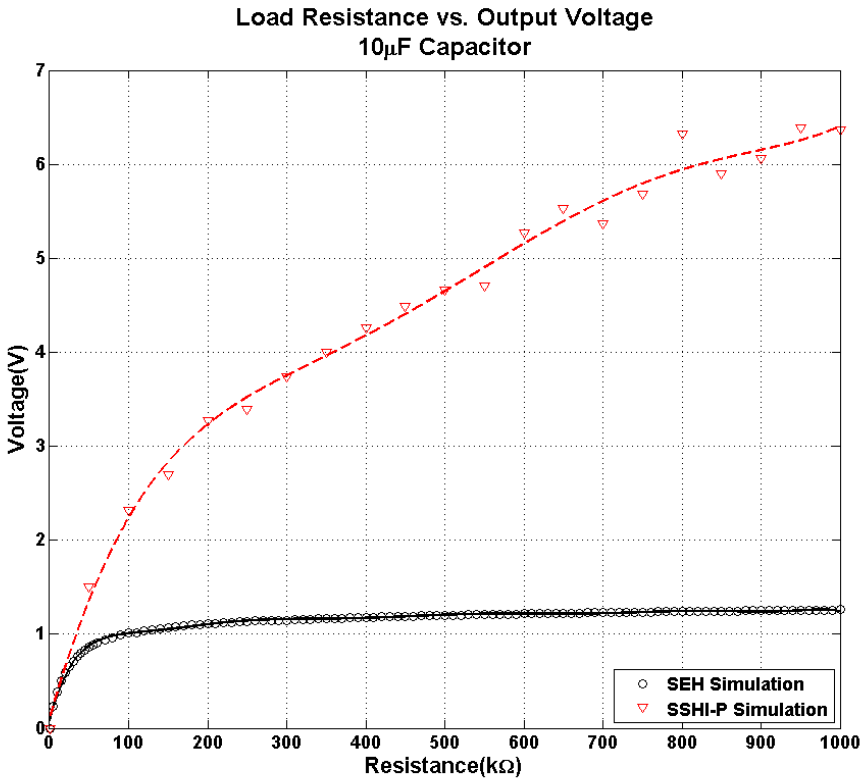

Figure 4.2.3: Simulated output voltage for SEH and SSHI-P circuits

Figure 4.2.3 shows simulated output voltage for the SEH and SSHI-P circuits over a load resistance range of 1 kΩ to1 MΩ. The simulated results show that the output voltage for the SSHI-P circuit increases as the load resistance increases. The output voltage for the SSHI-P circuit is also greater than that of the SEH circuit for all load resistances in the tested range. The results of the output power simulation show that the output power for the SSHI-P circuit is in fact significantly lower than the output power of the SEH circuit.

Figure 4.2.4 shows the simulated output power for the SEH and SSHI-P circuits over load resistances ranging from 1 kΩ to 1 MΩ. This simulation takes into account power losses from active sources. Despite a higher output voltage for the SSHI-P circuit, the output power is significantly lower than that of the SEH circuit. In fact, the net output

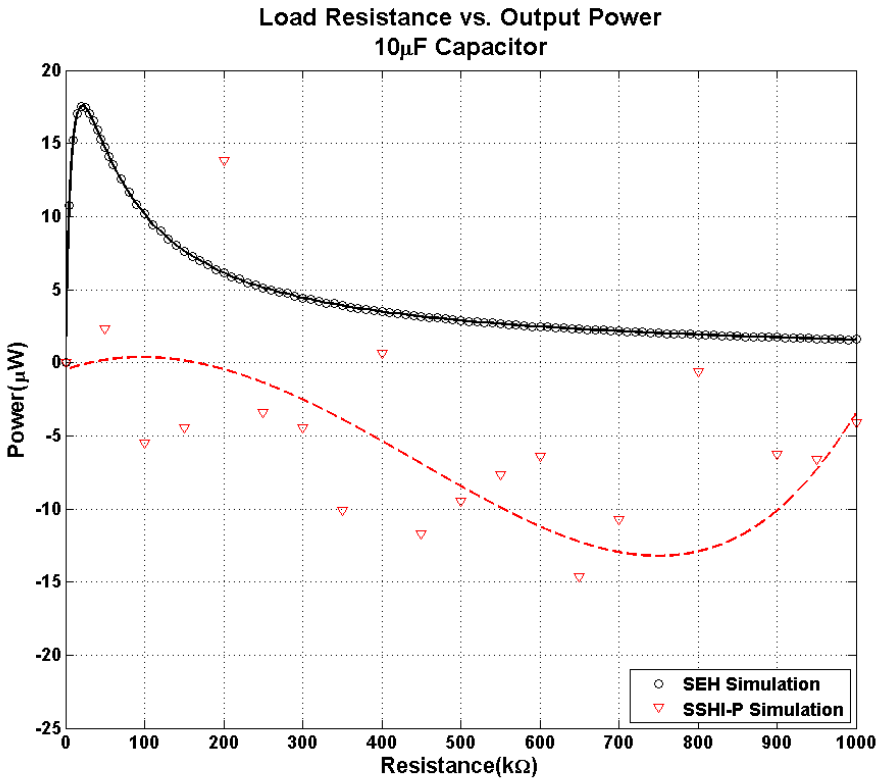

Figure 4.2.4: Simulated output power for SEH and SSHI-P circuits

power for the SSHI-P circuit is only positive for a small range of load resistances. For the majority of the load resistances tested in this simulation, the overall power generated by the SSHI-P circuit is negative as it consumes more power than it generates.

4.2.2 Conditioning Discussion

When reviewing the data, there are three main factors for consideration. The first consideration is what role the smoothing capacitance played in the power output. The results in Table 4.6 indicate that varying the smoothing capacitor at low frequencies has a very small, arguably negligible, effect on a system of this size and scale. The peak power varies only by 0.12 μW at most between capacitor values for the simulated data

sets and by 0.3 μW for the simulated data sets. Furthermore, the simulated data suggest a small peak power increase with an increase in capacitance while the experimental data saw a small loss in peak power output as capacitance values grew larger. This discrepancy is most likely due to the inability of the current pSpice model to account for real-world losses. Several of the modeled components, including the capacitors and inductors will produce losses in the physical world. For simplicities sake, the model does not factor in these losses. The losses themselves might be simulated by placing resistors of appropriate values in series with the components. However, since not all of these resistances are easily calculable, they were omitted altogether. In addition to the peak power, the corresponding load resistances too were minimally impacted. All load resistance values for the simulated set were within 100 Ω of one another. For the experimental data, the largest difference between optimal load resistances for varying capacitances was found to be less than 600 Ω, showing that the capacitor value had minimal impact on the optimal load resistance.

The second consideration for data revision was how accurate the simulation models were in predicting the peak output power and corresponding load resistance. When comparing the experimental and simulated data for a given smoothing capacitance value, it can be seen that the voltage and power levels differ. In all cases, the simulated data set predicted a higher voltage and a higher power than what was obtained through experimentation. There are a few reasons why the levels of voltage and power were different between the simulated data and the experimental data. As previously stated, the model does not factor in real-world losses for theoretically lossless components, such as capacitors and inductors. In addition to this, any inaccuracies for component values hinder the models ability to predict outputs accurately. For components such as the inductors and

capacitors, component value tolerances were small and well defined due to strict manufacturing standards. The component value of concern was the load resistance. The resistance box used as the load was not precise. When measured with a digital multi-meter, tolerances as large as 10% from their stated values. These component inaccuracies make it difficult to accurately simulate and predict voltage and power outputs. While the output levels make are not predicted with a high level of precision, the model does provide a good metric for predicting the load resistance which will produce a peak power output. For all smoothing capacitor data sets, the optimal load resistance between the experimental run and the simulated run fell within approximately 2 kΩ of each other. Since variations in the load resistance by 2 kΩ near the optimal value will result in only minor power output fluctuations, this is considered to be a success.

The third and final consideration for data revision was the overall performance of the SEH circuit when compared to the SSHI-P circuit. The results of the simulations for output voltage and output power for the SEH and SSHI-P circuits across varying load resistances differ. Power is related to voltage by the equation $I = \frac{V^2}{R}$. The output voltage for the SSHI-P circuit is higher than that of the SEH circuit, which suggests that the output power generated by the SSHI-P circuit is greater than the output power generated by the SEH circuit. However, the data generated by the output power simulation shows that the net output power generated by the SSHI-P circuit is in fact negative. This apparent contradiction is explained by the fact that the net power output factors in power consumption from active sources. The SSHI-P circuit uses an active switch which consumes more power than the circuit outputs. While this data suggests that SEH is a better option, it is important to consider scale and the overall switch design of the SSHI-P circuit. With a

higher input voltage source and a more efficient switch design, the SSHI-P circuit would produce a much higher output power. For this experiment, the input voltage source was limited by the scale of the harvesting device and the efficiency of the switch was not optimal but chosen for the ease of implementation in the pSpice environment. Diode selection also plays a critical role in determining overall performance. The SSHI-P circuit uses a standard silicon diode with a forward voltage drop of 0.7 V. The reason this diode was selected over a Schottky diode, which has a forward voltage drop of 0.3 V, was due to the lower leakage current. Schottky diodes have a larger leakage current which diminishes the efficacy of the voltage inversion that occurs during the switch time of the SSHI-P circuit. The SEH circuit is not bound by this necessity and thus would see an overall increase in power output if a Schottky diode was used in place of a standard silicone diode. Since this experiment was not about the role of diode selection, it was decided to use a standard silicone diode for both circuits for consistency.

Taken altogether, the results of simulated and experimental data yield a number of conclusions. In its current state, the model is not an accurate predictor of power output for a piezoelectric harvesting device. Despite this, the model has proved to be a useful tool and metric in predicting an optimal load resistance for a piezoelectric harvester, given the parameters of the piezoelectric element and the input force. Being able to predict an optimal load resistance is important in the proper selection of a storage device. Should a storage device?s input impedance match the optimal impedance of the harvesting and condition device, the maximum amount of power is able to be stored. In terms of the performance of the SEH and SSHI-P circuits for this application, the SEH proved to be a more efficient choice, as it generated more power for the same input. Future work and

research would revolve around being able to more accurately model real-world losses so that simulations can not only predict the optimal load resistance, but the project power output. Furthermore, the SSHI-P circuit would be revisited with the focus of designing a more efficient switch in order to make it a viable alternative to the SEH circuit.

4.3 Summary

The conditioning chapter summarizes the modeling, testing, and results related to the production of the conditioning subsystem. The goal of the conditioning system is to efficiently convert the AC output from the piezoelectric harvester to a DC input for the storage subsystem. The first step towards meeting this goal was to create pSpice models of the Piezoelectric harvester and the SEH and SSHIP-P rectifier circuits. Next, the SEH circuit was physically constructed on a breadboard for testing. The input voltage signal was generated by a PZT patch bonded to a beam, which was driven by a shaker. This set-up was used to determine the SEH circuit's optimal load resistance at the harvester's optimal oscillation frequency and to validate the pSpice models. A series of experiments were carried out by setting the piezoelectric material's output to four volts peak to peak, then sweeping through a range of load resistances to determine which value produced the greatest output power. In addition, the experiments were repeated for varying values of a smoothing capacitor to determine what effect the capacitance had on the power output and optimal load resistance. Once the data had been collected, the model's predictions were compared to the real world results. The simulations proved to be effective in estimating the optimal load resistance, but were a poor predictor for output power. By carrying

out these tests we were able to determine that the SEH circuit with a load resistance of approximately 22-23 kΩ is the most efficient design and gives an output of about 13.5 μW. Furthermore, based on the simulation outputs, the SEH circuit proved to be a more efficient design when compared to the SSHI-P. The scale of our harvester design proved to be a limiting factor in obtaining an improvement with the active rectification scheme.

5 Storage

The storage system aims to efficiently store input energy from the conditioning circuit into an energy storage device and deliver this energy to a load. Many storage systems and charging circuits are considered. The experimental process is outlined in the methodology, and the successes and challenges are presented in the results and discussion.

5.1 Storage Methodology

In this section, the selection of the battery and test circuitry is described. A method to quantify the efficiency of the different storage systems is presented. Configurations using supercapacitors are evaluated, and a final design for the hybrid system is chosen.

5.1.1 Battery Selection and Initial Testing

The storage subgroup developed several systems to compare the charging and discharging efficiencies from low power sources. The first stage of the research consisted of gathering the proper components to begin the modeling, building, and testing of the storage systems. The initial specifications were determined from estimates of the output levels from the energy harvester and conditioning circuit. The output voltage of the rectifying circuit was originally estimated to be less than 1 V with a power on the order of

microwatts, assuming a perfect impedance match. Therefore, the research goal of storage device testing was to determine the most efficient storage device that could charge with a low input voltage of less than 1 V but power a load at a higher voltage.

The initial battery chosen for storage device testing was the ML614-TZ2 lithium-ion coin battery produced by FDK America, rated at 3 V. It had a capacity of 3.4 mAh, a discharge rate of 15 ?A, and a standard charge current of 15 μA. It weighed 0.17 g. The second battery, also chosen for its high power capabilities, was the MEC202-22P THINERGY lithium-ion battery. It was rated at 4.1 V with a 3.9 V nominal output voltage. It had a capacity of 2.2 mAh, a discharge rate of 0.75 mA, and a maximum continuous discharge current of 90 mA. Its internal resistance was 22 Ω. The 4.1 V THINERGY battery weighed more than the 3 V coin battery, at 0.975 g.

In addition to lithium-ion batteries, a supercapacitor-lithium ion hybrid system was investigated as a plausible storage device design. The ESHSR-0100C0?002R7 supercapacitor designed by NessCap Cp Ltd was chosen for storage device testing. It had a capacitance of 100 F and was rated at 2.7 V with a surge voltage of 2.85 V. It had a rated current of 21.4 A, a maximum current of 58.7 A, and a maximum leakage current of 1.7 mA. It was designed for 500,000 life cycles. Under DC voltage, its maximum internal resistance was 13 mΩ. In addition, it weighed 22.5 g.

5.1.2 Charging System

A commercial-off-the-shelf (COTS) energy-harvesting charger and protector designed by Maxim Integrated was chosen to charge the lithium ion battery and used appro-

priately according to the data sheet. The MAX17710 was specially designed to manage poorly regulated sources with voltages as low as 0.75 V while preventing the battery from charging to voltages that would otherwise shorten the lifetime of the cell.

The MAX17710 charging chip used in the storage subsystem is able to charge a 4.1 V battery using input voltages that are typically 0.75 V but can be as low as 0.485 V through the use of a boost regulator. It can operate using an input power anywhere between 1 μW and 100mW. The charging voltage is limited to a maximum of 4.125 V to prevent overcharging. If the voltage of the battery drops below 2.15 V, the chip enters an undervoltage lockout mode to prevent overdischarge and possible damage to the battery. The chip draws 1 nA of current from the battery when in standby, and supplies 625 nA of charging current when input power is supplied. The physical dimensions of the chip are 3 mm by 3 mm by 0.5 mm, so a printed circuit board was designed to facilitate building the external circuitry of the system. The battery must reach a minimum voltage of 3.7 V before the PCKP (unregulated output) pin can be activated and power supplied to the load. The AE pin controls whether charge is delivered to the load, and must be pulsed with a minimum of 1.13 V in order to supply current to the load. It terminates the current supplied to the load when the AE pin is grounded.

The external components were chosen in order to operate the charger in its boost regulator mode, enabling a boost converter for harvesting sources providing approximately 1 μW. The names of the pins and the associated passive component values for this mode of operation are shown in Figure 5.1.1. When a source is present, a 47 μF capacitor is charged until the voltage on the FB pin exceeds 0.75 V. Internal circuitry then pulls the LX pin low to force current through the inductor. An internal oscillator releases

the LX pin, causing the voltage on the LX pin to rise and exceed the voltage on the CHG pin. This eventually causes a buildup of voltage on the 0.1 μF capacitor on the CHG pin. The oscillator repeats this process at 1 MHz with a 90% duty cycle. Thus an input of less than 1 V is boosted to a level suitable for charging the battery. An overcharge is detected when CHG exceeds 4.5 V, at which point the boost converter limits its output in order to return CHG to a safe level.

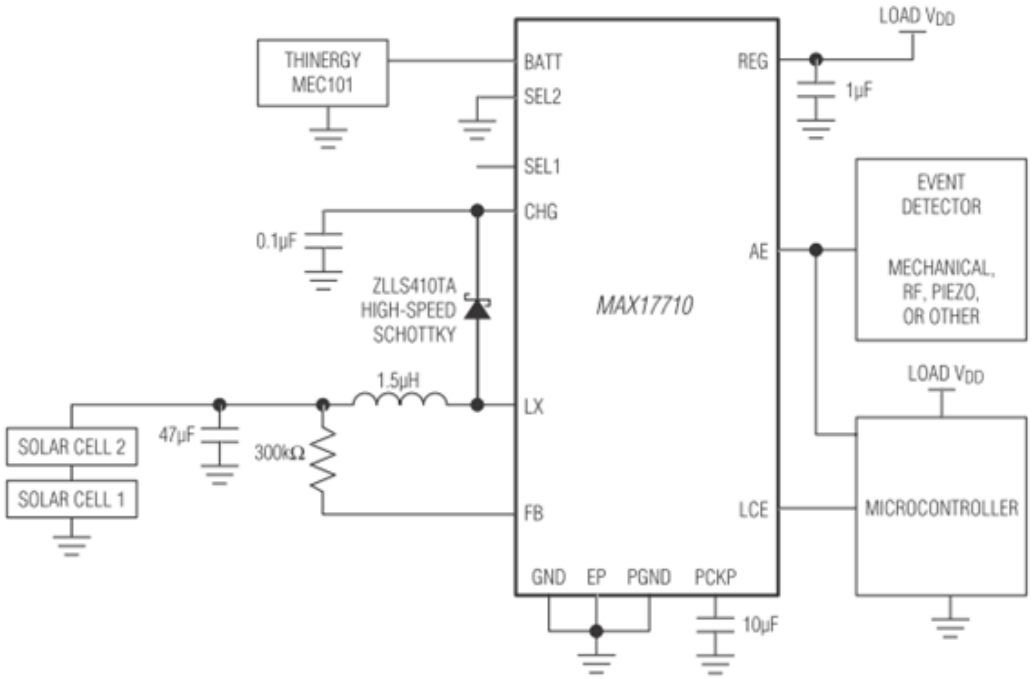

Figure 5.1.1: Boost converter configuration for the MAX17710 Integrated Circuit

The outputs are enabled through the control of the AE pin. In shutdown mode, the charger cannot provide power until a charge source is present. The system uses 1 nA of quiescent battery current. The MAX17710 determines that a charge source is present when the CHG pin exceeds 4.15 V, which causes 625 nA of current to be provided to the battery. Startup is achieved by pulsing the AE pin or holding it at a logic high value, a

minimum of 1.13 V, which enables power flow to the unregulated output pin. This startup can result in failure if the voltage on the PCKP pin is less than 2.15 V and collapses to 0 V or in success if the voltage on PCKP rises above 3.7 V. During the active period, 725 nA of current is drawn from the battery to supply the necessary power. Only after the output voltage falls below 2.15 V will an under-voltage lockout occur, causing the system to return to the original shutdown state. Otherwise, the output pin will be delivered power depending on the state of AE. After AE is grounded, the output is turned off and after AE is held at a logic high, the output is turned on.

In order to test the charging system with breadboard components and power supplies, a printed circuit board (PCB) with the footprint of the chip and breakout pins was designed using Eagle PCB Design Software. The design has holes that were spaced with a 0.1 inch pitch. Two traces of the chip layout were fabricated on 40 mm by 80 mm PCBs. The integrated circuits were placed onto the board using a heat reflow soldering station. Once the circuitry was constructed on the breadboard, ribbon cable attached to the pins in the accessible holes allowed for full integration of the chip.

5.1.3 Battery Efficiency

In order to determine the efficiency of the 4.1 V THINERGY battery in the context of the storage system a modified form of the quick test method was used[21]. Efficiency of the battery was determined by measuring the amount of energy input into the system during charging, compared to the amount of energy discharged to a load during discharg-

ing. This allowed for the calculation of efficiency by

$$\eta = \frac{E_d}{E_c} \tag{5.1.1}$$

where η is the efficiency, E_d is the discharge energy, and E_c is the charge energy.

5.1.4 Energy Measurement

The quick test method uses three voltage parameters, V_0, V_1, and V_2, in addition to three time parameters, t_1, t_2, and t_3. The battery was charged to an initial voltage of V_0. Next, the battery was charged from V_0 to V_1. The time required to charge the battery from V_0 to V_1 was recorded as t_1. The power supply was set to a constant 1 V during the charging process, and an ammeter was used to monitor the current leaving the power supply. When V_1 was reached, charging was stopped and the battery was allowed to discharge through the load attached to the unregulated output of the chip. The battery was discharged to a voltage, V_2, below that of V_0. Discharging was timed and recorded as t_2. While the battery was discharging, the ammeter was used to monitor the current leaving directly from the battery, and the oscilloscope was used to monitor the voltage drop across the battery. When the voltage of the battery dropped to V_2, discharging was stopped. At this point charging was resumed and timed until voltage V_0 was reached again. The time for the battery to charge from V_2 to V_0 was recorded as t_3. Just as with the charging process from V_0 to V_1, the current leaving the power supply was measured again with an ammeter and the power supply was set to a constant voltage. The target parameters for the quick test were as follows: V_0 = 3.8 V, V_1 = 4.1 V, and V_2 = 3.5 V.

5.1.5 Calculation of Efficiency from Measurements

The quick test results can be used to calculate both the energy used in charging, E_c, as well as the energy used in discharging, E_d. From E_c and E_d the efficiency of the battery, η, is calculated.

To calculate the charge energy, the power $P(t)$ is determined by multiplying the instantaneous current $I(t)$ by the voltage provided by the power supply, V,

$$P(t) = I(t) * V \tag{5.1.2}$$

If $P(t)$ is integrated over the amount of time necessary to charge the battery then the charging energy can be calculated as

$$\int_0^T P(t)dt = E_c = \int_0^{t_1+t_3} I(t) * V dt \tag{5.1.3}$$

where E_c is the energy needed to charge the battery.

The energy discharged by the battery can be calculated in a similar way. During the discharge of the battery, the current and voltage can be recorded and multiplied together to determine the power discharged.

$$P(t) = I(t) * V(t) \tag{5.1.4}$$

$I(t)$ is the current out of the battery as a function of time as recorded by the ammeter, $V(t)$ is the voltage drop across the battery as a function of time as recorded by the oscilloscope, and $P(t)$ is the power output of the battery as a function of time. If this function is integrated over the amount of time spent discharging the battery, the energy discharged,

E_d, can be calculated as

$$\int_0^T P(t)dt = E_d = \int_0^{t_2} I(t) * V(t)dt \tag{5.1.5}$$

As described in Equation 5.1.1, the charge and discharge energy are used to calculate the efficiency of the battery in the setup, η.

5.1.6 Supercapacitor Hybrid System

A battery-supercapacitor hybrid system was designed and its efficiency compared to that of the battery alone. From common configurations for a battery-supercapacitor hybrid storage system, the passive system was chosen because of its low manufacturing costs and relatively robust nature. In this configuration, a supercapacitor was attached in parallel with the battery so that the supercapacitor can absorb pulsed inputs of energy to extend battery lifetime. Although an active configuration using a DC-DC converter could improve the efficiency of the storage system, it was likely that the converter would consume more power than was available given the relatively low power output from the piezoelectric harvester[29]. The passive configuration slows down battery aging because the transient power is delivered by the supercapacitor, not the battery[45].

To test the passive configuration of the battery-supercapacitor storage system, the circuit was connected to a DC power supply using the same method as the battery system. The quick test method was utilized to test the efficiency of the hybrid system. The hybrid system had the same properties as the battery-only system, so the same method was valid for testing the hybrid system.

5.2 Storage Results and Discussion

In this section, the selection of the battery and test circuitry is described. A method to quantify the efficiency of the different storage systems is presented. Configurations using supercapacitors are considered, and a final design for the hybrid system is chosen.

5.2.1 Initial Setup Results

All tests were performed using MAX17710 chips soldered onto the PCB breakout circuit shown in Figure 5.2.1. The PCB was connected to all other components on a breadboard.

The first test using the MAX17710 chip used the 3 V lithium ion battery. Using a 1 V power supply, the battery was charged to 4.1 V and remained at this SOC as long as the power supply remained connected. However, once the power supply was disconnected, the battery immediately dropped to 3 V, the maximum voltage rating for the battery. The battery could not be discharged while connected to the MAX17710 chip because the unregulated output could not reach the threshold of 3.7 V, causing the voltage to collapse.

The next test was performed with the 3 V battery and a 100 F supercapacitor in a passive parallel configuration. When the supercapacitor was first placed into the breadboard with the power source disconnected, the battery voltage dropped immediately to 0 V. When the power supply was turned on, the battery and supercapacitor system charged at a much slower rate compared to the battery-only system. The charging time frame rose from seconds to hours. To test whether the supercapacitor was fully charged, the supercapacitor was removed from the circuit and returned to the circuit. There was no drop

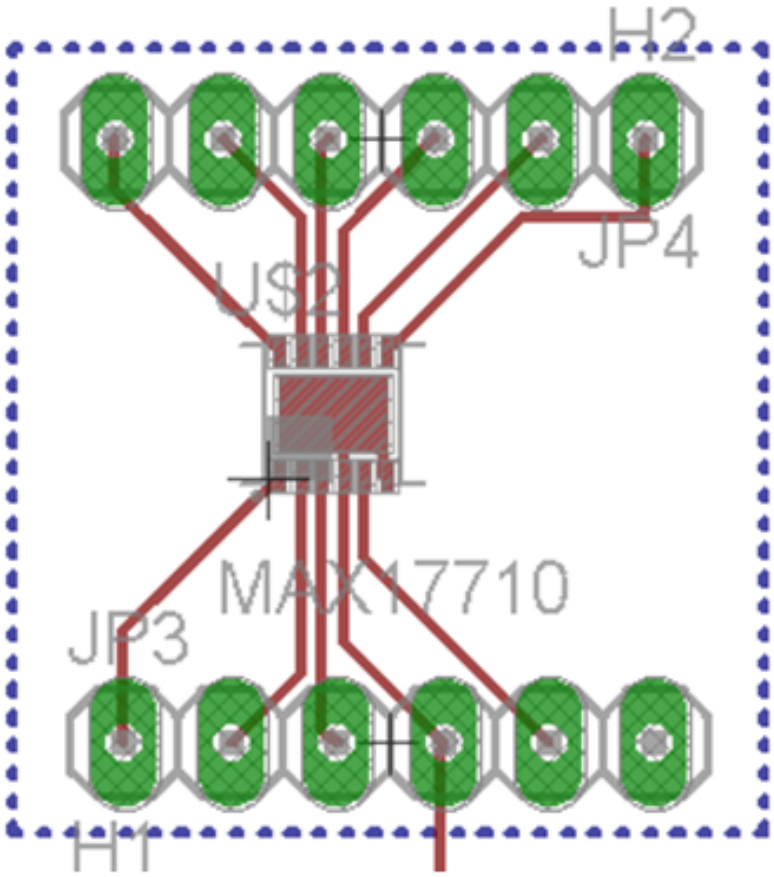

Figure 5.2.1: Breakout circuit designed for the MAX17710 in Eagle PCB Design.

in the battery voltage after the supercapacitor was reconnected, indicating that no charge was flowing from the battery to the supercapacitor. This verified that the supercapacitor was fully charged and was not receiving any more charge from the battery.

5.2.2 Final Setup Results

Due to the inability to discharge the 3 V lithium ion battery directly from the integrated circuit, new 4.1 V batteries were purchased. The MAX17710 chip that was used in the charging circuit was designed for a 4.1 V battery, like the THINERGY battery,

which resolved the issue with the discharge enable threshold. This allowed the battery to discharge into the load when the controlling AE pin was pulsed high. The voltage reading across the LED read 2 V even when the battery was fully charged. This occurred because the LED had an upper voltage limit. A 5 kΩ resistor was placed in series with the LED so that the voltage drop could be monitored across both the resistor and the LED, providing an accurate voltage reading for the load. In addition, the discharge current was calculated by measuring the voltage across the resistor and dividing by the resistance, eliminating the need for an ammeter.

Once there was a reliable method for reading the voltage across both the battery and the load using an oscilloscope, the THINERGY batteries were discharged, and their discharge profiles were monitored. Table 5.1 displays the range of voltages as a function of elapsed time for both the voltage drop across the battery and across the load. During this test, the input DC power supply was disconnected.

Elapsed Time (hours)	0:00	0:08	0:14	0:23	0:24
V_{batt} low	3.64	3.56	3.52	3.48	Breakdown
V_{batt} high	3.68	3.64	3.60	3.56	Breakdown
V_{PCKP} low	3.20	3.00	3.00	2.96	Breakdown
V_{PCKP} high	3.20	3.16	3.12	3.04	Breakdown
V_{PCKP} Average	3.20	3.08	3.06	3.00	Breakdown
V_{LED}	2.00	2.00	2.00	2.00	Breakdown
I_d (mA)	0.240	0.216	0.212	0.200	Breakdown

Table 5.1: Discharge voltage ranges as a function of time for the battery and load

V_{batt} was the voltage drop across the battery. V_{PCKP} was the voltage drop across

the unregulated output pin. V_{LED} was the voltage drop across the LED. The discharge current, I_d, was calculated from the results.

From Table 5.1, there is a steady decline in voltage across both the battery and the load. The voltage decrease was observed across both the battery and load over the period of 24 minutes, indicating that the battery was discharging into the load. The voltage drop across the LED remained constant because the LED had a voltage limit of 2 V, and the load voltage remained above this limit for the duration of the test. At 24 minutes into the discharge cycle, there was an unexpected voltage breakdown of the unregulated output observed on the oscilloscope. See Figure 5.2.2 for the breakdown profile.

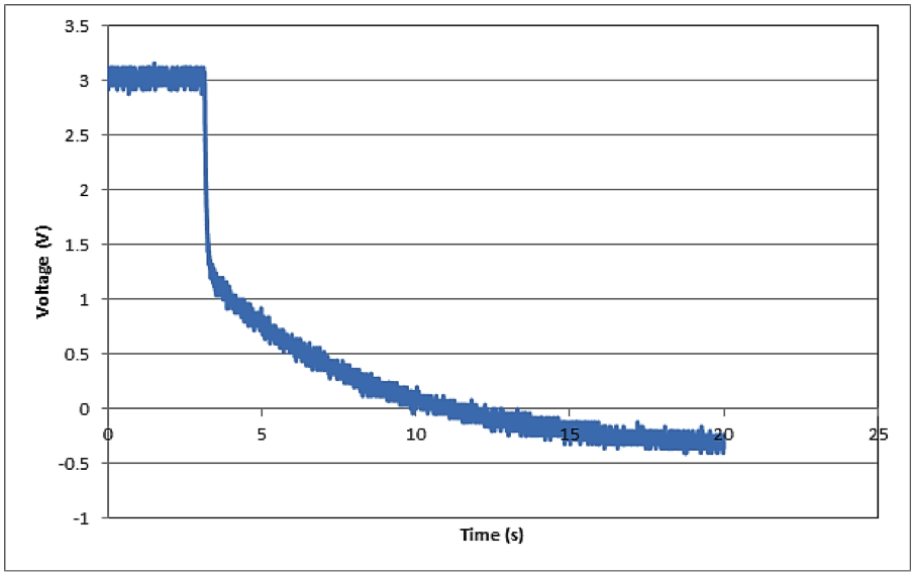

Figure 5.2.2: This graph shows the voltage profile for the unexpected voltage breakdown.

The next trial used another fully charged THINERGY battery. In this trial, beginning and end voltages were recorded over a three hour period. The load was kept constant from the previous setup, a 5 kΩ resistor in series with the LED. This load resulted in discharge currents between 0.2 and 0.24 mA. The battery was disconnected and reconnected

to the circuit between the 2:58 and 3:00 time points. Table 5.2 shows the voltages that were recorded.

Elapsed Time (Hours:Minutes)	0:00	2:58	3:00
V_{batt} low	4.04	2.40	3.60
V_{batt} high	4.08	2.48	3.70
V_{PCKP}	–	1.80	–
V_{LED}	2.00	1.80	–

Table 5.2: Discharge of the battery over a period of three hours

The voltage of the battery decreased significantly over the course of the three hours, indicating that it could drop below the breakdown voltage threshold. However, when the battery was disconnected from the circuit and reconnected, the voltage across the battery rose again to a higher voltage.

The quick test voltage parameters V_0, V_1, and V_2 were determined by charging and discharging the 4.1 V THINERGY battery. V_0 was determined to be 3.25 V, V_1 to be 4.10 V, and V_2 to be 2.44 V. The quick test method was attempted with a discharged battery with an initial voltage of 2.44 V. After 1 minute and 47 seconds (t_3), the battery voltage rose to the V_0 voltage. The voltage continued climbing to 3.6 V, where the voltage reading on the oscilloscope plateaued. Therefore, the quick test method was unable to be completed, and t_1 and t_2 were not collected. Upon later testing of the battery with a multimeter, it was discovered that the voltage had increased to 4.1 V.

It was determined that the 4.1 V THINERGY battery was able to discharge with the MAX17710 chip and a small load over three hours. A 1 V DC power supply was able

to partially recharge the battery. However, after attempting the quick test method, the voltages of the batteries dropped below 3 V. This damaged the batteries, and they could not be charged above 1.68 V. In addition, some of the batteries experienced mechanical failure when wires were soldered to the leads for testing.

5.2.3 Storage Discussion

It was determined that the first battery setup with the 3 V lithium ion battery and the final battery setup with the 4.1 V THINERGY battery were successful at charging the batteries using a 1 V input.

In the first charging circuit using the 3 V lithium ion batteries, many aberrant results were observed. This battery was rated to charge to a maximal SOC of 3 V, but the MAX17710 chip was meant for charging batteries with a voltage rating of 4.1 V. In addition the supercapacitors tested in conjunction with the 3 V batteries were rated at 2.7 V. The discrepancies between these key components caused damage to the storage system. Over the course of testing, all of the 3 V batteries used were degraded due to overcharging. This required a periodic replacement of batteries and made the results from different trials incomparable because of different states of degradation between the batteries. The supercapacitors did not degrade, but were all operating above their safe operation limit. In order to achieve the target functionality, additional circuitry in the form of a DC-DC converter or a different supercapacitor could be used to match the voltages of the battery and supercapacitor.

Two main issues were observed in discharging the batteries through the MAX17710

chip to a load. First, the 3 V battery had too low of a voltage rating to switch the integrated circuit into the discharge state, which has a threshold of 3.7 V on the PCKP pin. Second, the circuit was unable to discharge into a simple diode load because the LED had a maximum voltage of 2 V. The limit of the LED prevented PCKP from rising to 3.7 V. By placing a resistor in series with the LED charge was allowed to build up at the PCKP pin, and the chip was then able to transition the circuit into a discharge state.

The supercapacitor configurations were unsuccessful primarily due to voltage incompatibility between the supercapacitor and the rest of the devices. It was also determined that it would not be meaningful to test the supercapacitor as a standalone storage device. Due to the different electrical characteristics and efficiency considerations of batteries and supercapacitors, a supercapacitor cannot replace a battery in a circuit. When the supercapacitor was connected in parallel with the 3 V battery, the battery immediately discharged into the supercapacitor and its voltage dropped to 0 V. In addition, the hybrid system took much longer to charge than the standalone battery. The supercapacitor presented a large capacitance that dramatically increased the RC time constant and the charging time of the system. The system was unable to charge completely and the output was not at a suitable level for the MAX17710. Therefore without a DC-DC converter, the supercapacitor hybrid is unsuitable for this application.

Acquisition of the 4.1 V THINERGY batteries fixed several of the charging problems originally encountered. This battery allowed for the successful transition of the charging circuit into and out of the discharge state. The higher voltage rating of the batteries allowed the voltage on the PCKP pin to reach 3.7 V. In order to control the transition into the discharge state the AE pin was manually pulsed to V_{batt}. The discharging

state was terminated by pulsing AE to ground. A complete standalone charging device would incorporate a low power micro-controller in order to control this signal. Data was successfully collected on the charge and discharge function for the THINERGY batteries. During discharge the unregulated output consumed 0.22 mA and after three hours the voltage dropped below the safe discharge rating of the battery, causing permanent damage to the THINERGY batteries.

One of the problems observed during testing was that the voltage at the PCKP pin collapsed unexpectedly during some testing periods and no longer provided current to the load. This may have occurred because the battery had passed below its safe discharge voltage and could no longer provide a current to the load. This result was inconsistent because during another trial the battery did not stop discharging causing concern as to the susceptibility of the circuitry to external influences. Many of the problems encountered resulted from manipulation of the measurement leads from the oscilloscope during testing runs, which caused disturbances to the circuit and disrupted proper function of the circuitry and battery. The leads on the THINERGY batteries were also very fragile and mechanical failure of the leads resulted in a functional loss of the batteries.

A similar experiment could be repeated with different testing circuitry and monitoring devices. The oscilloscope used for monitoring the circuit had inherent offsets of up to 0.5 V, which may have led to inaccurate readings during testing. Using an oscilloscope that can simultaneously measure and record data in an external file would allow future experiments to produce more accurate charging profiles. In addition, methods should be devised to prevent mechanical failures of the THINERGY battery.

5.3 Summary

The storage chapter summarizes the testing and results carried out in the development of the energy storage subsystem. The research on designing an energy storage system capable of charging from a low voltage source while providing power to a load of a high voltage began with the acquisition of two different batteries, the 3 V ML614-TZ21 and 4.1 V THINERGY MEC202-17P lithium ion batteries, and a charge regulating microchip, MAX17710. In addition to these two test configurations, a supercapacitor battery hybrid storage system was tested using the 2.7 V, 100 F supercapacitor and the 3 V lithium ion battery in a passive parallel configuration. The MAX17710 was chosen to act as the charge regulator for each of the experimental setups. A modified version of the quick test method was used to determine the efficiency of the setups with a 1 V DC source and an LED and resistor for the load. During this testing it was shown that the regulatory circuitry was able to charge both battery systems and the supercapacitor hybrid system. However, the 3 V battery and the supercapacitor hybrid system were not able to enter the discharge state using the MAX17710 circuitry. When comparing these two systems it was also seen that the battery supercapacitor hybrid system took longer to complete charging. The 4.1 V THINERGY battery was able to pass the threshold voltage to enable discharge to a load through the designed charging circuit. The use of the 4.1 V THINERGY battery provided the expected testing results and corrected several problems seen when running tests on the other storage devices. It also allowed for the determination that the storage system, including the MAX17710 microchip and the 4.1 V THINERGY battery, achieved close to ninety percent efficiency early in its life cycle.

6 Integration

After the completion of subsystem research, further testing was conducted to integrate the harvesting, conditioning, and storage systems. Tests were conducted to determine the maximum power output from and possible sources of loss in the integrated harvester-conditioning system. Finally, tests were conducted to determine how much rectified energy was able to be stored in the conditioning-storage system.

6.1 Integration Testing

Following subsystem testing, the integrated harvester-conditioning system was placed in the wind tunnel to observe how much power was generated. The setup for the harvester was similar to the configuration described in the harvesting methodology. Since the beam was permanently epoxied to the baseline plug, only baseline testing could be performed. Further attempts to separate the plug risked damage to the piezoelectric element and beam.

The fan frequency was swept in order to determine the frequency with the highest AC output voltage of the piezo. Once this frequency had been obtained, the fan frequency was set and the output of the piezoelectric element was wired to the SEH circuit. Using procedures described in the conditioning system methodology, the load resistance of the

SEH circuit was swept in order to determine the optimal resistance which would correspond to a maximum power output. Voltage was measured using the DAQ. The smoothing capacitor for this test was fixed at 10 μF.

Another test setup was designed to integrate the conditioning circuit with the storage subsystem. As in previous experiments, a beam with piezoelectric material excited by the shaker was used as input for the conditioning circuit. The excitation frequency was 78 Hz and the open circuit voltage of the piezoelectric beam was set to 4 V_{pk-pk}. The conditioning circuit replaced the power supply used in experiments with the storage system. A 4.1 V THINERGY battery which was discharged to 1.8 V was used as a test cell. Both the output voltage of the conditioning circuit and the voltage of the battery was monitored as the cell charged after activating the shaker.

6.2 Data Analysis

At the optimal fan frequency, the voltage across the piezoelectric element had a frequency of 56 Hz and an amplitude of 350 mV. This value agrees with the location and magnitude of the voltage peak in previous baseline testing. Figure 6.2.1 shows a trace of the voltage across the piezoelectric element at the optimal fan frequency.

After connecting the SEH circuit and performing a load resistance sweep, several observations were made. Regardless of the load resistance, the output voltage did not change. This voltage remained at a level of 30 mV or 10% of our input voltage. Figure 6.2.2 shows the output from the rectifier circuit when connected to a load of 1kΩ.

With a 4 V_{pk-pk} input signal and a perfect impedance match with minimal power

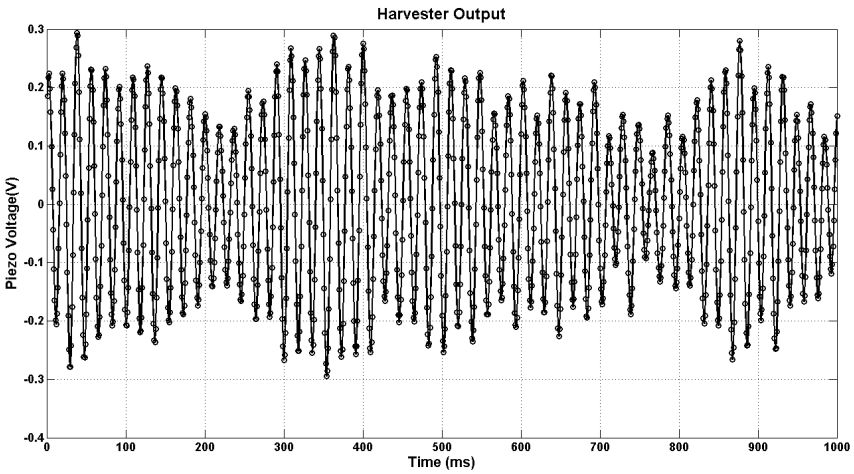

Figure 6.2.1: Voltage across piezoelectric element at 56 Hz

loss, the output from the conditioning circuit was expected to be a DC voltage of 0.7 V. However, with the storage system connected to the conditioning circuit, a 4 V_{pk-pk} input signal produced a DC output of 0.25 V. This 0.25 V output served as the input to the storage system. This voltage was too low to activate the charging mechanism in the MAX17710 chip, so the battery did not charge.

6.3 Discussion

The output voltage of the integration baseline testing agreed with results obtained from previous baseline testing. Regardless, at voltages below 400 mV, there isn't enough voltage to bias the diodes which make up the full wave rectifier. As such, there is no meaningful relationship between input and output voltages. The 30 mV output can most likely be explained by a bias voltage from the measuring device. Without being able to correctly bias the diodes, there is no way to generate a voltage and load resistance relationship. Based on dynamic magnification testing under optimal conditions, a higher

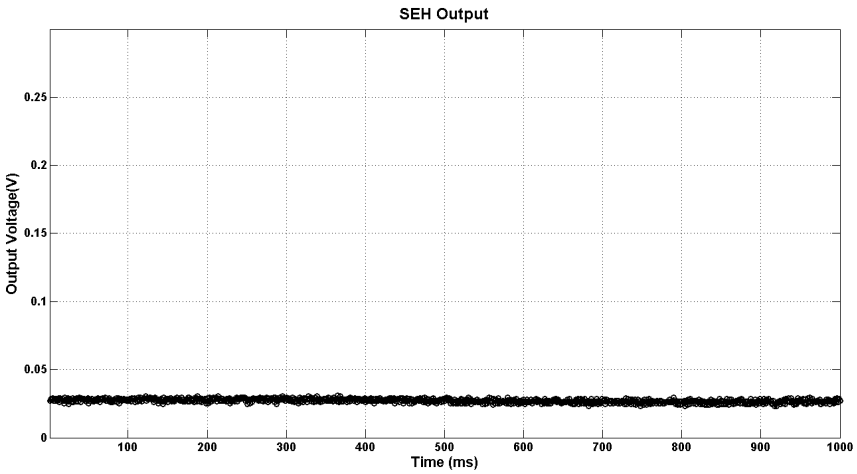

Figure 6.2.2: Rectifier output for integrated circuit

output voltage suitable for the conditioning circuit can be achieved.

The results from integrating the conditioning circuit with the storage system indicate that the impedance mismatch between the two circuits caused losses that prevented proper charging of the battery. The optimal output from the conditioning circuit was 0.7 V when connected to a resistive load, but only 0.25 V was received, which was 65% less than expected. An impedance matching network should be incorporated into future research to ensure optimal power transfer between systems.

6.4 Potential Applications

At the power levels produced in the prototype testing phase it is clear that the current harvester design will not be the solution to the global energy crisis. However, it is important to understand and appreciate the need for such a design is low power applications. The rapidly growing field of microelectromecanical systems often involve low power devices that could utilize the harvester power output. Additionally, bridge and

building sensors without grid access could now draw power from a piezoelectric energy harvester and be used to monitor fires, fatigue, mechanical stress and other structural vital signs. The harvester could be used in even more remote applications such as crop sensors in the center of large fields and mountain or forest sensors that measure climate data.

7 Conclusion

This study successfully demonstrated dynamic magnification, determined a method to find an optimal load given a piezoelectric voltage input, and designed a storage system for low-voltage applications. Further research can be conducted to improve harvester and circuitry design. Scale was a limiting factor in the effectiveness of the energy harvesting system. The design of the energy harvester was limited by the dimensions of the wind tunnel test environment. The integration testing was hindered by insufficient voltage generated by the energy harvester. This insufficient voltage also greatly limited the design of the storage system by reducing the ability to use the stored energy for practical applications and preventing the use of multiple active circuitry components in the design. Utilizing more piezoelectric material, whether by increasing the number or size of harvesters, would increase the voltage output. The SSHI-P rectifying circuit would become a potentially viable option with a larger voltage output from the harvester. In addition, the storage system could consist of additional components including a DC-DC converter and a microcontroller which consume power from the source but would reduce limitations that were observed in the storage design.

Further research could focus on integration of an energy harvester with a rectifying circuit and a storage system at the onset of experimentation. To focus on an integrated

system, the impedance of the rectifying circuit would need to be closely matched to the impedance of the storage system in order to store energy. Additional research could involve testing the integrated system solely on a shaker. By focusing on shaker testing instead wind tunnel testing, experimental data would be more reliable because the input variables such as frequency and vibrational intensity would be easily controlled.

Piezoelectric energy harvesting utilizing dynamic magnification through wind-induced vibrations is a novel concept that can benefit from continued research. Investigation into this type of renewable energy can have a positive impact on low flow velocity wind energy harvesting. Crucial elements of this research include determining the reliability of piezoelectrics for these applications and assessing the feasibility of these energy harvesters. The research presented here can serve as a foundation for future exploration of piezoelectric wind energy harvesters.

Glossary

Energy Harvesting

Cyclic loading - portions of the system are exposed to fluctuating loads continually in order to determine the effects on a material over time

Degenerate states - two or more states are degenerate if they have the same energy level, so the system is equally likely to be in either state

Dielectric - electrical insulator that can be polarized by aligning domains with an applied electric field

Domain wall - a gradual reorientation of magnetic moments forming a boundary between magnetic domains

Endurance limit - the maximum stress which can be applied to a material for an infinite number of stress cycles without resulting in failure of the material.

Magnetic domain - a region of uniform magnetization, with all individual magnetic moments of the atoms alligned in the same direction

Rhombohedral - three equal aces and oblique angles

Tetragonal - rectangular prism

Energy Conditioning

Alternating current (AC) - a flow of electric charge that periodically reverses direction

Capacitor - a passive two-terminal electrical component used to store energy in an electric field. Capacitors are widely used in circuits for blocking direct current while passing

alternating current

Coupling (weak, strong) - the transfer of electrical energy from one circuit segment to another

Diode - a two-terminal electrical component with low resistance to current flow in one direction and high resistance to current flow in the other

Direct current (DC) - a flow of electric charge that only flows in one direction

Full-bridge rectifier – a rectifier circuit that uses four diodes connected in a closed-loop bridge to produce the desired output

Gain - the measure of the ability of a circuit to increase the power of a input signal.

Impedance - the measure of the opposition to the passage of current when voltage is applied to a circuit.

Inductor - a passive electrical component that stores energy in a magnetic field.

Phase shift - In a sinusoidal wave, a phase shift describes a wave with an offset starting angle.

Rectifier - a circuit which converts AC current into DC current.

Standard energy harvester (SEH) - a rectifier circuit that consists of a standard full-bridge rectifier coupled with a resistor and capacitor in series

Synchronous switch harvesting on inductor (SSHI) - a rectifier circuit that is formed by placing a branch with an inductor, a switch, and a resistor in parallel (SSHI-parallel) or in series (SSHI-series) to the traditional SEH circuit

Energy Storage

Coulombic efficiency - the amount of battery charge output to input

Depth of discharge - the amount that a battery can ideally be discharged without adversely affecting other properties of the battery

Energy capacity - the amount of energy a battery can hold in total

Energy density - the capability to deliver energy over its volume: how much electricity a system can store as compared to the space it takes up

Life span - the number of charge and discharge cycles that it can undergo before it needs to be replaced

Memory effect - when a battery's maximum energy capacity drops after being repeatedly charged but only partially discharged since the battery remembers only the lower energy capacity

Operating temperature - the ideal temperature at which the battery will charge and discharge, without adversely affecting any other properties of the battery

Power capacity - the maximum rate of energy transfer over time

Power density - the power per volume of battery

Pulse width modulation – a manner of delivering energy through a succession of pulses rather than a continuously varying signal

Rate of self-discharge - the amount of energy that is dissipated over time when the batter is not connected to anything

Rate capacity effect - an effect that causes degradation of the battery discharge efficiency under high load currents

State of charge – the percent of the total energy capacity contained in a battery at an instantaneous moment of time

Bibliography

[1] *Contribution of working group I to the fourth assessment report of the intergovernmental panel on climate change*, 2007.

[2] O. Aldraihem and A. Baz. Energy harvester with a dynamic magnifier. *Journal of Intelligent Material Systems and Structures*, pages 521–530, 2011.

[3] S. R. Anton and H. A. Sodano. A review of power harvesting using piezoelectric materials(2003-2006). *Smart Materials and Structures*, 16(3):R1–R22, 2007.

[4] A. Ballato. Piezoelectricity: Venerable effect, modern thrusts. *Army Research Lab Fort*, pages 1–26, 1994.

[5] P. P. Barker. Ultracapacitors for use in power quality and distributed resource applications. *Power Engineering Society Summer Meeting, 2002 IEEE*, 1:316–320, July 2002.

[6] A. Baz. The structure of an active acoustic metamaterial with tunable effective density. *New Journal of Physics*, 11, 2009.

[7] P. W. Bearman. Vortex shedding from oscillating bluff bodies. *Annual Review of Fluid Mechanics*, 16(1):195–222, 1984.

[8] P. W. Bearman, J. R. Chaplin, and F. J. Huera Huarte. On the force distribution along the axis of a flexible circular cylinder undergoing multi-mode vortex-induced vibrations. *Journal of Fluids and Structures*, 22(6):897–903, 2006.

[9] A. J. Bell. Factors influencing the piezoelectric behaviour of pzt and other "morphotropic phase boundary" ferroelectrics. *Journal of Materials Science*, 41(1):13–25, 2006.

[10] M. Bernitsas. Out of the vortex. *Mechanical Engineering*, 132(4), 2010.

[11] K. Y. Billah and R. H. Scanlan. Resonance, tacoma narrows bridge failure, and undergraduate physics textbooks. *American Journal of Physics*, 59(2):118–124, 1991.

[12] J. Brufau-Penella and M. Puig-Vidal. Piezoelectric energy harvesting improvement with complex conjudgate impedance matching. *Intelligent Material Systems and Structures*, 20(5):597–608, March 2009.

[13] F. Dincer. The analysis on photovoltaic electricity generation status, potential and policies of the leading countries in solar energy. *Renewable and Sustainable Energy Reviews*, 15(1):713–720, January 2011.

[14] I. Dincer. Renewable energy and sustainable development: A crucial review. *Renewable and Sustainable Energy Reviews*, 4(2):157–175, June 2000.

[15] K. C. Divya and J. Ostergaard. Battery energy storage technology for power systems. *Electric Power Systems Research*, 79(4):511–520, 2009.

[16] B. Dunn, H. Kamath, and J.-M. Tarascon. Electrical energy storage for the grid: A battery of choices. *Science*, 344(6058):938–935, 2011.

[17] J. E. Garcia, D. A. Ochoa, V. Gomis, J. A. Eiras, and R. Pérez. Evidence of temperature dependent domain wall dynamics in hard lead zirconate titanate piezoceramics. *Journal of Applied Physics*, pages 139–142, 2012.

[18] J. Gerrard. The mechanics of the formation region of vortices behind bluff bodies. *Journal of Fluid Mechanics*, 25(2):401–413, 1966.

[19] L. M. Gil-Martin, J. F. Carbonell-Marquez, E. Hernandez-Montes, M. Aschheim, and M. P. Fernandez. Dynamic magnification factors of sdof oscillators under harmonic loading. *Applied Mathematics Letters*, 25(1):38–42, 2012.

[20] P. E. Glaser. Power from the sun: its future. *Science*, 162(3856):857–861, 1968.

[21] M. J. Guan and W. H. Liao. On the efficiencies of piezoelectric energy harvesting circuits towards storage device voltages. *Smart Materials and Structures*, 16(2):498, 2007.

[22] M. Hadartz and M. Julander. *Battery-Supercapacitor energy storage*. PhD thesis, Chalmers University of Technology, 2008.

[23] B. Haug. High power bus in li-ion handheld. *Electronics Weekly*, (2359):40, 2008.

[24] C. E. Holland, J. W. Weidner, R. A. Dougal, and R. E. White. Experimental characterization of hybrid power systems under pulse current loads. *Journal of Power Sources*, 109(1):32–37, 2002.

[25] W. Huang, X. Wang, J. Guo, J. Zhang, and J. Yang. Discussion on application of super capacitor energy storage system in microgrid. *International Conference on Sustainable Power Generation and Supply*, 2009.

[26] ICPE '07. 7th Internatonal Conference on Power Electronics, 2007. *Energy storage technology markets and applications: ultracapacitors in combination with lithium-ion*, 2007.

[27] A. Ju. *Students Harness Vibrations from Wind for Electricity*. Cornell Chronicle, May 2010.

[28] N. Krihely and S. Ben-Yaakov. Self-contained resonant rectifier for piezoelectric sources under variable mechanical excitation. *IEEE Transactions on Power Electronics*, 26(2):612–621, 2011.

[29] A. Kuperman and I. Aharon. Battery-ultracapacitor hybrids for pulsed current loads: A review. *Renewable and Sustainable Energy Reviews*, 15(2):981–992, 2011.

[30] J. Liang and W.-H. Liao. Impedance matching for improving piezoelectric energy harvesting systems. *Proc. SPIE*, 7643:76430K–76430K–12, 2010.

[31] I. C. Lien, Y. C. Shu, W. J. Wu, S. M. Shiu, and H. C. Lin. Revisit of series-sshi with comparisons to other interfacing circuits in piezoelectric energy harvesting. *Smart Materials and Structures*, 19(12):125009, 2010.

[32] J. H. Lienhard. *Synopsis of lift, drag, and vortex frequency data for rigid cylinders*. PhD thesis, Washington State University, College of Engineering Research Divisions, 1966.

[33] K. J. Loh and D. Chang. Zinc oxide nanoparticle-polymeric thin films for dynamic strain sensing. *Journal of Materials Science*, 46:228–237, 2011.

[34] Z. Luo, S. Pojprapai, J. Glaum, and M. Hoffman. Electrical fatigue-induced cracking in lead zirconate titanate piezoelectric ceramic and its influence quantitatively analyzed by refatigue method. *Journal of the American Ceramic Society*, 95(8):2593–2600, 2012.

[35] A. Manbachi and R. S. C. Cobbold. Development and application of piezoelectric materials for ultrasound generation and detection. *Ultrasound*, 19(4):187–196, 2011.

[36] National Instruments Corporation. *NI USB-6008/6009 User Guide and Specifications*, February 2012.

[37] A. Odabaee. Buck-boost dc-dc regulators evolve. *Electronics Weekly*, (2341):14–15, 2008.

[38] E. Ogut, O. S. Yordem, Y. Menceloglu, and M. Papila. Poly(vinylidene fluoride)/zine oxide smart composite material. *Proceedings of SPIE*, 6526, 2007.

[39] M. Okayasu and Y. Sato. New experimental techniques for in-situ measurement of the damage characteristics of piezoelectric ceramics under high cycle fatigue testing. *Experimental Mechanics*, 52(8):1009–1020, 2012.

[40] F. Ongaro, S. Saggini, and P. Mattavelli. Li-ion battery-supercapacitor hybrid storage system for a long lifetime, photovoltaic-based wireless sensor network. *IEEE Transactions on Power Electronics*, 27(9):3944–3952, 2012.

[41] J. H. Pedersen. *Low Frequency Low Voltage Vibration Energy Harvesting Converter*. PhD thesis, Technical University of Denmark, November 2011.

[42] G. Sessler. Piezoelectricity in polyvinylidenefluoride. *Journal of the Acoustical Society of America*, 70(6):1596–1608, 1981.

[43] D. Shin, Y. Kim, Y. Wang, N. Chang, and M. Pedram. Constant-current regulator-based battery-supercapacitor hybrid architecture for high-rate pulsed load applications. *Journal of Power Sources*, 205:516–524, 2012.

[44] Y. C. Shu, I. C. Lien, and W. J. Wu. An improved analysis of the sshi interface in piezoelectric energy harvesting. *Smart Materials and Structures*, 16(6):2253, 2007.

[45] K. A. Smith. Electrochemical control of lithium-ion batteries [applications of control]. *Control Systems, IEEE*, 30(2):18–25, 2010.

[46] G. W. Taylor, J. R. Burns, S. A. Kammann, W. B. Powers, and T. R. Welsh. The energy harvesting eel: A small subsurface ocean/river power generator. *Smart Materials and Structures*, 26(4):539–547, 2001.

[47] J. Thomas and M. Qidwai. The design and application of multifunctional structure-battery materials systems. *JOM*, 57(3):18–24, 2005.

[48] Y. Ting, G. Hariyanto, B. K. Hou, and C. Y. Huang. Conference paper. Paper presented at the IEEE International Conference on Information and Automation, Zhuhai/Macau, China.

[49] U.S. Energy Information Administration. *U.S. primary energy consumption by source*, 2010.

[50] U.S. Environmental Protection Agency. *Inventory of U.S. greenhouse gas emissions and sinks: 1990-2009*, 2011.

[51] W. Zhou, G. R. Penamalli, and L. Zuo. An efficient vibration energy harvester with a multi-mode dynamic magnifier. *Smart Materials and Structures*, 21(1):015014, 2011.

Appendices

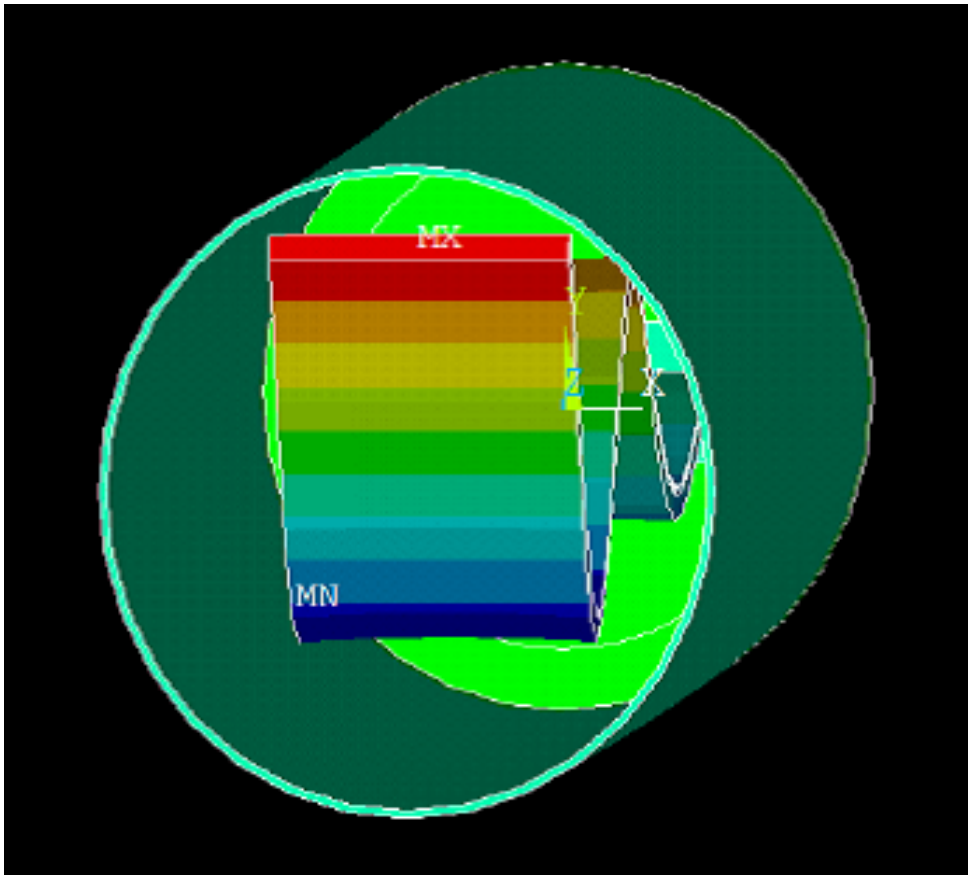

Figure .0.1: FEM showing the 4th bending mode of the inner beam at 191 Hz in the baseline configuration

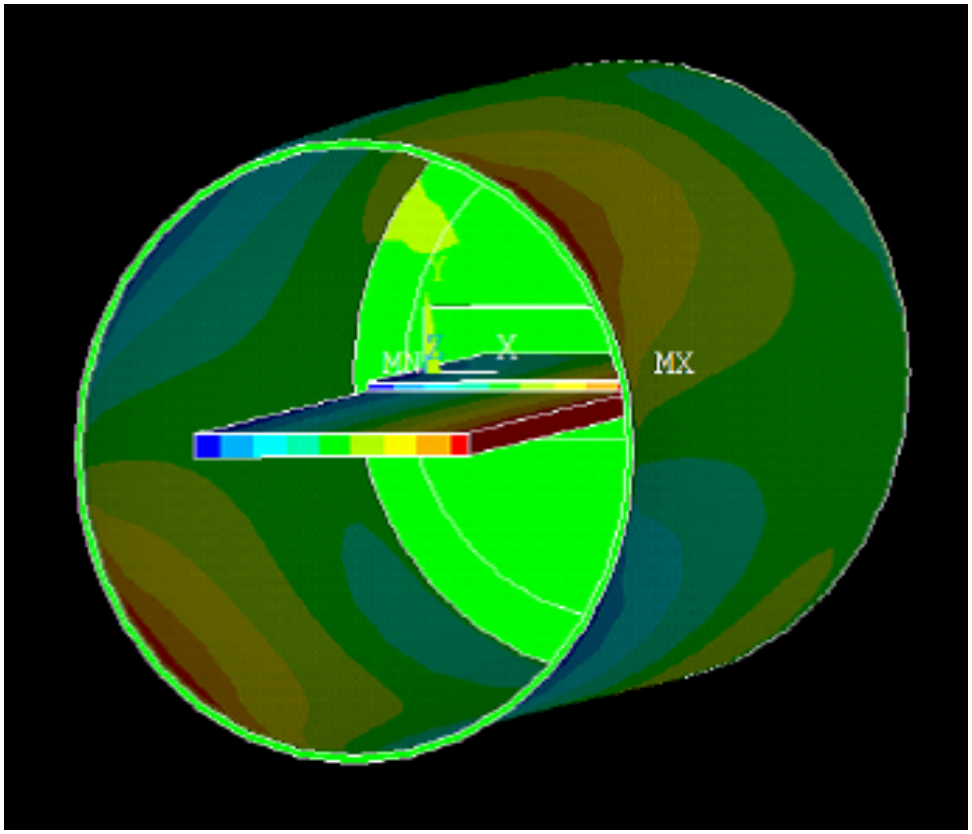

Figure .0.2: FEM showing the 1st bending mode of the outer cylinder at 191 Hz in the baseline configuration

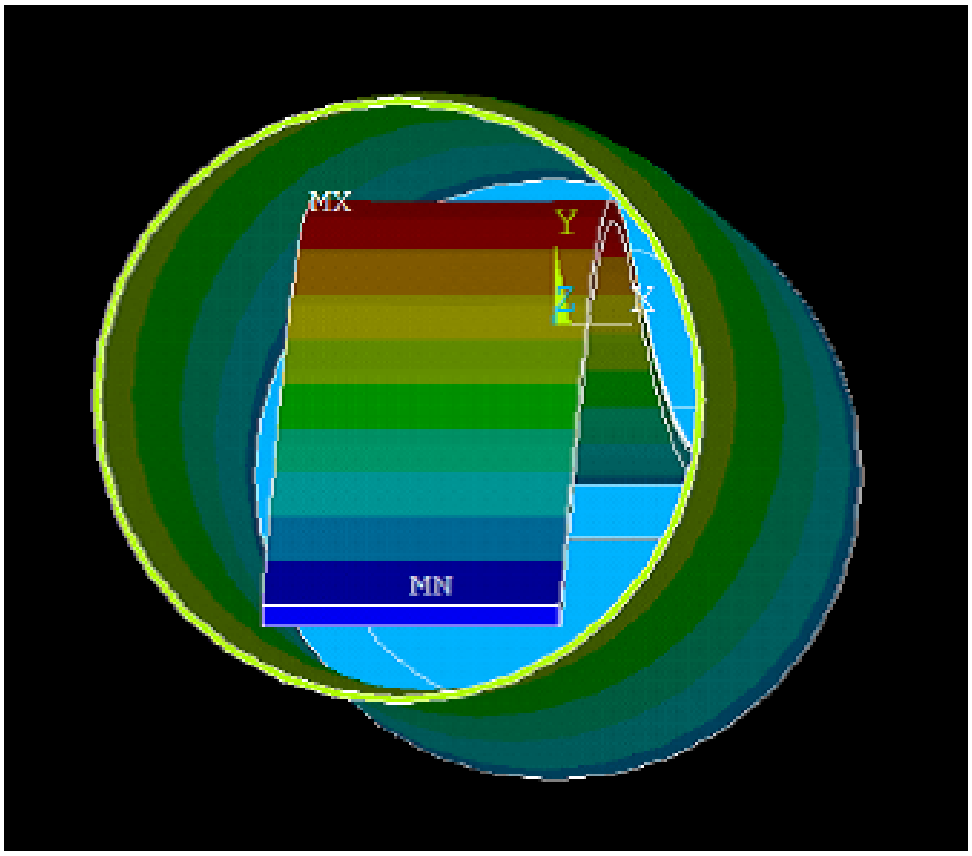

Figure .0.3: FEM showing the 2nd bending mode of the outer cylinder at 191 Hz in the baseline configuration

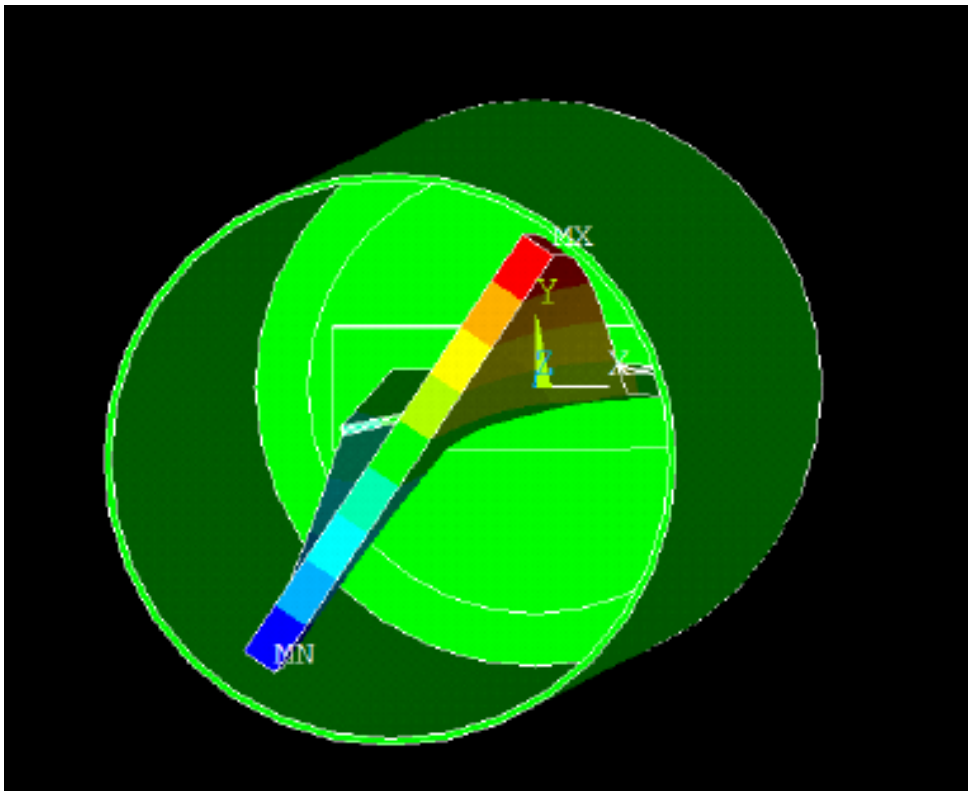

Figure .0.4: FEM showing the 1st torsional bending mode of the inner beam at 171 Hz in the baseline configuration

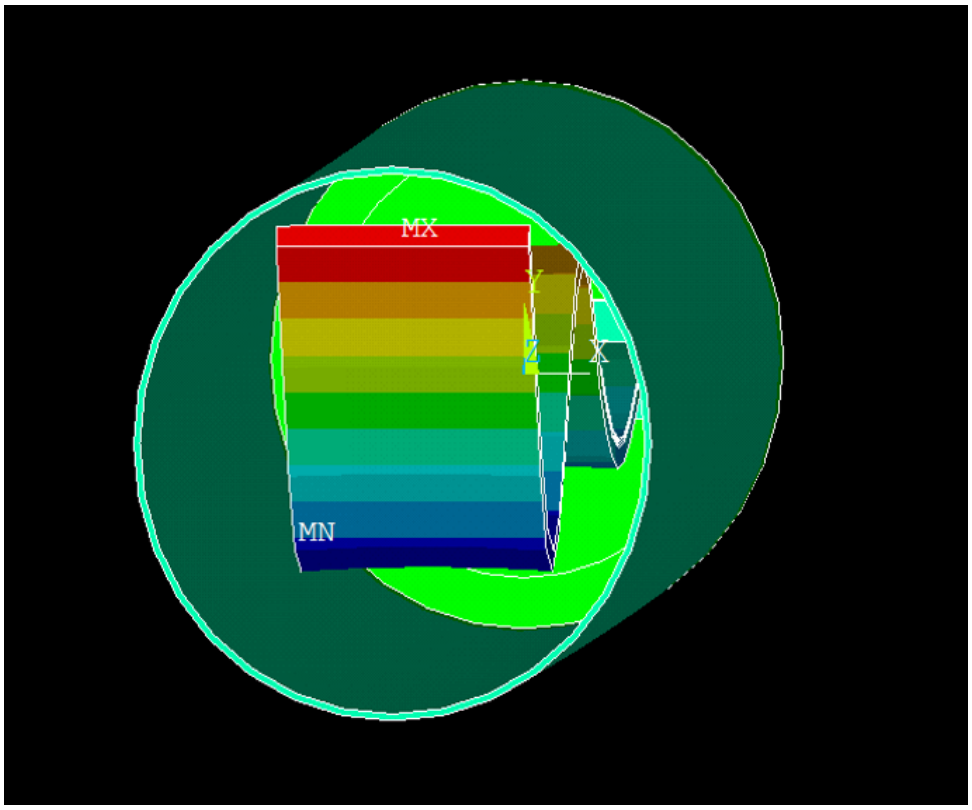

Figure .0.5: FEM showing the 4th bending mode of the inner beam at 191 Hz with dynamic magnification

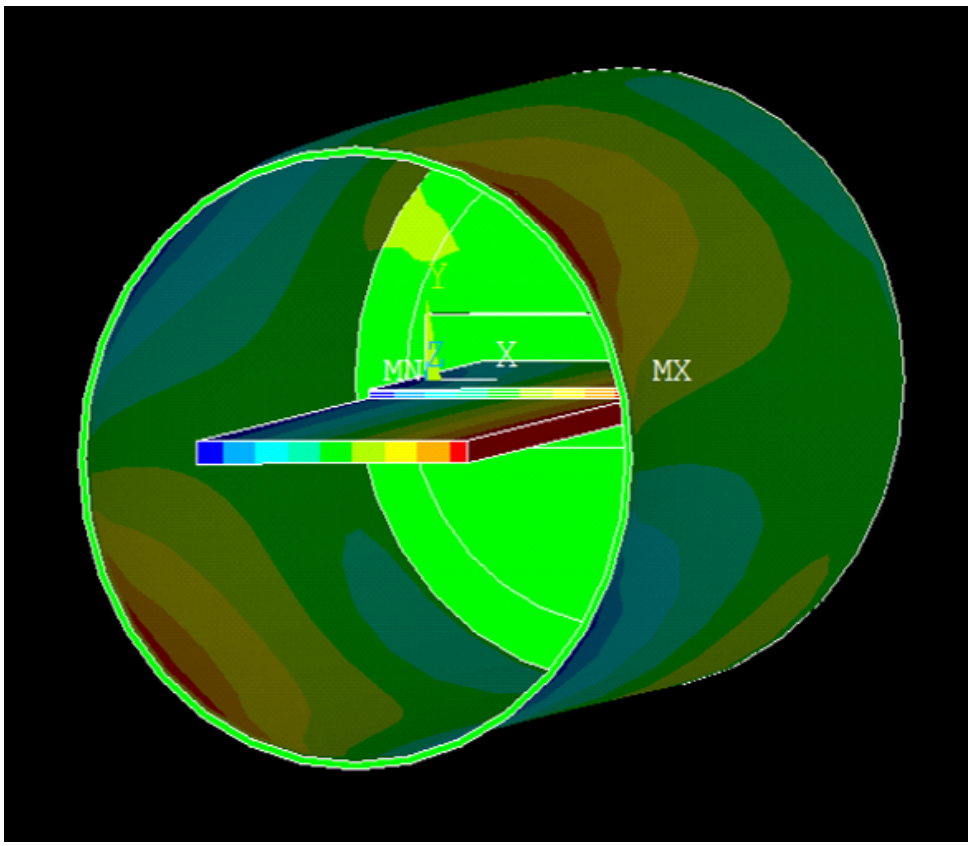

Figure .0.6: FEM showing the 1st bending mode of the outer cylinder at 191 Hz with dynamic magnification

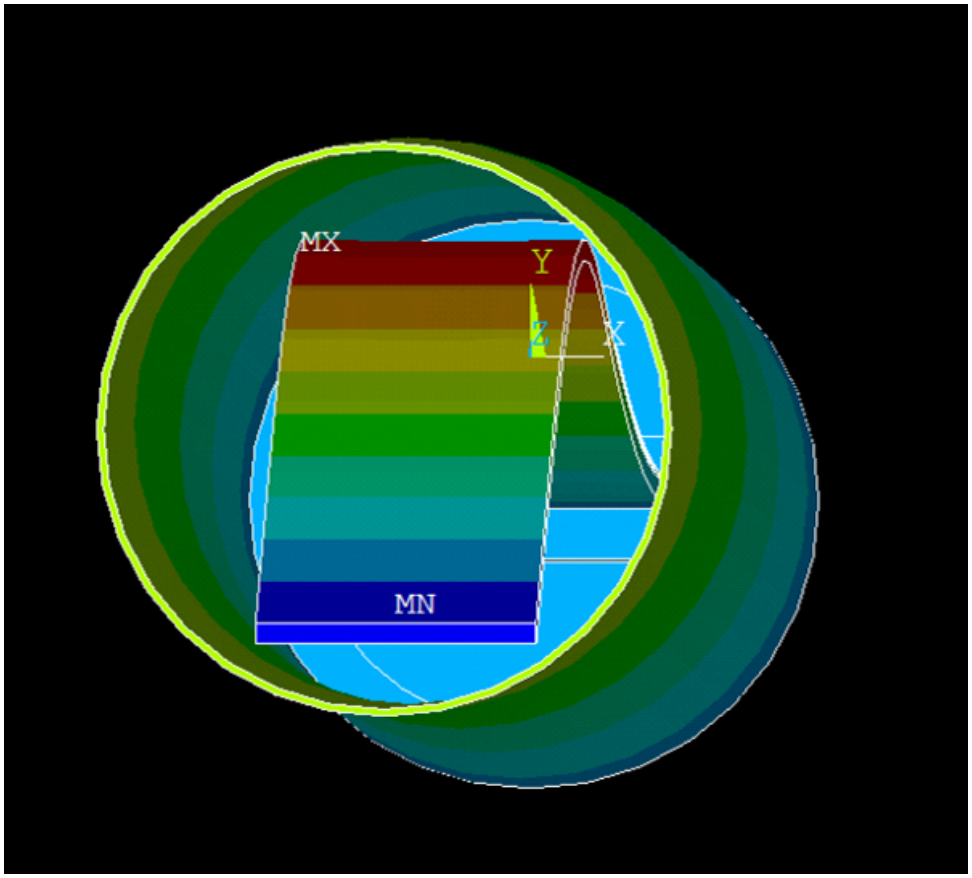

Figure .0.7: FEM showing the 2nd bending mode of the outer cylinder at 191 Hz with dynamic magnification

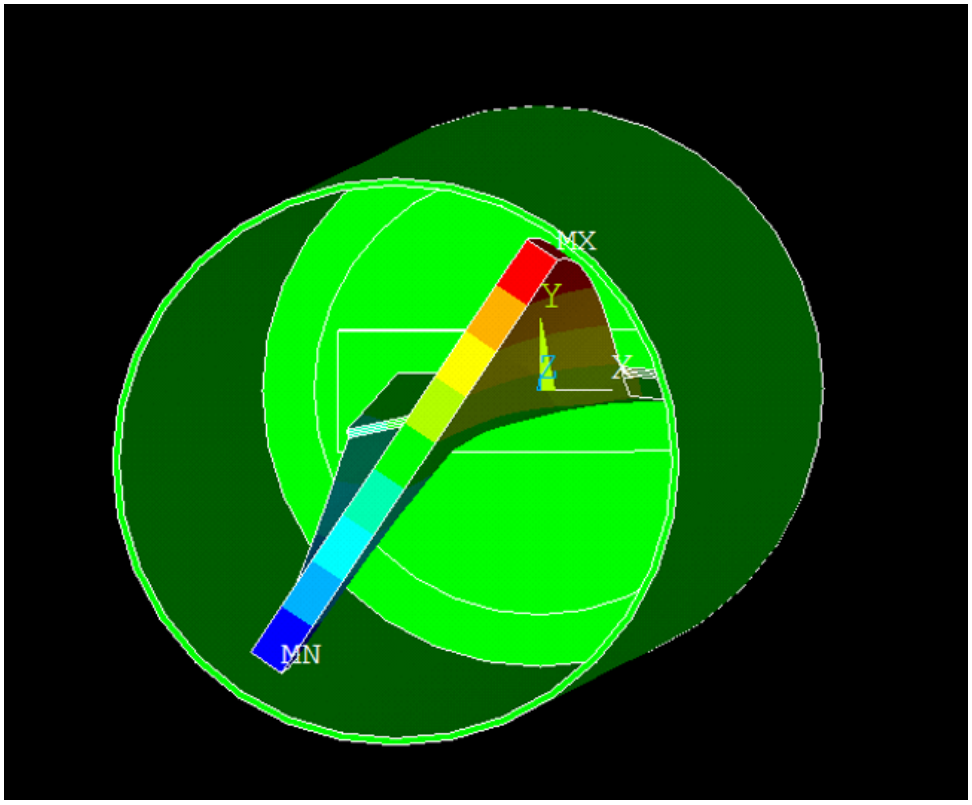

Figure .0.8: FEM showing the 1st torsional bending mode of the inner beam at 171 Hz with dynamic magnification

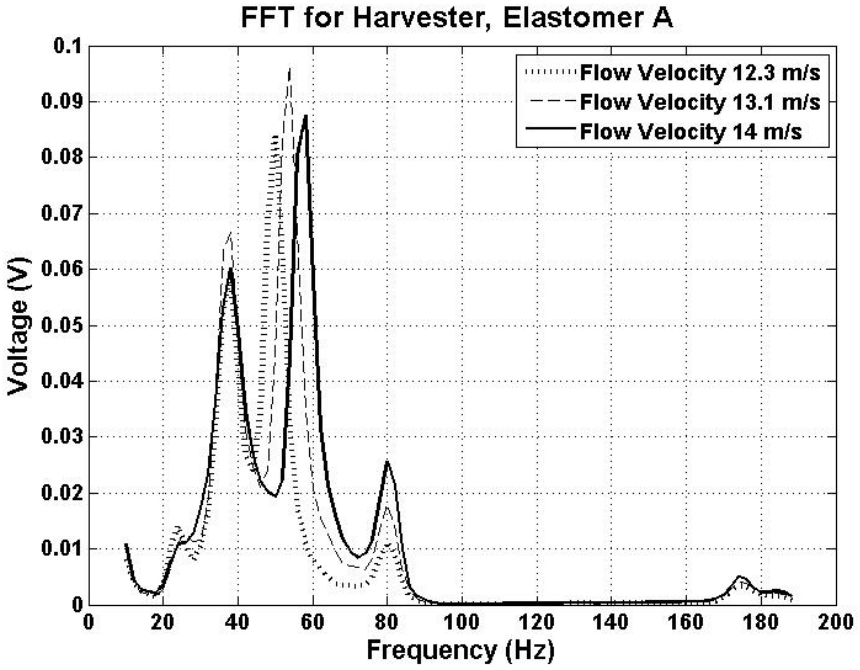

Figure .0.9: Peak voltage output for the harvester system with elastomer A for flow velocities ranging from 12.3-14 m/s

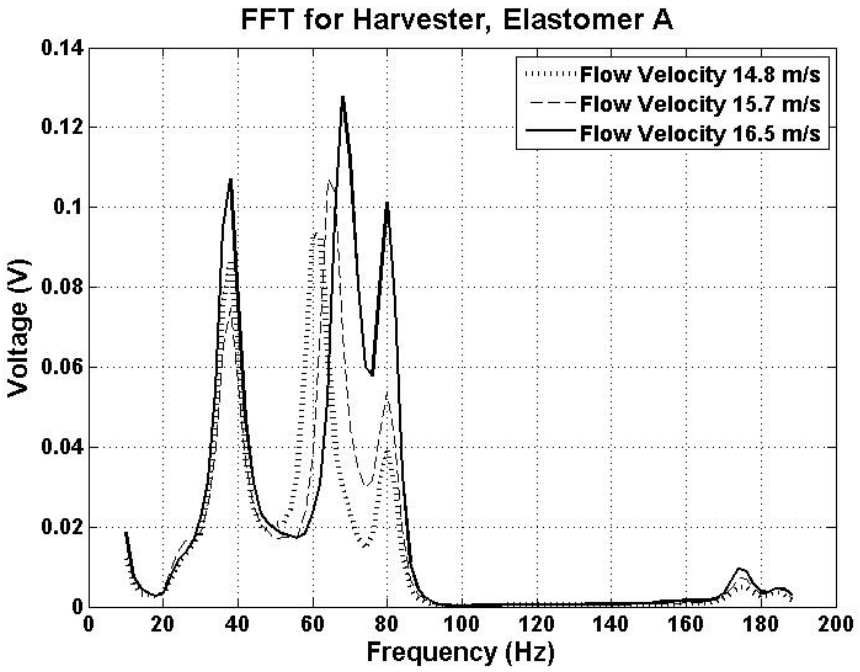

Figure .0.10: Peak voltage output for the harvester system with elastomer A for flow velocities ranging from 14.8-16.5 m/s

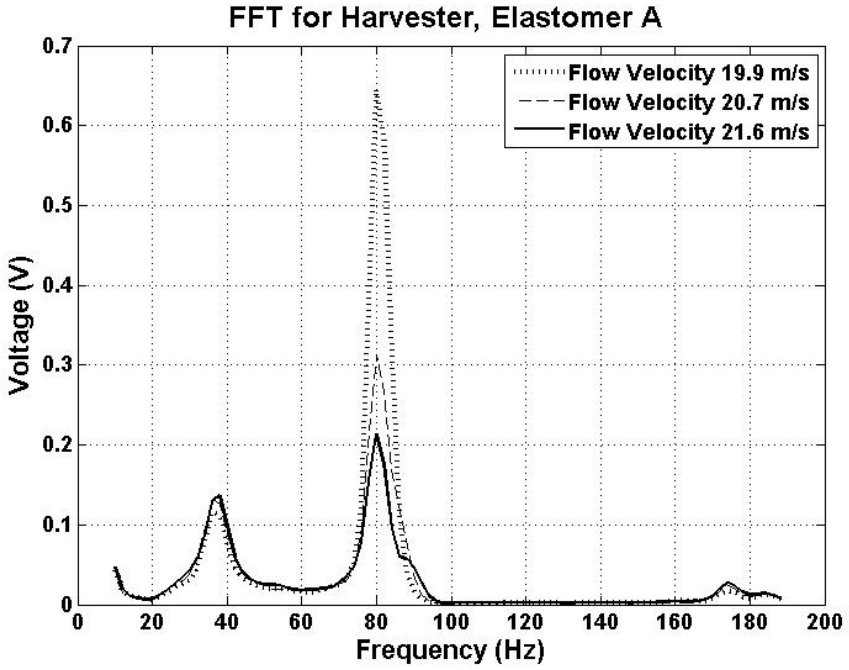

Figure .0.11: Peak voltage output for the harvester system with elastomer A for flow velocities ranging from 19.9-21.6 m/s

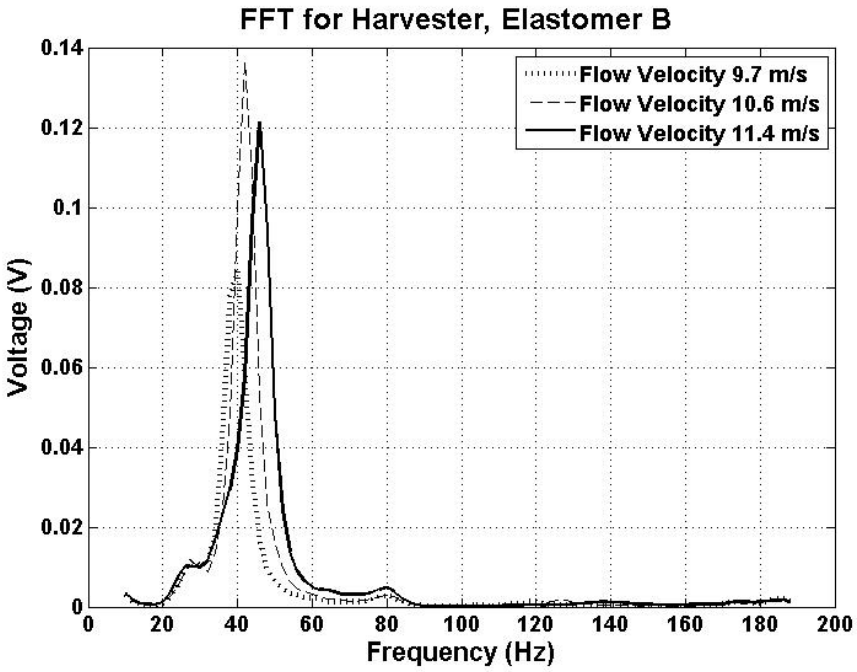

Figure .0.12: Peak voltage output for the harvester system with elastomer B for flow velocities ranging from 9.7-11.4 m/s

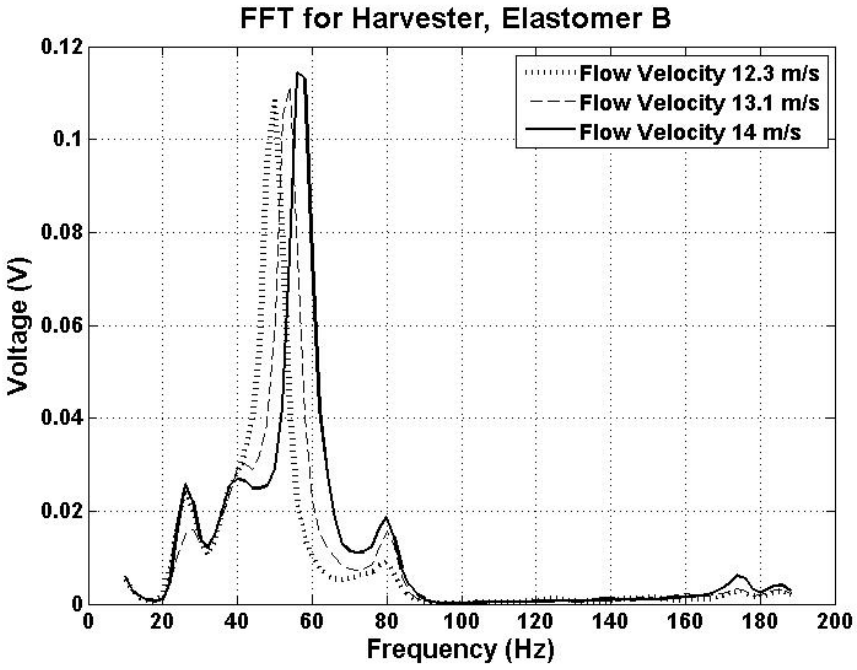

Figure .0.13: Peak voltage output for the harvester system with elastomer B for flow velocities ranging from 12.3-14 m/s

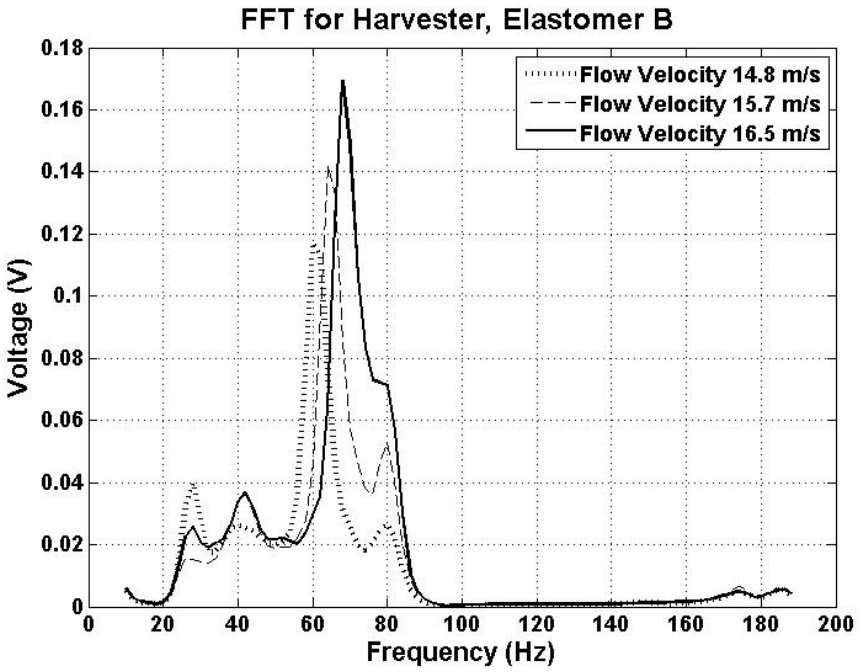

Figure .0.14: Peak voltage output for the harvester system with elastomer B for flow velocities ranging from 14.8-16.5 m/s

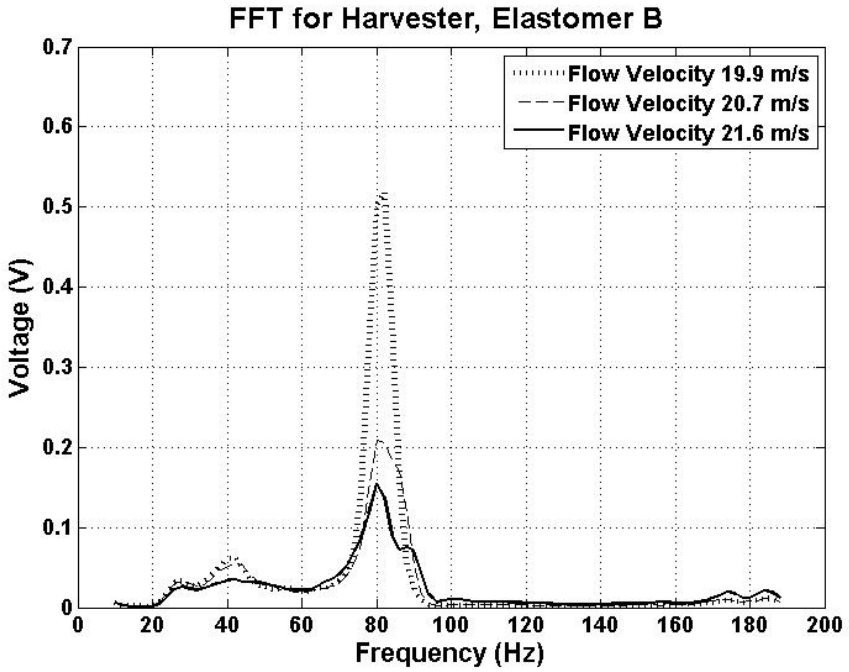

Figure .0.15: Peak voltage output for the harvester system with elastomer B for flow velocities ranging from 19.9-21.6 m/s